Title
THE EFFECT OF FREE-PARTICLE COLLISIONS IN HIGH ENERGY PROTON and PION-INDUCED NUCLEAR REACTIONS

Author
Jacob Jr., Norman P.

Publication Date
1975-07-01

LBL-4067
c.1

THE EFFECT OF FREE-PARTICLE COLLISIONS IN HIGH ENERGY PROTON AND PION-INDUCED NUCLEAR REACTIONS

Norman P. Jacob, Jr.
(Ph. D. thesis)

July 1975

Prepared for the U. S. Energy Research and Development Administration under Contract W-7405-ENG-48

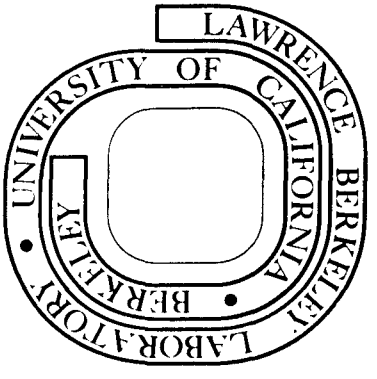

LBL-4067
c.1

DISCLAIMER

I

Common sense, do what it will, cannot avoid being surprised occasionally. The object of science is to spare it this emotion and create mental habits which shall be in such close accord with the habits of the world as to secure that nothing shall be unexpected.

B.R.

TABLE OF CONTENTS

THE EFFECT OF FREE-PARTICLE COLLISIONS IN HIGH ENERGY PROTON AND PION-INDUCED NUCLEAR REACTIONS

Norman P. Jacob, Jr.

(Ph.D. Thesis)

Department of Chemistry
and
Lawrence Berkeley Laboratory
University of California
Berkeley, California 94720

ABSTRACT

The effect of free-particle collisions in simple "knockout" reactions of the form (a,aN) and in more complex nuclear reactions of the form (a,X) was investigated in a two part study by using protons and pions as the incident projectiles. In the first part of this study, cross sections for the $^{48}Ti(p,2p)\ ^{47}Sc$ and the $^{74}Ge(p,2p)\ ^{73}Ga$ reactions were measured from 0.3 to 4.6 GeV incident proton energy. The results indicate a rise in (p,2p) cross section for each reaction of about (25 ± 3)% between the energies 0.3 and 1.0 GeV and are correlated to a large increase in the total free-particle pp scattering cross sections over the same energy region. The experimental results are compared to previous (p,2p) excitation functions in the GeV energy region and to (p,2p) cross section calculations up to 1 GeV incident proton energy based on a Monte Carlo intranuclear cascade-evaporation model. This model yields cross sections that are generally a factor of 2 greater than the experimental values.

In the second part of this thesis, cross section measurements for $(\pi^{\pm},\pi N)$ and other more complex pion-induced spallation reactions were

measured for the light target nuclei ^{14}N, ^{16}O, and ^{19}F from 45 to 550 incident pion energy. These measurements indicate clearly a broad peak in the excitation functions for both $(\pi,\pi N)$ and (π,X) reactions near 180 MeV incident pion energy. This corresponds to the large resonances observed in the free-particle π^+p and π^-p cross sections at the same energy. Striking differences in $(\pi,\pi N)$ cross section magnitudes are observed among the light nuclei targets. The experimental cross section ratio $R_{\pi^-/\pi^+} = \sigma(\pi^-,\pi^-n)/\sigma(\pi^+,\pi N)$ at 180 MeV is 1.7 ± 0.2 for all three targets. The experimental results are compared to previous pion and analogous proton-induced reactions, to Monte Carlo intranuclear cascade-evaporation calculations, and to a semi-classical nucleon charge exchange model in an effort to understand the mechanism of pion reactions, particularly of the $(\pi,\pi N)$ reaction.

Part I. Cross Sections Above 0.3 Gev for (p,2p) Reactions of ^{48}Ti and ^{74}Ge

1. INTRODUCTION

The interaction of high energy projectiles (> 0.1 GeV/nucleon) with nuclei has been a field of considerable interest since the advent of the Berkeley 184-inch synchrocyclotron in 1947. Since then, the development and construction of charged particle accelerators, and more recently the "meson factories" have made it possible to perform these studies with a variety of projectiles, ranging from charged pions to heavy ions, and extending in energy into the gigaelectron volt region. The majority of these studies have been directed toward an understanding of reaction mechanisms, such as fission and fragmentation, nuclear properties and structure, and elementary particle behavior in the presence of nuclear matter. In addition, such research is applicable in cosmic ray physics and astrophysics for understanding the yields of radionuclides in extraterrestrial specimens such as meteorites and moon rocks and in the choice of shielding materials for high energy, high intensity accelerators, where activation of the surroundings is a potential problem.

Specifically, the broad objective to this thesis was to investigate elementary particle behavior in the presence of nuclear matter. In order, then, to provide a foundation for understanding the principles that are fundamental to this project, a brief review of high energy nuclear reaction models and theories is presented in the following section. This area has been the subject of several excellent reviews by Miller and Hudis(1), Grover and Caretto(2) and more recently by Hudis(3). These articles are recommended as references for a more extensive treatment of the subject than given here.

1.1 The Cascade-Evaporation Model and the Impulse Approximation

The model of nuclear reactions induced by high energy projectiles was originally proposed by Serber(4) to explain the wide distribution of radioactive nuclides formed in the 200 MeV deuteron irradiation of ^{75}As as found by Cunningham and co-workers(5). This model considers the mechanism to be the sum of two stages. In the first stage, the incident projectile collides with a single nucleon in the nucleus. These collision partners may subsequently collide with other nucleons and generate a nucleonic cascade. The struck particles may escape from the nucleus with high kinetic energies and be forward peaked. The incident projectile could make several more collisions before escaping the nucleus with most of its initial kinetic energy. This process is short on the time scale for nuclear reactions and is of the order of 10^{-22} - 10^{-21} seconds duration.

The second stage of this process is the subsequent de-excitation of the excited residual cascade nucleus in a manner similar to that for low energy nuclear reactions i.e., by emission of nucleons, alpha particles, photons, or even fission fragments. This is termed the "evaporation" stage and has a time scale that is on the order of 10 to 1000 times as long as the cascade stage. Thus, the average de-excitation time for an excited nucleus would last about 10^{-20} - 10^{-18} seconds.

In light of this mechanism, the wide distribution of product nuclides formed in a high energy nuclear reaction can be logically explained. Depending upon the complexity of the nucleonic cascade, high as well as low energy deposition events will occur, which in turn, create a wide range of final nuclides after completion of the second or "evaporation" stage of the reaction.

This model was further developed by Chew and co-workers(6-8), who proposed the "impulse approximation". This particular approach postulated that the target nucleus would appear to a high energy projectile as a collection of "free" nucleons, rather than an integral cluster, and that the following assumptions should hold (1) The incident particle never interacts with more than one nucleon at any one time. (2) The amplitude of each incident wave falling on each nucleon is the same as if the nucleon were a free particle. (3) The binding forces between constituent nucleons in the nucleus are negligible during the strong interaction of the incident particle with the system.

Assumptions (1) and (2) are somewhat oversimplified for systems heavier than the alpha particle. The seemingly paradoxical "impulse" assumption (3) is reconciled by the fact that for very short collision times τ, the energy E of the system cannot be determined to better than $\Delta E \sim \hbar/\tau$, a simple application of the uncertainty principle. In spite of these apparent shortcomings, the impulse approximation has been successfully used to correlate a broad spectrum of empirical data and still remains the basic assumption in models for high energy nuclear reactions.

1.2 Simple Nuclear Reactions

Simple nuclear reactions of the form (a,aN), where a is the incident projectile and N is the nucleon removed from the nucleus, have been a field of extensive investigation over the years(2), mainly because this class of reactions represents the simplest form of the cascade-evaporation model and impulse approximation outlined in the previous section. In addition, such reactions are thought to occur mainly on the nuclear surface, damage the nucleus only slightly, and are therefore, of value in probing

certain aspects of nuclear structure.

According to Grover and Caretto(2), the most commonly assumed mechanisms for (Nucleon, 2 Nucleon) reactions are: (1) Clean Knockout (CKO)-The incident nucleon penetrates into the nucleus, interacts strongly with only one nucleon, and both collision partners promptly exit the nucleus without disturbing it further(i.e. the residual excitation energy is less than the binding energy of the least bound particle in the nucleus). (2) Unclean Knockout (UCKO)-The incident nucleon penetrates the nucleus, more than one intranuclear nucleon-nucleon collision occurs, and the initial projectile and a nucleon promptly exit the nucleus (3) Inelastic Scattering followed by Evaporation of a Nucleon (ISE)-The incident nucleon promptly exists the nucleus with somewhat diminished energy and at a much later time on the nuclear scale, a nucleon emerges. (4) Charge Exchange Scattering followed by Evaporation of a Nucleon (CESE)-A nucleon of the opposite type as the original incident projectile promptly emerges from the nucleus and at a much later time on the nuclear scale, another nucleon emerges. (5) Compound Nucleus Formation followed by Evaporation of 2 Nucleons-The incident particle penetrates into the nucleus and a much later time on the nuclear scale, two nucleons emerge. (6) Pickup to form a Deuteron-The incident nucleon enters the nucleus, interacts with a target nucleon of the opposite type having about the same momentum, and both leave the nucleus as a deuteron. (7) Knockout of a Deuteron-The incident nucleon knocks a deuteron out of the target nucleus and is itself captured.

Mechanisms (1) through (4) may easily be extended to include the general class of (a,aN) reactions and in particular the (π,πN) reaction. For initial inelastic collisions in which pion production is involved,

the created particles must also escape with the initial collision partners, if a residual product one nucleon removed from the target is to be formed. For example, a (p,2p) reaction above the pion production threshold of about 400 MeV would include contributions from ($p,pn\pi^+$) and ($p,2p\pi^\circ$) for single pion production and ($p,2n2\pi^+$) and ($p,pn\pi^+\pi^\circ$) from double pion production.

Several important recoil experiments have demonstrated that simple high energy reactions of the form (a,aN) may be understood in terms of any one or a combination of the CKO,ISE, and CESE mechanisms. For the reaction $^{12}C(p,pn)\ ^{11}C$ at 450 MeV incident proton energy, Panontin and coworkers(9) have observed a monotonically decreasing, slightly forward peaked angular distribution of recoiling ^{11}C nuclei, and set a lower limit of 85% for the CKO contribution to the cross section at that energy. In a study of the $^{65}Cu(p,pn)\ ^{64}Cu$ reaction from 0.4 to 2.8 GeV incident proton energy, Remsberg(10) discovered a sidewise peak in the angular distribution for recoiling ^{64}Cu nuclei near 90°, which was ascribed to the ISE and/or CESE mechanism. An estimate of the area under the peak showed these mechanism to contribute about 30% to the total cross section, with the remaining 70% accounted for by the CKO mechanism. An evaporation calculation made in the same work estimated the CESE mechanism to be about 10% of the ISE mechanism or 3% of the total cross section. Using the same experimental technique for the $^{63}Cu(p,n)\ ^{63}Zn$ and $^{63}Cu(p,2n)\ ^{62}Zn$ reactions at 1.0 GeV, Remsberg(11) further illustrated that peaks in the angular distributions near 85° for the

angular distributions near 85° for the recoiling ^{63}Zn and ^{62}Zn product nuclei could be attributed to charge exchange and CESE mechanisms, respectively.

Other angular distribution studies of recoiling nuclei from simple high energy reactions such as $^{9}Be(p,2p)\ ^{8}Li(12)$, $^{197}Au(p,pn)\ ^{196}Au(13)$, and $^{58}Ni(p,pn)\ ^{57}Ni(13)$ lend credence to the idea that such reactions proceed predominantly by a CKO mechanism, with some contribution coming from the ISE and/or CESE mechanism. For incident projectile energies greater than 0.1 GeV/nucleon, the mechanism of compound nucleus formation, pickup to form a deuteron, and knockout of a deuteron, are not significant contributions to the reaction mechanism. While the process of unclean knockout (UCKO) has not thus far been strongly considered as a mechanism for simple reactions due to a lack of experimental data, evidence for its occurrence in $(\pi,\pi N)$ reactions will be presented in the second part of this thesis.

1.3 The Free-Particle Influence and the (p,2p) Reaction

In light of the preceding discussion, simple "knockout" reactions of the form (a,aN) are potentially feasible tools for investigating free-particle collisions in nuclear matter. From the viewpoint of the impulse approximation and the evidence obtained in angular distribution studies of recoiling nuclei, the predominant mechanism for such reactions involves a "quasi-free" knockout of a target nucleon by a high energy incident projectile, such as a proton or pion. It would be anticipated then that changes in cross section for (a,aN) type reactions should reflect to some degree corresponding changes in free-particle aN scattering cross sections.

In order to illustrate this point with a case specifically germane to this work, Fig. 1-1 displays the total free-particle pp scattering cross sections [hereafter denoted as $\sigma(pp)$] (14). The pp cross section shows marked structure in its behavior, rising in value from 24 mb at 0.3 GeV to about 48 mb at 1.0 GeV incident proton energy. This increase is attributed to increasing contributions to the total cross section by inelastic pion producing pp collisions. Above 1.0 GeV, the curved displays a gradual decrease. It was originally expected and later demonstrated (15-17) in light of the quasi-free nature of the (p,2p) reaction, that (p,2p) excitation functions in the GeV energy region should exhibit significant rises in cross section values which could be correlated to rises in $\sigma(pp)$ over the same energy region between 0.3 and 1.0 GeV, and to display little or no change above 1.0 GeV, like the corresponding $\sigma(pp)$ behavior. Previous studies have determined (p,2p) excitation functions for the target nuclei ^{57}Fe(15), ^{68}Zn(15), ^{142}Ce(16), and ^{25}Mg(17) in the GeV energy region and have illustrated the above trends, with the added observation that the rise in $\sigma(p,2p)$ is significantly less than the corresponding $\sigma(pp)$ rise. This relative flattening of the (p,2p) excitation function is explained in terms of a reduction in the effective pp cross section due to attenuation factors for the incoming projectile and outgoing particles by the nucleus.

1.4 Definition and Purpose of Project-Part I

The general objective of this work was to investigate the effect of free-particle collisions in nuclear reactions at high energy and to understand how the presence of nuclear matter (the nucleus) modifies these collisions. Part I of this thesis reports the results for measurement of

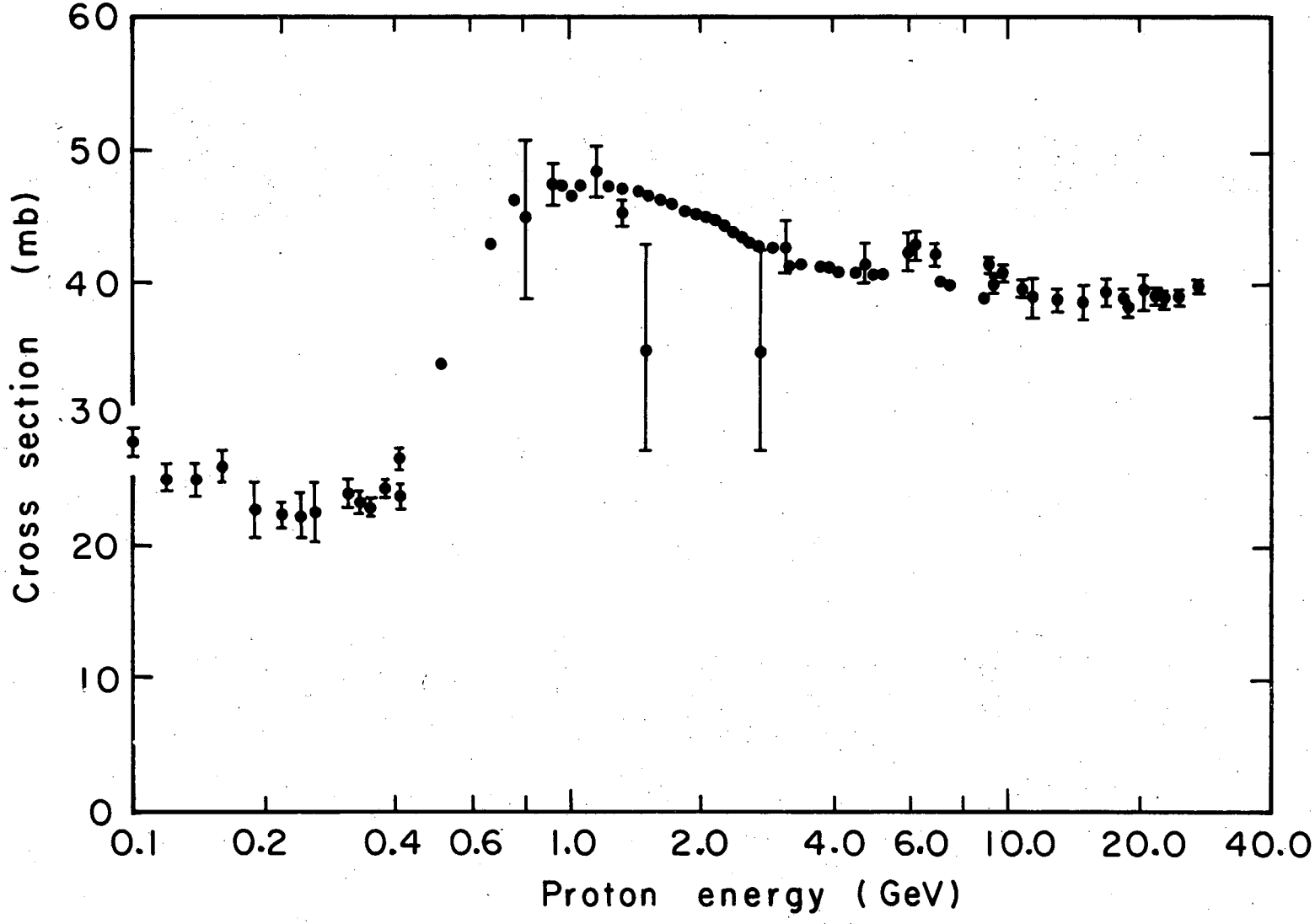

XBL755-2871

Fig. 1-1. The total free-particle pp scattering cross sections (from Reference 14).

(p,2p) excitation functions of ^{48}Ti and ^{74}Ge above 0.3 GeV incident proton energy.* This lower energy limit was chosen because it represents the onset of the rise in $\sigma(pp)$ cross sections due to pion production. Each target conveniently yielded a radioactive (p,2p) product that could be assayed without prior chemical separation. Specifically, the purpose of these proton experiments was to supplement the previous (p,2p) excitation function studies in order to gain a more complete understanding of the systematic variations or trends, if any, of the free-particle pp structure in such reactions.

Part II of this thesis will be a continuation of the broad based objective by using charged pions as the high energy projectiles to study the effect of πN collisions in the light nuclei ^{14}N, ^{16}O, and ^{19}F, with particular emphasis on the $(\pi,\pi N)$ excitation functions for these targets. A detailed background discussion on this project is deferred until then.

2. EXPERIMENTAL PROCEDURE

The general technique used in the proton phase of this work was to activate stacks of aluminum and target foils in the internal proton beams of the Lawrence Berkeley Laboratory 184-inch synchrocyclotron and the Bevatron. Subsequent counting of the foils with high resolution Ge(Li) detectors and analysis of the photopeaks and decay curves by computer code permitted reaction cross sections to be measured. The following is a detailed description of the experimental procedure.

---

*The results from the first part of this thesis on (p,2p) reactions has been published by Norman P. Jacob, Jr. and Samuel S. Markowitz, Phys. Rev. C11, 541 (1975).

2.1 Targets

All targets for this work were prepared by high temperature vacuum evaporation of the enriched oxide isotopes $^{48}TiO_2$(99.13%) and $^{74}GeO_2$ (94.5%), obtained from Oak Ridge National Laboratory, to thicknesses of 0.7-1.5 mg/cm^2 on 0.0013 cm aluminum foil. This backing provided support for the target material and served to catch forward recoiling nuclei produced from the induced nuclear reactions. Targets produced in the manner were visually uniform, produced no flaking when handled, and could be easily and cleanly cut with a scissors. The isotopic composition and elemental contamination of these oxides is shown in Table 2-1.

At the high temperatures required for this target preparation, decomposition of the oxides became a possibility. Since an accurate knowledge of target composition is required for cross section calculations, all targets were spectrophotometrically analyzed following completion of gamma counting for Ti or Ge contents (18). Generally, analysis of the targets by weighing agreed to within 10% of the results obtained from the spectrophotometric analysis.

2.2 Bombardments

The targets were activated in the internal proton beams of the 184-inch synchrocyclotron for incident proton energies from 0.3 to 0.73 GeV and the Bevatron for energies from 1.0 to 4.6 GeV.

The beam energies in each machine were determined in the following manner. In the synchrocyclotron, the target was moved along a radial line by a main probe until it intercepted the circulating internal proton beam at the desired energy. Smaller energies required a deeper radial penetration by the probe. These beam energies were known conservatively to ±4%,

Table 2-1. Mass Analysis and Chemical Composition of Target Isotopes

Target	Mass Number	%[a]	Chemical Impurities (%)[a]
^{48}Ti	46	0.25±0.02	Al, Ca, Ni, Pb < 0.05%
	47	0.26±0.02	Si < 0.02%
(TiO_2)	48	99.13±0.05	Cr, Cu < 0.02%
	49	0.19±0.02	Others negligible
	50	0.17±0.02	
^{74}Ge	70	1.71±0.10	Al, Pt, Ni < 0.05%
	72	2.21±0.10	Zn < 0.2%
(GeO_2)	73	0.90±0.05	Si < 0.03%
	74	94.48±0.10	Others negligible
	76	0.70±0.05	

[a]Taken from spectrographic analysis figures supplied by the Oak Ridge Isotope Division.

corresponding to a one inch error in radial placement of the target.[19] The average internal proton fluxes were 1μA. For the Bevatron, a beam energy was established by turning the rf oscillator off when the desired energy was reached. Targets were then flipped into position at the end of a pulse to intercept the beam. Energies determined by this method are known to ±1%.(20). Internal fluxes averaged 2×10^{12} protons per pulse with 10 pulses per minute.

The target stacks as traversed by the proton beam consisted of a 0.005 cm aluminum foil, 3 separate 0.0008 cm aluminum foils, the enriched target layer on the thin aluminum backing, and a final 0.005 cm aluminum foil. This description is illustrated in Fig. 2-1. The first and last thick 0.005 cm aluminum foils held the thinner intermediate foils together. The central 0.0008 cm aluminum foil was used as a beam flux monitor via the $^{27}Al(p,3pn)\ ^{24}Na$ reaction (21), while the forward and backward aluminum foils acted as guards and compensated for ^{24}Na recoil loss in the monitor foil. When targets of $^{48}TiO_2$ and $^{74}GeO_2$ were run simultaneously, an extra guard and target foil were included in the stack. Typical total stack thicknesses were approximately 35-40 mg/cm^2. Irradiation times were for periods of 10-20 minutes.

2.3 Counting Procedure

After each exposure, a 1.25 cm diameter circle was punched from the foil stack just back of the leading edge. This insured alignment of monitor and target foils and minimized the undesirable "leading edge effect", whereby the beam is concentrated largely on the leading edge of the foil stack. As a check on this alignment, the thick 0.005 cm front and back aluminum foils were counted after each run in an end window beta-proportional counter. After a small correction for recoil losses, the difference

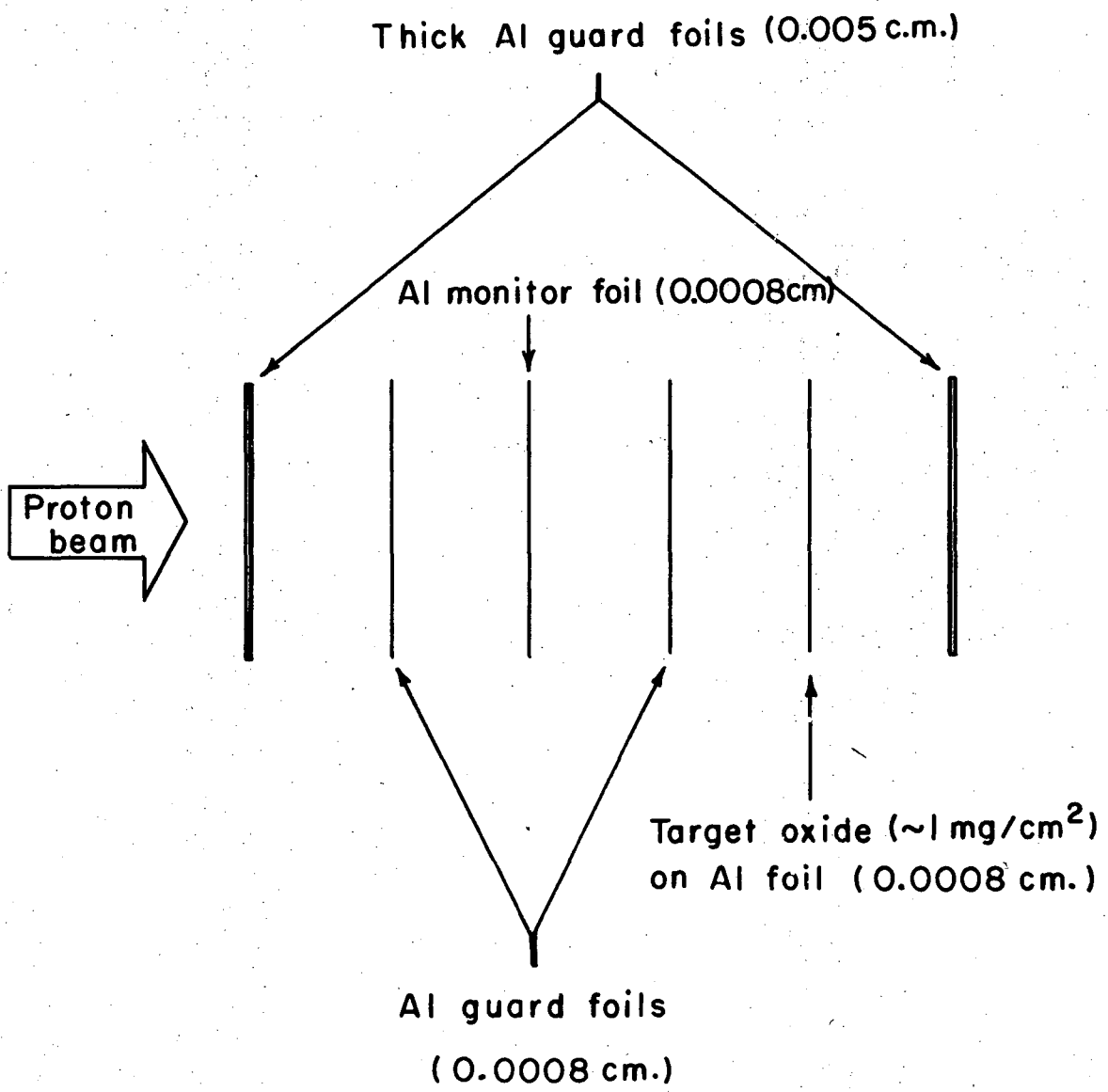

Fig. 2-1. The target stack.

Table 2-2. Decay Schematics for the Observed Radionuclides

Nucleus	Half-Life	γ-Energy(MeV)	Fraction of decays leading to γ-emission	Reference
^{24}Na	15.0 h	1.37	1.0	22,23
^{47}Sc	3.43 d	0.160	0.73	23
^{73}Ga	4.9 h	0.297	0.87	23
		0.326	0.13	23

in decay rates between the foils was invariably less than 2%. Error due to alignment was thus ignored.

The target and monitor foils were mounted on standard aluminum counting cards and the desired product nuclei were assayed by gamma ray counting with high resolution Ge(Li) detectors. The photopeaks from ^{47}Sc and ^{73}Ga were sought from the targets ^{48}Ti and ^{74}Ge respectively, while the decay of ^{24}Na produced in the aluminum was followed. The decay characteristics (22,23) for the observed nuclides are summaried in Table 2. The decay of a nuclide was monitored for two or more of its half-lives. Counting of the aluminum monitor foils and the ^{74}Ge target was begun usually 20 minutes after an exposure. For the ^{48}Ti target, counting was initiated a day or two after irradiation. This permitted shorter interfering activities to decay.

The two Ge(Li) detectors used in this work had active volumes of 20 cm^3 and 30 cm^3 and were of the planar and coaxial variety, respectivity(24). Each was carefully calibrated for efficiency as a function of gamma ray energy using a set of standard IAEA sources(25) (see Appendix A). Because all counting was done at a distance of 10 cm from the face of the detector, the 1.25 cm diameter foil would appear to the detector as essentially a point source(26). Thus, no efficiency corrections to the data for an extended disc source were necessary. For the 122 keV gamma ray of ^{57}Co, the resolution of each detector was 2 keV full-width at half-maximum (FWHM).

Electronically, each detection system was identical. The signal in a detector was first preamplified and then directed through a high rate linear amplifier used in conjunction with a biased amplifier. The output

signals were then accumulated in the memory of a Northern 1024 or Victoreen 400 channel analyzer. After a counting interval was completed, the stored gamma spectra was recorded onto either a seven inch magnetic tape or printed onto long strips of paper. For this work, the magnetic tape was used exclusively for recording the data from the ^{74}Ge experiments. Later, breakdowns in the magnetic tape-analyzer interface required a switch to printed readouts for all ^{48}Ti spectra.

2.4 Data Analysis

Figure 2-2 illustrates an energy region of interest in the gamma ray spectra from an irradiated ^{74}Ge target. All relevant photopeaks were analyzed by the computer code SAMPO(27) on the LBL CDC 6600 computer. Briefly, this program fits each photopeak to a Gaussian function with exponential tails and calculates the area (number of total net counts) under this fitted function. Also tabulated in the output is an estimate of the error in the peak area and an indication of the "goodness" of the fit to the data.

Figure 2-3 illustrates fitted photopeaks for gamma rays from ^{47}Sc and ^{73}Ga. Residuals, expressed in units of standard deviations of the data, are shown immediately below. When small and randomly distributed, these residuals are indicative of a good fit to the photopeak.

The decay curves synthesized by plotting the counting rates obtained from the photopeak analysis as a function of time were fit by the standard least squares program CLSQ(28). In all cases, only one component in the decay curve was fit, and a fixed half-life, taken from Table 2, was used in obtaining the initial activity and standard deviation of the component

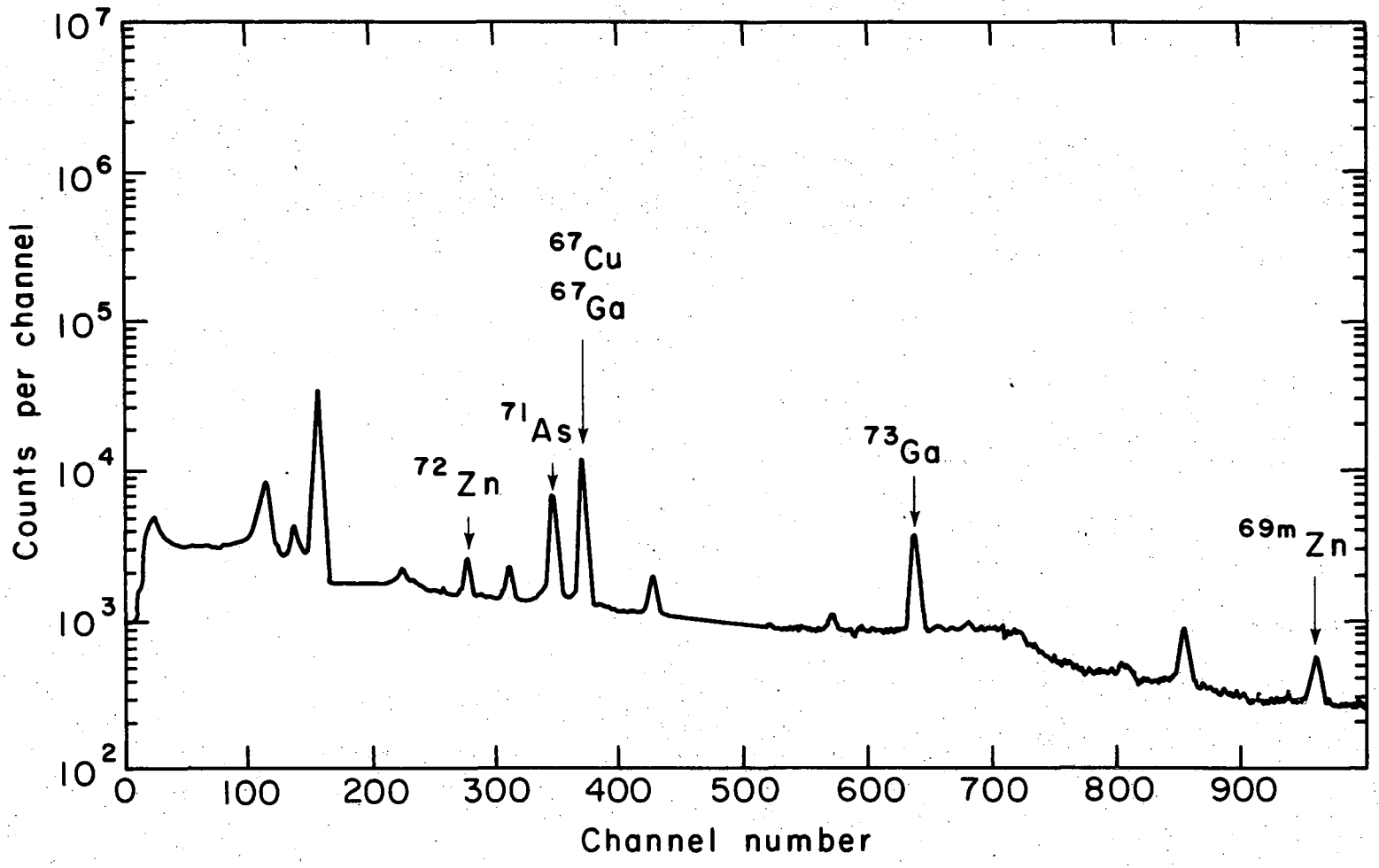

XBL756-3135

Fig. 2-2. A portion of the Gamma Energy Spectrum from an irradiated ^{74}Ge target.

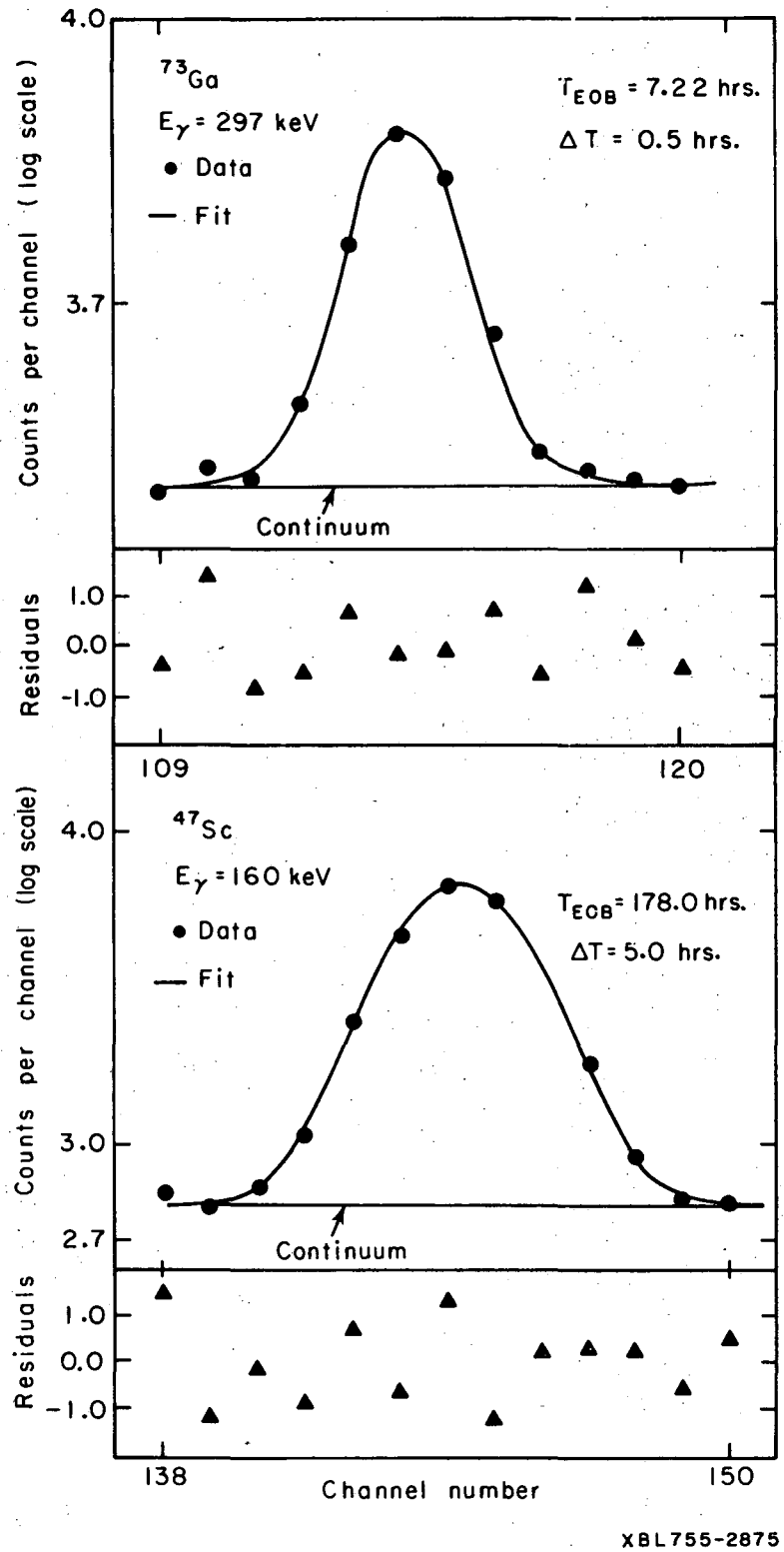

Fig. 2-3. SAMPO fitted photopeaks for ^{73}Ga and ^{47}Sc. Small and randomly distributed residuals are indicative of a good fit.

at the end of bombardment.

For ^{73}Ga, the 297 keV peak(87%) (23) was chosen for analysis rather than the 326 keV peak (13%) (23) because of its larger abundance. In addition, the small 326 keV peak was often washed almost completely out, resulting in large errors in the area analysis. An additional noteworthy fact is that ^{67}Ga ($t_{1/2}$ = 78.0 h) (23) produced in the proton bombardment of ^{74}Ge emits a gamma of 300 keV energy (16%) (23). This was difficult to resolve from the more abundant 297 keV ^{73}Ga photopeak even with the aid of the computer code. By comparison, however, it comprised less than 2% of the area of the larger peak, and its presence was ignored in the early counting.

The final reaction cross sections were calculated in the following manner. The end of bombardment activities were converted to decay rates by dividing by the Ge(Li) detection efficiency for the particular gamma ray. Saturation decay rates D_s were obtained by dividing the decay rates by a saturation factor $(1-e^{-\lambda t})$, where λ is the decay constant for a particular nuclide, and t is the length of bombardment. The equation which expresses a reaction cross section for the production of species X from target T, designated as $\sigma_T(X)$, relative to the cross section for the production of ^{24}Na from the aluminum monitor foil, designated as $\sigma_{Al}(^{24}Na)$ is given then by

$$\sigma_T(X) = \sigma_{Al}(^{24}Na) \frac{D_s(X)}{D_s(^{24}Na)} \frac{n_{Al}}{n_T} \qquad (2\text{-}1)$$

where n_{Al} and n_T are respectively, the number of aluminum monitor foil and target atoms per cm^2.

Table 3-1. Reaction cross sections.

Energy (GeV)	Individual Cross Sections (mb)	Average±s.d. (mb)	Individual Cross Sections (mb)	Average±s.d. (mb)	Free pp[a] (mb)	Monitor Cross[b] Sections (mb)
0.300±0.012	23.3,22.9,22.8, 22.9,24.5	23.3±0.3			22.5±1.5	10.1±7%
0.400±0.016			19.4,20.2	19.8±0.4	24.0±1.0	10.5
0.520±0.022	27.3,25.5,27.8, 26.9	26.9±0.5			34.0±0.2	10.7
0.730±0.029	27.9,28.4,28.1, 29.5	28.5±0.4	23.9,21.2	22.6±1.3	46.0±0.1	10.8
1.00 ±0.01	29.4,28.8	29.5±0.3	23.5,22.3	22.9±0.6	47.5±0.1	10.5
1.60 ±0.02	28.8,28.1	28.5±0.4	21.9,20.7	21.3±0.6	46.4±0.1	10.0
2.80 ±0.03	26.5,23.0	25.2±1.3	18.8,20.0	19.4±0.6	43.0±0.1	9.2
4.62±0.05	25.4,26.6	26.0±0.6	18.5,16.1	17.3±1.2	40.9±0.1	8.8

[a]Ref. 14

[b]Ref. 21.

3. RESULTS

The final reaction cross sections are summarized in Table 3-1. The monitor cross sections for the reaction $^{27}Al(p,3pn)\ ^{24}Na$, taken from the review article by Cumming(21), and the free-particle pp scattering cross sections(14) are also tabulated. The uncertainty quoted with each mean (p,2p) cross section is the mean standard deviation σ_χ and is calculated according to the formula(27)

$$\bar{\sigma}_\chi = \sum_i [(\chi_i - \bar{\chi})^2/n(n-1)] \qquad (3\text{-}1)$$

where χ_i is an individual measurement, and $\bar{\chi}$ is the mean value for a set of n measurements. Generally, these standard deviations averaged about 3% of the value of the mean cross section.

An independent estimation of important random errors to the experimental cross sections would include 1-3% for photopeak analysis, and 3% for the spectrophotometric analysis of Ti and Ge. The nonuniformity of a given target is a more difficult error to quantify, but based on the method of high temperature vacuum evaporation for target preparation, and the small area (1.25 cm^2) of the target used for analysis, a figure of 3% is assigned to this possible source of error. A root-mean-square estimated value of about 4-5% is in good agreement with the mean standard deviation figure of 3% calculated from the individual cross sections. Included among systematic errors are 7% for the monitor cross sections, 3-5% for gamma ray detection efficiency, and 1-3% for decay scheme characteristics. This yields a combined root-mean-square error in absolute cross section determination of 9-10%. In discussions of the data,

only the random errors are important in comparisons of cross section changes and trends. Systematic errors are therefore noted here, but excluded in ensuing discussions of the results.

The excitation functions for the $^{48}Ti(p,2p)\ ^{47}Sc$ and the $^{74}Ge(p,2p)\ ^{73}Ga$ reactions are presented in comparison to the total free-pp scattering cross sections in Fig. 3-1. The datum at 0.16 GeV is taken from the work of Cohen et al.(29).

4. DISCUSSION

4.1 General Features and Qualitative Interpretation of the Data

As seen from Table 3-1 and Fig. 3-1, the phenomenon of quasi-free pp scattering is demonstrated for the (p,2p) reactions of ^{48}Ti and ^{74}Ge in the GeV energy region. Each (p,2p) excitation function displays a slight but significant rise between 0.3 and 1.0 GeV, and a gradual decrease above 1.0 GeV incident proton energy. This particular structure in the excitation functions is a reflection, to a much lesser degree, as seen from Fig. 3-1, of the corresponding behavior for free-particle pp cross sections over the same energy region.

The observed rise in each (p,2p) excitation function may also be viewed as evidence for inelastic collisions contributing to the (p,2p) cross section. The single pion producing pp inelastic collisions that occur within the nucleus can be seen to be increasingly less effective in forming (p,2p) nuclei up to 1.0 GeV, and then of about equal effectiveless above 1.0 GeV, the point at which two pion production becomes important. Figure 4-1 illustrates this picture by displaying a decrease in the ratio $\sigma(p,2p)/\sigma(pp)$ between 0.3 and 1.0 GeV and a flat behavior

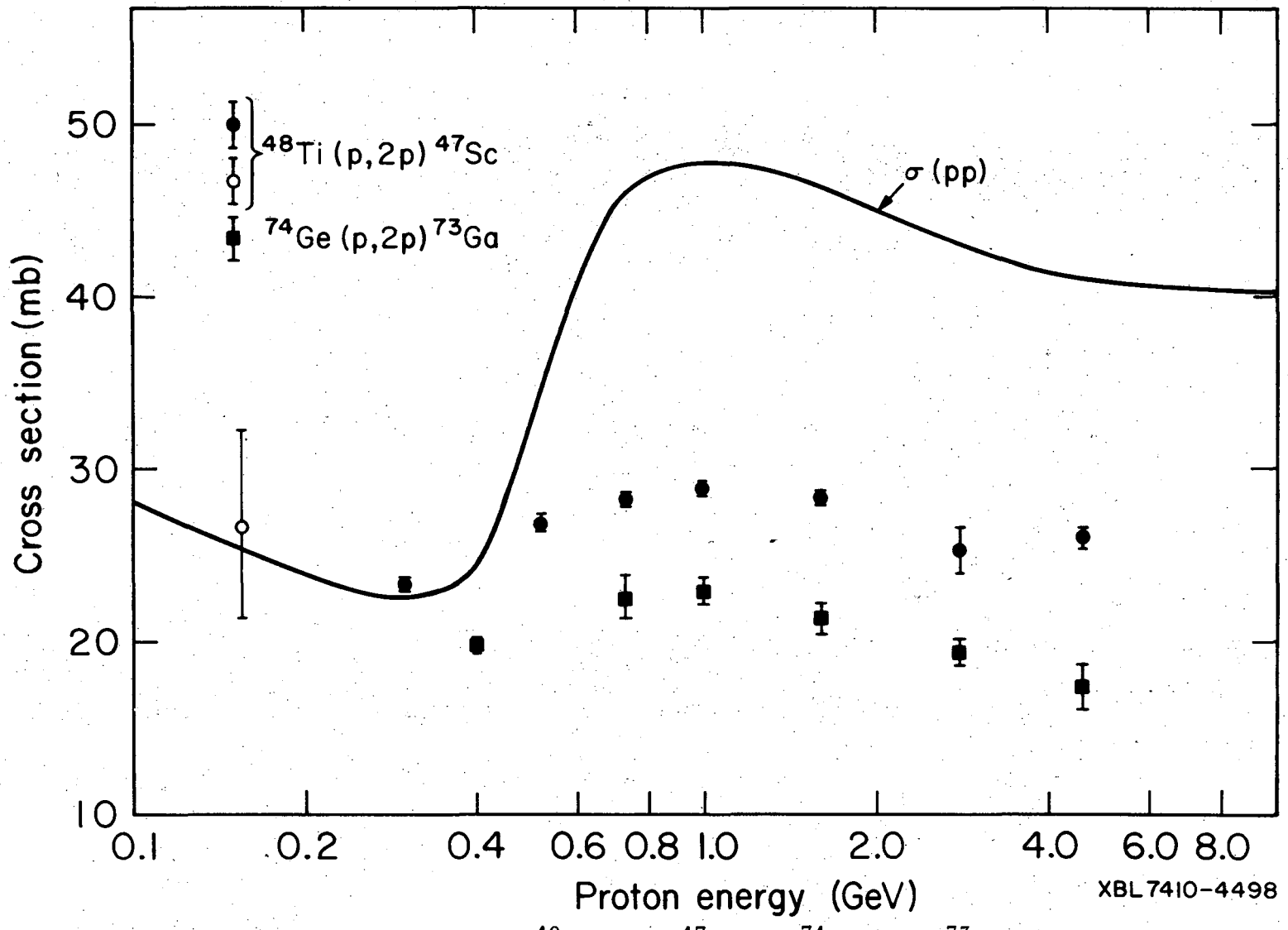

Fig. 3-1. Excitation functions for the ^{48}Ti(p,2p) ^{47}Sc and ^{74}Ge(p,2p) ^{73}Ga reactions. The open circle at 0.16 GeV is taken from Reference 29. The total cross section for pp scattering is taken from Reference 14.

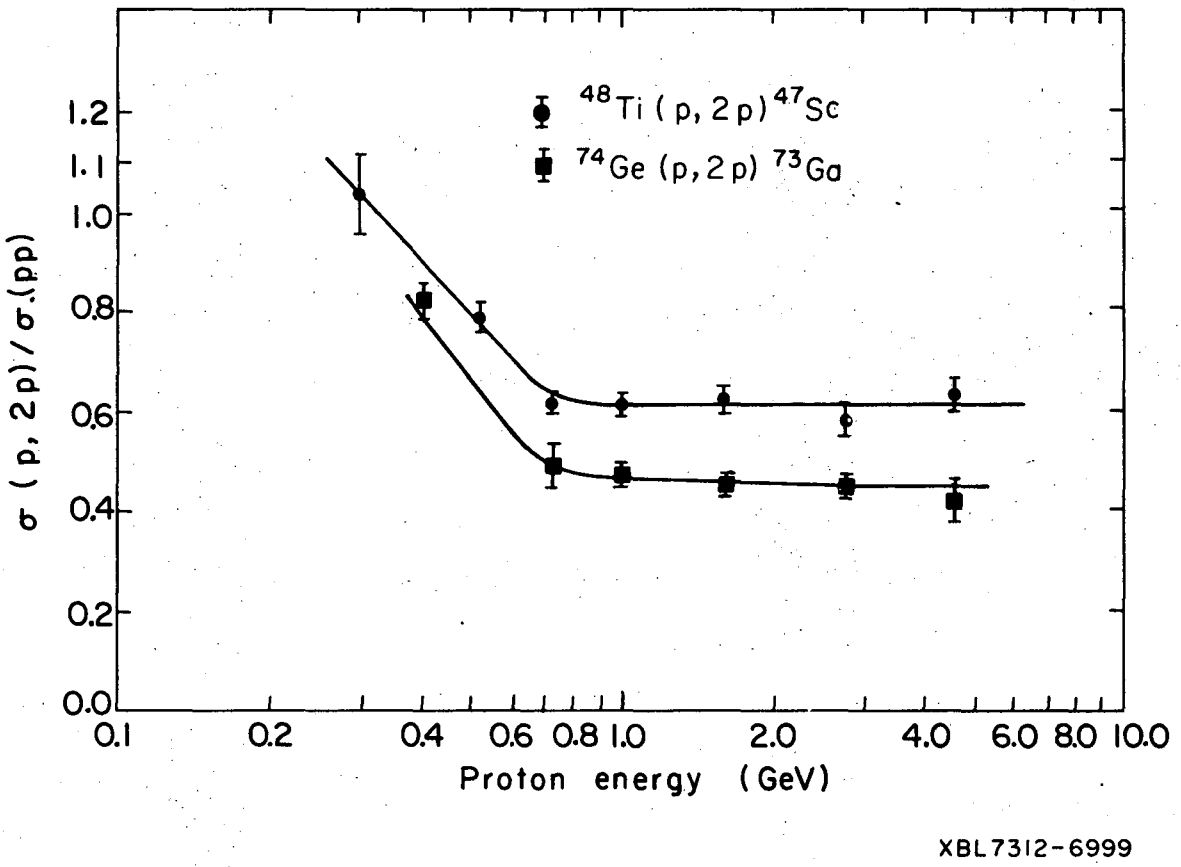

Fig. 4-1. Cross section ratios.

above 1.0 GeV incident proton energy.

A large difference of about 30% between the (p,2p) excitation function magnitudes is noted at this point and will be considered in detail later in the text.

4.1.1 Comparison to Prior (p,2p) Excitation Function Studies

Previous studies of (p,2p) excitation functions in the GeV energy region have been directed toward exploring free-particle pp scattering behavior in these reactions(15-17). The work of Reeder on the $^{57}Fe(p,2p)$ ^{56}Mn and $^{68}Zn(p,2p)$ ^{67}Cu excitation functions in the GeV energy region was the first to correlate the increase in (p,2p) cross sections above 0.4 GeV with free-pp cross section structure. A study of the $^{142}Ce(p,2p)$ ^{141}La excitation function by Meloni and Cumming(16) showed the cross sections to increase about 50% in going from 0.4 to 1.0 GeV, and then to gradually decrease above 1.0 GeV incident proton energy. A later investigation by Reeder(17) on the $^{25}Mg(p,2p)$ ^{24}Na reaction above 0.4 GeV incident proton energy indicated about a 20% increase in cross section. Cross sections determined by Caretto(30) for the $^{118}Sn(p,2p)$ ^{117}In reaction displayed a rise between 0.22 and 0.6 GeV. In addition to these studies, the $^{18}O(p,2p)$ ^{17}N reaction has cross sections of 14.5, 30.4, and 25.1 mb at 0.16, 1.0, and 2.8 GeV incident proton energy,[31,32] respectively.

In Table 4-1, the ratios of the (p,2p) cross section at 1.0 GeV to the (p,2p) cross section at or near 0.4 GeV incident proton energy for prior and present work are summarized. The increases in relative (p,2p) cross section for the targets in the present study are in excellent agreement with that determined by Reeder for the $^{25}Mg(p,2p)$ ^{24}Na

Table 4-1. Ratio of (p,2p) cross section at 1.0 GeV to the cross section at 0.4 GeV for various targets.

Reaction	$\sigma_{1.0}/\sigma_{0.4}$	Reference
free pp	1.98±0.08	14
$^{25}Mg(p,2p)^{24}Na$	1.19±0.05	17
$^{48}Ti(p,2p)^{47}Sc$	1.17±0.03	Present Work[a]
$^{57}Fe(p,2p)^{56}Mn$	1.40±0.31	15[b]
$^{68}Zn(p,2p)^{67}Cu$	1.46±0.22	15[b]
$^{74}Ge(p,2p)^{73}Ga$	1.16±0.04	Present Work
$^{142}Ce(p,2p)^{141}La$	1.47±0.13	16

[a]Cross section at 0.4 GeV is interpolated from excitation function.

[b]This ratio represents $\sigma_{0.74}/\sigma_{0.42}$.

reaction.(17) Although there appears to be no obvious trend from inspection of these tabulated results, an estimated increase of about 30% in (p,2p) cross section above 0.4 GeV incident proton energy may be predicted for any target nucleus independent of mass number. This trend implies that the surface (where simple knockout reactions are throught to occur and which enhances the cross section with increasing target mass number) to volume effects (which tend to decrease the knockout cross section through attenuation of incident and outgoing particles) neither enhance nor suppress (p,2p) cross section structure in a target nucleus regardless of mass number. Such an implication is surprising in view of the approximate $A^{-1/3}$ variation of the surface to volume ratio for the nucleus. Further accurate (p,2p) excitation function measurements above the meson production threshold for targets heavier than ^{142}Ce would serve to test this idea more rigorously. For example, ^{186}W and ^{238}U would be potential candidates in such a study and in addition, may be easily obtained in convenient foil form.

4.1.2 Magnitudes of (p,2p) cross sections

The (p,2p) cross sections measured for ^{48}Ti and ^{74}Ge are comparable in magnitude to other activation (p,2p) cross sections in the GeV energy region(33). A particularly striking feature, however, as seen from Fig. 3-1, is that the cross sections for the $^{48}Ti(p,2p)^{47}Sc$ reaction are consistently 30% higher than those for the $^{74}Ge(p,2p)\ ^{73}Ga$ reaction.

Such differences in cross sections for simple nuclear reactions at GeV proton energies are difficult to understand, especially considering that the absolute cross sections are based on gamma ray branching ratios that may introduce error. Plausible explanations for the trends in cross

section magnitudes in simple reactions have previously embraced a number of ideas, four of which are applied to the results from this work and discussed in the following sections.

4.1.2A Stability of the Residual Nucleus

In view of the cross section differences, it is conceivable that the residual ^{73}Ga nucleus may be more unstable with respect to particle emission than ^{47}Sc, following deposition of the about 10 MeV or less of post-knockout excitation energy in each system. If this hypothesis were correct, then the depletion of the ^{73}Ga yield relative to ^{47}Sc could qualitatively be understood by comparing nucleon and particle binding energies in each of these nuclides.

A concrete example of this would be the anomalously low cross sections observed for the ^{14}N(p,pn) ^{13}N reaction at GeV energies.(33) Because the proton binding energy in ^{13}N (1.95 MeV)(34) is less than its first excited state (2.37 MeV),(35) the residual excited ^{13}N nucleus would be unstable to proton emission with the deposition of 2.37 MeV or more of excitation energy.

Table 4-1 presents a summary of the binding energies for different particles in the residual ^{47}Sc and ^{73}Ga nuclei. The last two rows designated (V_p+S_p) and $(V_\alpha+S_\alpha)$ are respectively, the sum of the proton separation energy and the Coulomb barrier for a proton in each nucleus, and the sum of the alpha particle separation energy and the Coulomb barrier for and alpha particle in each nucleus. These two quantities represent the "effective" separation energies for protons and alphas in these nuclei. This comparison of binding energies shows (i) That if an evaporation from a post-knockout ^{47}Sc or ^{73}Ga does occur, the most likely

Table 4-2. Binding Energies of Various Particles in the Observed Nuclides

Particle	Separation Energy (MeV)[a]	
	^{47}Sc	^{73}Ga
n	10.6	9.2
p	8.5	8.9
α	10.1	6.2
2n	19.4	15.8
2p	22.3	——
(V_p+S_p)[b]	14.1	16.1
$(V_\alpha+S_\alpha)$[b]	17.5	16.4

[a]Reference 34.

[b]Assumes r_0 = 1.44 F for calculation of Coulomb barrier

candidate for emission would be a neutron. (ii) The binding energies for the neutrons in the residual nuclei are very similar and HIGH in comparison to an expected residual excitation energy of 10 MeV maximum. Thus, these two residual nuclei are expected to be stable with respect to further particle evaporation if 10 MeV or less of excitation energy remains. One is then left with the possibility that a shift in the excitation energy spectrum to higher residual cascade energies would be required for ^{73}Ga relative to ^{47}Sc. to explain the large difference in (p,2p) cross sections. Such a difference is unlikely in view of the low momentum transfer, low energy deposition characteristics of the (a,aN) knockout reactions in general.

NOTE: Monte Carlo cascade calculations performed for incident 0.73 and 1 GeV protons on ^{48}Ti and ^{74}Ge target nuclei show that the excitation energy spectra for cascade products having one mass number less than these targets are essentially identical. This information was extracted from the standard computer calculation, which was performed as part of this project to calculate reaction cross sections. These computed cross sections are presented later in the text.

4.1.2B Number of Bound Levels in the Residual Nucleus

This concept can be an important factor in influencing the yield of a nuclide formed in a nuclear reaction. The cross sections measured in this work are in reality, equal to the sum of the individual cross sections for the formation of all bound residual nuclear states, both ground and excited. Therefore, the number of excited bound levels decaying to the ground state (which outside of long-lived isomeric states is the only state measured in activation) would effect the integral

cross section. For example, anomalously low $^{14}N(p,pn)\ ^{13}N$ cross sections may also be ascribed to the fact that only the ground state of ^{13}N is formed. All excited states in this nucleus are unbound,(35) and thus cannot feed the ground state and contribute to the observed cross section.

According to the information in Nuclear Data Sheets(36), ^{47}Sc has 45 particle bound excited levels below the proton separation energy of 8.5 MeV, while ^{73}Ga has only its ground state listed. Several excited states for ^{73}Ga have recently been found by Erdal and co-workers(37) in a study of the β^- decay of ^{73}Zn. It is obvious that additional excited states do exist, but are not yet known. This information would be necessary in determining the importance of this proposal.

4.1.2C Neutron Skin Thickness

The concept of a neutron skin thickness has been presented as a suitable explanation by Caretto and co-workers(38,39) for (p,pn) and (p,2p) cross section trends across a row of cadmium and tellurium isotopes. The "thin" neutron skin hypothesis has been discussed by Karol and Miller(40) in relation to the anomalously low $^{58}Ni(p,pn)\ ^{57}Ni$ cross section (30 mb at 0.4 GeV compared to a "normal" value of 60 mb).

Such a hypothesis may be applied to the targets in the present work. The neutron skin thickness t_n, derived according to the theory of the Droplet Model,(41) is defined as the difference between the radii of the spheres corresponding to the proton and neutron density distributions, and is quantitatively given by

$$t_n = (2/3)r_0A^{1/3}(I-\bar{\delta}) \qquad (4\text{-}1)$$

where $I=(N-Z)/A$ and $\bar{\delta} = (I + k_1 Z^2 A^{-5/3})/(1 + k_2 A^{-1/3})$, with k_1 and k_2 being known constants, and r_0 the nuclear radius constant. If the nuclei along beta stability are defined as having "normal" neutron skin thickness, then $I = 0.4A/(200+A)$ (34) can be used as an approximation to the valley of beta stability.

Table 4-2, generated by applying Eq. 4-1 with $k_1 = 0.01117$, $k_2 = 3.15$, and $r_0 = 1.16F$, summarizes the neutron skin thickness for "normal" beta stable nuclei with mass numbers 48 and 74, and for ^{48}Ti and ^{74}Ge, the target isotopes in this study. In comparison to the neutron skin thickness for A = 74, ^{74}Ge displays a neutron skin thickness which is 29% higher than "normal". In contrast, ^{48}Ti shows only a slight increase of 9% over the "normal" neutron skin thickness for A = 48. According to the Droplet Model, these figures imply that on the average, the protons in ^{74}Ge are closer to the center of the nucleus than usual, while the protons in ^{48}Ti have a more usual distribution. Since knockout reactions are thought to occur on the nuclear surface, such a circumstance would be a plausible explanation for the observation of smaller (p,2p) cross sections for ^{74}Ge than for ^{48}Ti.

Some caution should be taken in postulating the variation in (p,2p) cross sections with neutron skin thickness, because this idea is not clearly separable from the increasing particle attenuation factors associated with larger nuclei.

4.1.2D Shell Structure and Proton Availability

A theory incorporating shell structure effects to explain (p,pn) cross section magnitudes was first developed by Benioff(42). This theory

Table 4-3. A Comparison of Neutron Skin Thicknesses

	"Normal" A=48	^{48}Ti	"Normal" A=74	^{74}Ge
$t_n(F)$	0.088	0.096	0.133	0.172
$\Delta\%^a$	+9.1		+29.3	

$$a_{\Delta\%} = \frac{(t_n(X) - t_n(\text{Normal})) \times 100}{t_n(\text{Normal})}$$

was used later by Porile and Tanaka(43) in a study of (p,pn) reactions on medium mass nuclei to demonstrate that the drop in σ(p,pn) between N = 40-42 was due to the sudden "unavailability" of the eight $1f_{7/2}$ neutrons, i.e., sudden removal of a neutron from this level would leave a "hole", resulting in evaporation of a particle (neutron), and thereby destroying the (p,pn) product. For (p,2p) reactions, the coincidence detection of outgoing protons has clearly shown that quasi-free scattering of the incident proton occurs from bound proton shells.(44,45).

For purposes of exploring possible shell structure effects on the cross section magnitudes in this work, a calculation of relative (p,2p) cross sections for ^{48}Ti and ^{74}Ge was made by applying the theory of Benioff to these reactions. In analogy to the (p,pn) reaction, the cross section for a (p,2p) reaction in the GeV region would be given by

$$\sigma(p,2p) = k \sum_{\substack{\text{allowed} \\ \text{shells}}} N_{n1j} M_{n1} \qquad (4\text{-}2)$$

where k is a constant proportional to the effective pp scattering cross section (defined as the free pp cross section reduced by Pauli Exclusion factors) in a particular nucleus, N_{n1j} is the number of available protons in the n1j shell, and M_{n1} is the fractional availability or the probability per proton that the incident proton collides with an n,1 proton and all collision products escape the nucleus without further interaction.

Three important assumptions were made in order to perform the calculation (i) The effective pp cross sections in ^{48}Ti and ^{74}Ge were equal (ii) The nuclear radius parameter r_0 was set equal to 1.20F(consistent with r_0 values for medium mass nuclei measured by electron scattering)

(iii) The variable M_{nl} was equal for target neutrons and protons. This last assumption may not be strictly applicable for bound proton shells. The overall approach, however, should yield some idea about relative cross section magnitudes.

Finally, available proton shells were chosen for ^{48}Ti and ^{74}Ge from experimental binding energies summarized by Millener and Hodgson(46) and Riou(45). The shell model calculations of Ross et al (47) were also used as a guide. From this information, it was determined that each nucleus has the following available protons:

^{48}Ti $\quad 1f_{7.2}(2),\ 1d_{3/2}(4),\ 2s_{1/2}(2),\ 1d_{5/2}(6)$

^{74}Ge $\quad 2p_{3/2}(4),\ 1f_{7/2}(8),\ 1d_{3/2}(4),\ 2s_{1/2}(2)$.

From Eq. 4-2 and the fractional availability charts in the paper by Benioff(42), a calculation of relative (p,2p) cross sections yields

$$\frac{\sigma\ ^{48}Ti(^{47}Sc)}{\sigma\ ^{74}Ge(^{73}Ga)} = 0.9$$

in contrast to the experimental ratio of 1.3. It is thus concluded that the availability of proton shells may not be a satisfactory explanation for the differences in (p,2p) magnitudes.

4.1.2 E Summary

1. Proposals based on the stability of the residual nucleus and shell structure effects in the target do not successfully reflect the experimental result that the (p,2p) cross sections for ^{48}Ti are systematically 30% higher than those for ^{74}Ge.

2. Sufficient data on the existence of excited bound states for ^{73}Ga does not exist presently to determine if this phenomenon is a factor in its yield.

3. An argument based on neutron skin thickness, calculated by formulas derived from the Droplet Model of the Nucleus, shows that the proton distribution in ^{74}Ge may be more recessed from the nuclear surface than usual, and correspondingly, results in lower (p,2p) cross sections for ^{74}Ge than for ^{48}Ti. Of the above mentioned considerations, this is the most plausible, although it does not quantitatively predict the 30% difference in cross section magnitudes.

4.2 Monte Carlo Calculations

Since the electronic computer calculations of Metropolis et al. (48,49), much work has followed in implementing the Monte Carlo technique to simulate the cascade-evaporation model of high energy nuclear reactions. The overall scope of the effort has been to correlate a large body of cross section data to this general model. To date, refinements in the details of the model have been made to the extent that very good agreement is generally obtained with experimental studies involving high energy protons and pions on a variety of target nuclei (50-55) for more complex reactions.

The (p,pn) reaction has been a particular concern in these calculations. Since this reaction is thought to occur mainly on the nuclear surface, a calculated (p,pn) cross section would be expected to be sensitive to the choice of nuclear model representing the target. For example, the calculations of Metropolis(49), using a constant density nuclear model, yielded (p,pn) cross sections a factor of 2 to 3 lower than the radio-

chemical data. Recent Monte Carlo calculations, incorporating realistically improved nuclear models(50,52,53) have achieved good agreement with experimental (p,pn) cross sections.

In contrast, (p,2p) reactions have not received such attention. Comparisons between experimental and Monte Carlo calculated cross sections are sparse. In addition, these calculations have been confined to incident proton energies less than the pion threshold of about 350 MeV (17,53). Thus far, there exists no (p,2p) cross section calculations in the literature above this energy. It would be of considerable interest to determine if the Monte Carlo cascade-evaporation calculation above 0.3 GeV would predict the same energy dependence behavior observed for experimental (p,2p) excitation functions above the pion production threshold.

As part of this study, (p,2p) cross sections for ^{48}Ti and ^{74}Ge up to 1 GeV incident proton energy were performed, using the intranuclear cascade model of Harp(55) (HIGH ENERGY VEGAS-ISOBAR hereafter referred to as HEVI) coupled to the evaporation code of Dostrovsky et al.(56) (hereafter referred to as DFF). This cascade model is an extension to 1 GeV incident projectile energy if the earlier VEGAS ISOBAR code (hereafter referred to as LEVI)(54). A brief review of HEVI and DFF codes is given in the following section.

4.2.1 The HEVI model(55)

The low energy VEGAS ISOBAR Model (LEVI) was developed by Harp et al. (54) to include the elastic formation and subsequent decay or interaction of (3,3) pion-nucleon isobars in the cascade stage of high energy nuclear reactions. Previous cascade studies(49,51,52) assumed immediate isobar

incorporated. Since only single pion and thus single isobar production are considered, the HEVI code was not extended beyond 1 GeV, the point above which double pion production becomes important.

4.2.2 The DFF evaporation code(56)

The cascade nuclei from the HEVI program are subsequently used as the initial input to the Monte Carlo DFF evaporation program(56). For a given A and Z input, the relative emission probabilities for neutrons, protons, deuterons, tritons, ^{3}He, and ^{4}He were computed according to derived expressions for the emission widths (one is referred to Eqs. 15 and 16 in reference 56 for these expressions for the emission widths for neutrons and charged particles). After normalization of these probabilities to 1, the type and kinetic energy of the evaporated particle are selected by a random number between 0 and 1, and this process is then repeated as a starting point. The evaporation was terminated when none of the maximum values of the emitted nucleon kinetic energies exceeded 0, and a new evaporation was started with the original A,Z, and E. Gamma emission could occur when particle emission was energetically prohibited, but was not allowed to compete above this limit. The details in the development of this code are contained in the original paper(56).

4.2.3. Computational Procedure

For each nucleus, 5000 incident cascades were performed at each incident experimental energy below 1 GeV. The input information included the total energy of the projectile (kinetic plus rest mass energy), atomic and mass numbers of the target, average binding energy of the last nucleon (taken as the arithmetic mean of the last neutron and proton binding energies), and a cutoff energy for isobars, which in this calculation was

set equal to the sum of the Coulomb barrier for a proton in the target nucleus plus the average binding energy of the last nucleon. The pion potential was set equal to 25 MeV and the process of isobar exchange scattering was ignored. Each of these last two choices was followed based on the recommendation in the paper by Harp(54).

The following DFF code performed 10 evaporation cascades for every excited residual nucleus for all calculations. The level density parameter was taken to be $a = A/20$, where A is the target mass number.

Generally, the following information was listed as standard output from the HEVI-DFF program (1) each cascade nucleus, including transparencies, with respective Z,A, excitation energy, and the kinds of particles emitted in the cascade as well as an indication of whether a formed isobar escaped, decayed, or was captured. (2) The average number of protons, neutrons and pions emitted per inelastic cascade. (3) The number of protons, neutrons, and pions emitted in kinetic energy intervals of 10 MeV. (4) Angular distribution of emitted protons, neutrons, and pions. (5) Excitation energies in 25 MeV intervals versus change in the mass number of the target. (6) The total number of emitted isobars. (7) Cross sections for the formation of all possible nuclei. (8) Mass and charge distributions. The emphasis of this work was on point (7).

4.2.4. Comparison of Experimental Trends

The calculated and experimental cross sections are presented in Figs. 4-2 and 4-3. Included in the plots for contrast are computed (p,pn) cross sections. Errors on the calculated cross sections are statistical and are given by the Monte Carlo code.

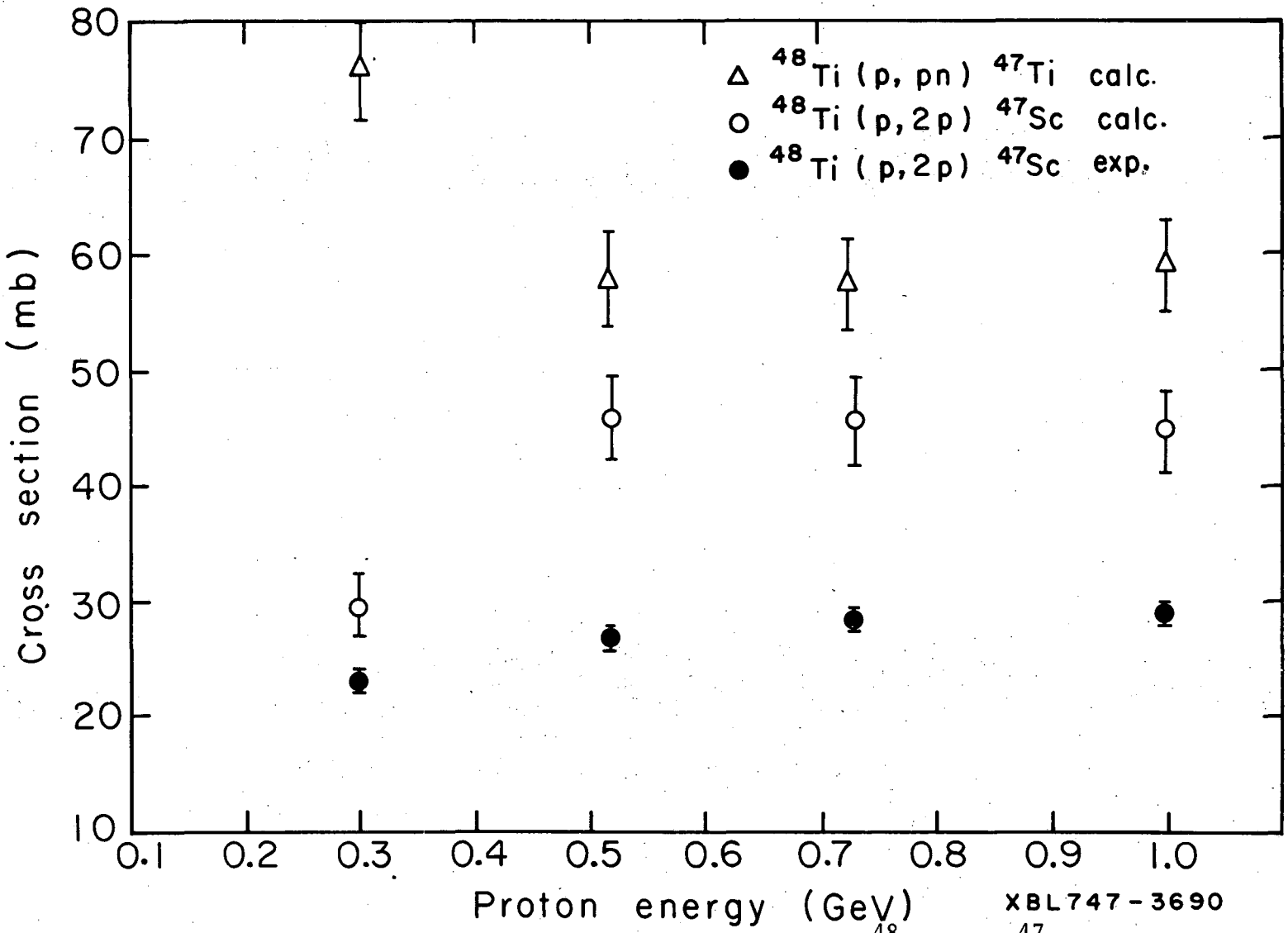

Fig. 4-2. Calculated and experimental cross sections for the $^{48}Ti(p,2p)\ ^{47}Sc$ reaction. The $^{48}Ti(p,pn)\ ^{47}Ti$ cross sections, calculated using the same model are also added to the plot for comparison.

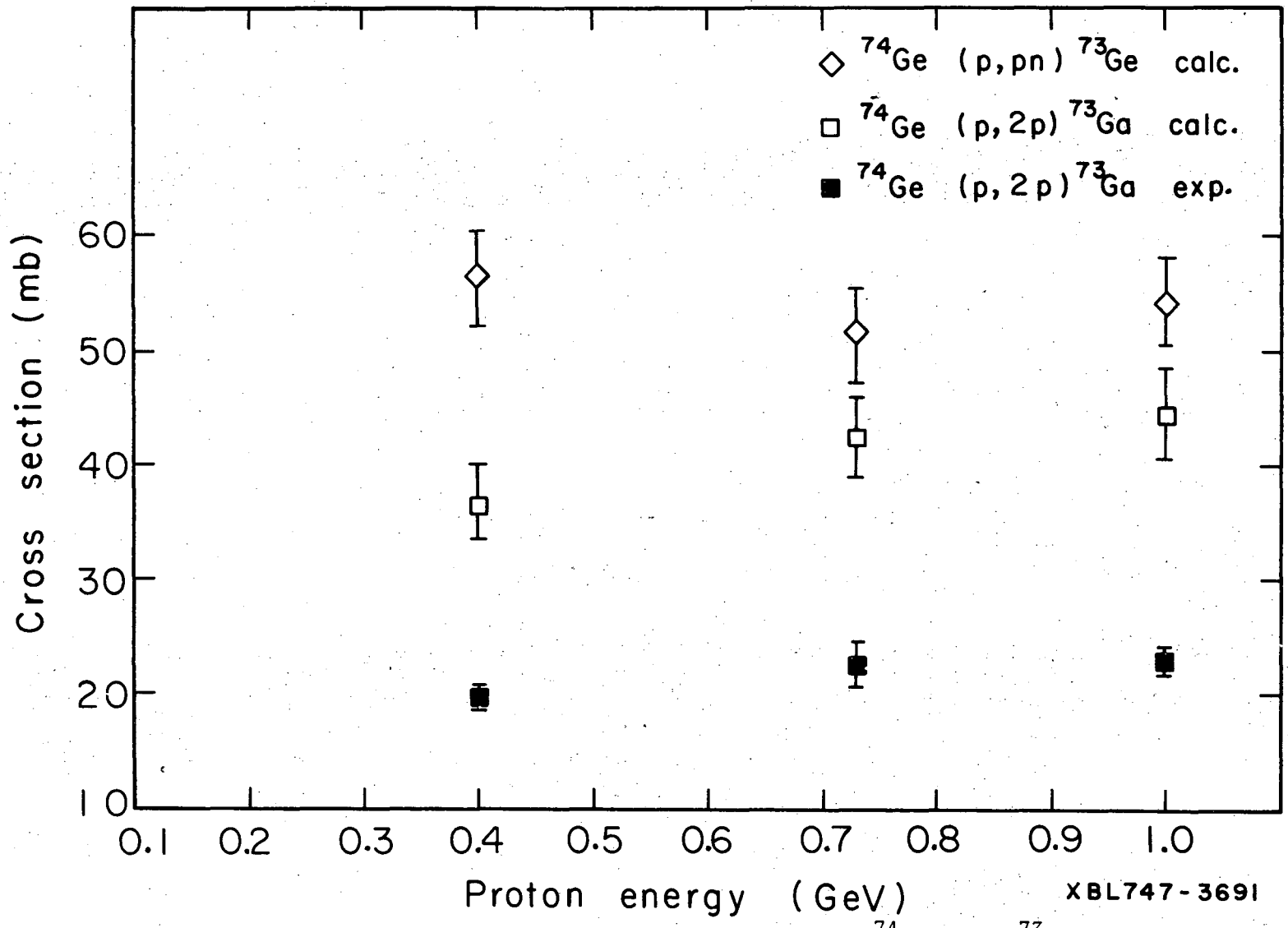

Fig. 4-3. Calculated and experimental cross sections for the ^{74}Ge(p,2p) ^{73}Ga reaction. The ^{74}Ga(p,pn) ^{73}Ge cross sections, calculated using the same model, are also added to the plot for comparison.

decay after formation. In this model, two possible modes of isobar interaction are considered (1) Isobar capture, schematically written as $\Delta + N_1 \rightarrow N_2 + N_3$, where Δ is the isobar and N is a nucleon (2) Isobar-Nucleon "exchange" scattering, written as $\Delta_1 + N_1 \rightarrow \Delta_2 + N_2$, whereby both the charge and mass of the isobar may change.

As in the original VEGAS code by Chen et al.(53) the nuclear radial density distribution is represented by a step function. Consequently, this introduced the processes of reflection and/or refraction of the incoming and outgoing particles. Both possibilities were ignored in the calculation.

The pion-nucleus potential was constant, attractive, and determined in the LEVI program(54) to be a "best" value of 25 MeV. Potentials for isobar-nucleus interactions were taken as the sum of proton and pion potentials for positively charged isobars and the sum of neutron and pion potentials for negatively charged isobars.

Only T = 3/2 pion-nucleon interactions were allowed. Cross sections used for these interactions were elementary particle pion-nucleon total cross sections. Cross sections for $\pi^\circ n$ and $\pi^\circ p$ were taken to be the arithmetic mean of $(\pi^+ p)$ and $(\pi^- p)$ cross sections.

Finally, differential cross sections for isobar decay, isobar capture, and isobar-nucleon "exchange" scattering were built into the code for these processes. The derivation of the angular distributions for each of these processes is described in detail elsewhere(53,54).

Modifications to the above described LEVI model to extend the code to 1 GeV incident projectile energy are described in detail in a subsequent paper by Harp(55). In the HEVI model, the formation of (3,3) isobars from inelastic nucleon-nucleon and pion-nucleon collisions is

In order to bring the combined experimental and computer results into a general picture which concisely emphasizes cross section changes, excitation function shapes, and comparisons to free pp cross sections, the following procedure was employed: The Monte Carlo results for the ^{74}Ge(p,2p) ^{73}Ga reaction were multiplied by a factor of 1.06 so as to place these points on the uppermost smooth universal "calculated (p,2p) curve" with the ^{48}Ti(p,2p) ^{47}Sc Monte Carlo results, illustrated in Fig. 4-4. Multiplication of the experimental ^{74}Ge(p,2p) ^{73}Ga data up to 1 GeV by 1.27 would place these points on a universal "experimental (p,2p) curve, immediately below. Likewise, the "calculated (p,pn) curve" is obtained by vertically shifting the Monte Carlo results for the ^{74}Ge(p,pn) ^{73}Ge reaction up by a factor of 1.11 to smoothly mesh with the ^{48}Ti(p,pn) ^{47}Ti data. Plotted at the bottom of the figure is the free pp cross section.

The above analysis may be summarized (i) The general energy dependence of (p,2p) cross sections above the pion threshold is correctly predicted by the Monte Carlo calculation. The experimentally observed rise in σ(p,2p) for ^{48}Ti and ^{74}Ge is, however, substantially smaller than the HEVI calculations indicate. Quantitatively, for each target, the relative increases in going from 0.3 to 1.0 GeV are (25±3)% experimentally to (51±19)% theoretically (ii) The HEVI-DFF results are generally a factor of two larger than the experimental values (iii) Both the experimental and calculated σ(p,2p) rises are significantly smaller than the free pp rise of (98±8)% over the same energy region. Again, this observation may be interpreted as evidence for attenuation of the incoming projectile and outgoing particles by the nucleus (iv) The shapes of the two experi-

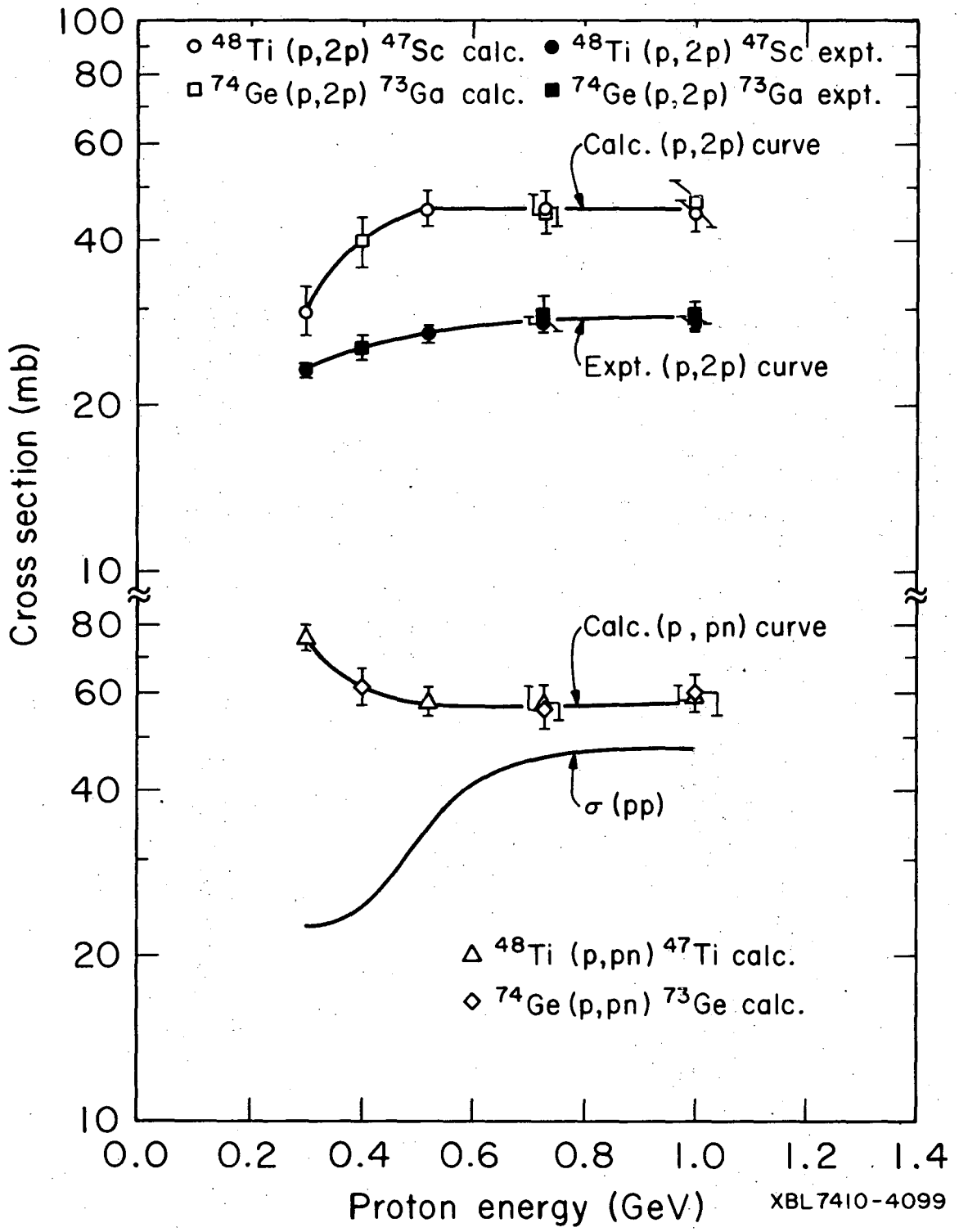

Fig. 4-4. Comparison of cross section changes and excitation function shapes. The "experimental" and "calculated (p,2p) curves" were obtained by normalizing the ^{74}Ge(p,2p) ^{73}Ga results to the ^{48}Ti(p,2p) ^{47}Sc results up to 1 GeV. In a similar fashion, the (p,pn) Monte Carlo results for ^{74}Ge were normalized to those for ^{48}Ti to yield the smooth "calculated (p,pn) curve". Plotted at the bottom is the free-pp cross section over the same energy region.

(p,2p) excitation functions and the two theoretical excitation functions are similar. The above analysis shows the experimental ^{48}Ti(p,2p) ^{47}Sc cross sections to be systematically about 27% larger than those for the ^{74}Ge(p,2p) ^{73}Ga reaction. The HEVI-DFF calculations predict a (p,2p) cross section increase for ^{48}Ti in the same direction, but only by 6%. (v) The "calculated (p,pn) curve" shows a significant drop above 0.3 GeV as opposed to the rising "experimental (p,2p) curve". It is noted here that this behavior reflects changes in the elementary pn scattering cross sections over the same energy region(14). The calculation also predicts a large (p,pn) cross section for ^{48}Ti than for ^{74}Ge by about 11%.

4.2.5. Other Interesting Results of the Calculation

A very interesting by-product of the HEVI code is the contribution of pion-producing colisions and isobar formation to the total (p,2p) cross sections. Such information is summarized in Table 4-2, where $\sigma(pn\pi^+)$ and $\sigma(2p\pi^\circ)$ denote cross sections for producing the individual particles in parentheses, and $\sigma(nI^{++})$ and $\sigma(pI^+)$ are respectively, the cross sections for production and escape of doubly charged $(p+\pi^+)$ and singly charged $(p+\pi^\circ$ or $n+\pi^+)$ isobars and their partner nucleons. The figures in this tabulation imply that (i) Inelastic collisions do contribute to the total (p,2p) cross section, as stated in Section 4.1. According to the computation, inelastic collisions make essentially no contribution to the (p,2p) cross section below 0.4 GeV, but above this energy, constitute an increasing fraciton of the cross section (ii) Above 0.5 GeV, the contribution from isobar formation becomes strikingly large, being responsible for about 12-20% of the (p,2p) cross section between 0.7 and 1 GeV incident proton energy. This particular result confirms the plausibility of isobar

Table 4-4. Inelastic contributions to the (p,2p) cross section from the HEVI program

Proton Energy (GeV)	Cross Sections (mb) $\sigma(pn\pi^+)$	$\sigma(2p\pi^\circ)$	$\sigma(nI^{++})$	$\sigma(pI^+)$	$\sigma_{inel}(p,2p)$	Inelastic (p,2p) Fraction = $\sigma_{inel}(p,2p)/\sigma_{TOTAL}^{(p,2p)}$
^{48}Ti[a]						
0.300	0	0	0	0	0	0
0.520	4.1±1.0	0.5±0.4	0.5±0.4	0.3±0.3	5.4±1.2	0.117±0.027
0.730	10.2±1.6	3.3±0.9	2.3±0.8	0.3±0.3	16.1±2.0	0.349±0.050
1.00	10.7±1.7	2.0±0.7	3.3±0.9	2.0±0.7	18.0±2.2	0.399±0.057
^{74}Ge[b]						
0.400	0	0	0	0	0	0
0.730	9.7±1.7	2.4±0.8	4.6±1.2	1.2±0.6	17.9±2.1	0.422±0.061
1.00	7.6±1.5	2.4±0.8	7.9±1.5	0.9±0.5	18.8±2.3	0.424±0.062

[a] Only inelastic events leading to residual ^{47}Sc nuclei with less than 10.6 MeV of excitation energy (binding energy of the neutron) were accepted as contributing to the cross sections.

[b] Only inelastic events leading to residual ^{73}Ga nuclei with less than 9.2 MeV of excitation energy (binding energy of the neutron) were accepted as contributing to the cross sections.

formation and interaction in the cascade stage of high energy nuclear reactions, and specifically in the mechanism of simple knockout reactions. The formation and escape of isobars could be an especially significant contribution to $(\pi,\pi N)$ reactions.

4.2.6. Discrepancy Between Computed and Experimental Cross Sections

For the present study, the Monte Carlo HEVI-DFF cross sections are generally a factor of two higher than the experimental (p,2p) cross sections for ^{48}Ti and ^{74}Ge. In addition, the HEVI-DFF code predicts only a 6% systematic increase in (p,2p) for ^{48}Ti over ^{74}Ge, compared to an experimentally observed 27-30% increase in the same direction.

This discrepancy, although large, should be viewed as a common difficulty among Monte Carlo cascade-evaporation codes in reproducing cross sections for the simplest nuclear reactions of the form (a,aN). Previously, the VEGAS-DFF code(53) has achieved good agreement with (p,pn) cross sections below the pion production threshold. From Fig. 4-1, it is noted that moderately close agreement between computed and experimental (p,2p) cross sections at 0.3 GeV is found, but that the discrepancy increases above this energy.

Generally, the reason for the differences between the Monte Carlo calculations and experimental results is unclear(57). It is suggested here, that perhaps inelastic collisions are contributing too heavily to the total (p,2p) cross sections, as was implied in the preceding paragraph. Future Monte Carlo calculations incorporating further refinements or input parameters may shed some light on the reasons for such discrepancies.

5. SUMMARY AND CONCLUSIONS - Part I

Cross sections for (p,2p) reactions above 0.3 GeV incident proton energy for ^{48}Ti and ^{74}Ge were measured by activation and calculated using a Monte Carlo intranuclear cascade-evaporation model (HEVI-DFF). The combined results lead to the following observations and conclusions:

(1). Both experimental and Monte Carlo computed $^{48}Ti(p,2p)\ ^{47}Sc$ and $^{74}Ge(p,2p)\ ^{73}Ga$ excitation functions display rising cross sections from 0.3 to 1 GeV incident proton energy. These results indicate that "quasi-free" pp collisions, a large fraction of which are inelastic, contribute to the studied reactions.

(2). Attenuation scattering of the incoming projectile and outgoing particles, including pions, by the nucleus accounts for the flattening of both experimental and calculated (p,2p) excitation functions relative to the free pp scattering cross sections.

(3). The rise in $\sigma(p,2p)$ over the energy region 0.4 GeV to 1 GeV for the reactions studied was (17±3)% and was roughly in agreement with previously observed (p,2p) cross section rises in the same energy region for a wide range of target mass numbers. This may imply the approximate cancellation of cross section reduction due to increasing attenuation of incoming projectile and outgoing particles, and cross section increase due to an increasing nuclear surface area, where simple reactions such as (p,2p) most frequently occur.

(4). Of several proposed explanations, the inordinately thick neutron skin of ^{74}Ge as compared to a more "normal" neutron skin thickness for ^{48}Ti is the most plausible argument for the 27-30% higher (p,2p) cross sections for ^{48}Ti than ^{74}Ge. The magnitude of the difference, however, is not predicted.

(5). Although the Monte Carlo calculations generate the correct energy dependence for the (p,2p) excitation functions, they predict a much larger (p,2p) cross section rise above 0.3 GeV incident proton energy than observed experimentally. Generally, calculated cross section magnitudes are a factor of two higher than experiment. Excessive contribution to the (p,2p) cross section from inelastic events is cited as a possible cause for this discrepancy.

(6). According to the HEVI cascade calculation, isobar formation and escape constitutes as much as 20% to the total (p,2p) cross section. Qualitatively, this demonstrates the importance of isobars in the mechanism of simple knockout reactions.

II

"Science is nothing but good sense and sound reasoning"

Stanislaus Leszcynski
King of Poland, 1763

Part II. Cross Sections for $(\pi^{\pm},\pi N)$ and Other More Complex Spallation Reactions on ^{14}N, ^{16}O and ^{19}F Through the (3,3) Resonance

1. INTRODUCTION

1.1 General Considerations of Free-Particle Pion-Nucleon Cross Sections

The use of π mesons in nuclear reaction studies is a potentially valuable tool in elucidating the mechanism of nuclear reactions at high energies. Naively, high energy (>100 MeV) pion-induced nuclear reactions are anticipated to proceed according to the impulse approximation, discussed in Part I of this thesis, and to show similarities to the interactions of high energy protons with nuclei. In contrast, however, to the nucleon-nucleon total cross sections, total pion-nucleon cross sections display several resonances(58). This picture is illustrated in Fig. 1-1, which is a plot of the total free-particle π^-p and π^+p cross sections as a function of incident pion kinetic energy. Each set of cross sections (hereafter denoted as $\sigma(\pi^-p)$ and $\sigma(\pi^+p)$) exhibits the well-studied $T = 3/2$, $J = 3/2$ resonance (commonly referred to as the (3,3) resonance) at about 180 MeV. Smaller resonances are observed for $\sigma(\pi^-p)$ at 600 and 900 MeV.

Therefore, the structures and magnitudes of the free-particle πN cross sections may manifest themselves in two important ways in a study of simple pion-induced nuclear reactions:

(i) The excitation functions for "knockout" reactions of the form $(\pi,\pi N)$, where N is the removed nucleon, should exhibit the resonant structures if a pion-nucleon initial collision has occured. (ii) The ratio of π^- to π^+ cross sections leading to the same product in knockout

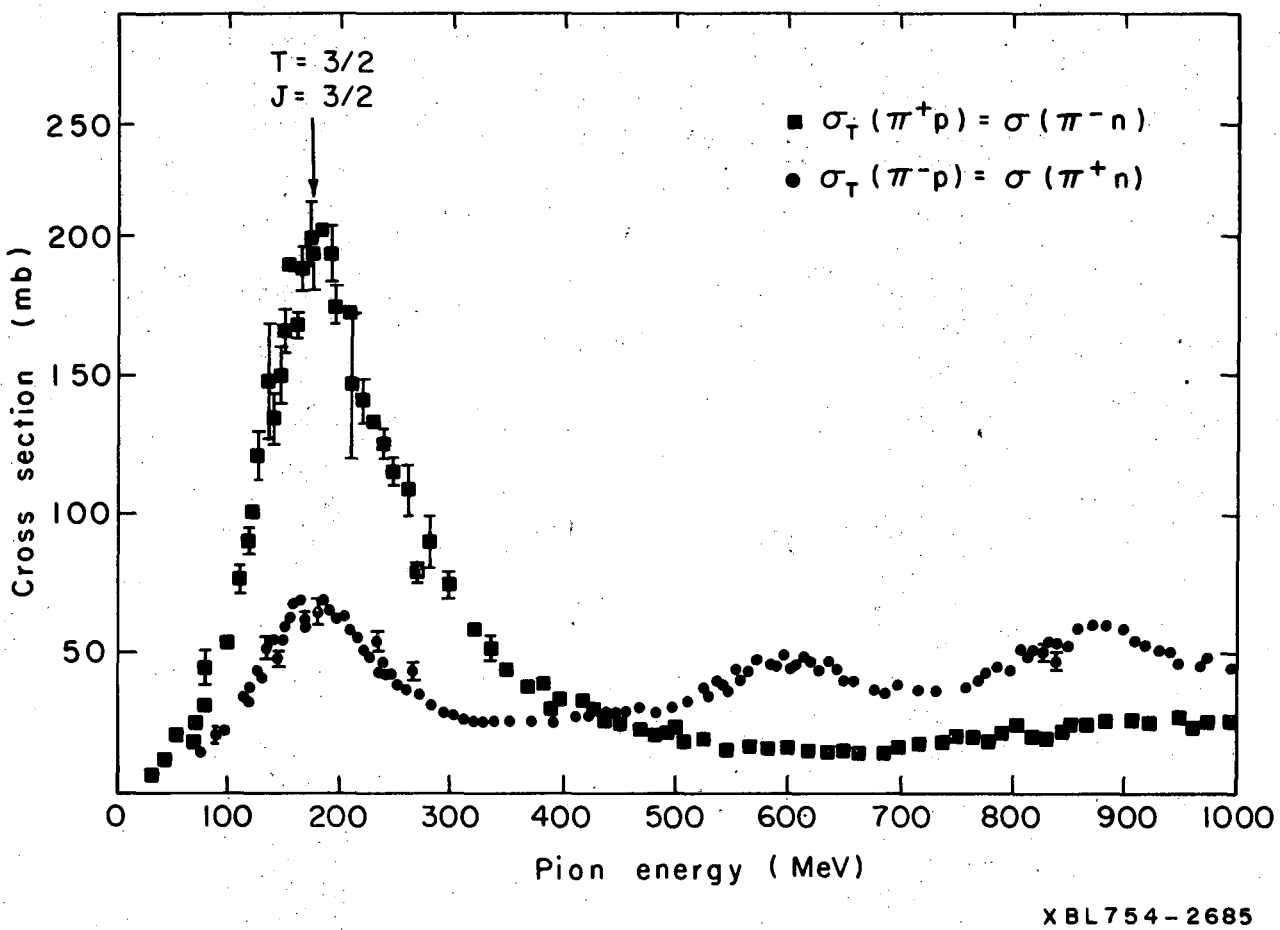

Fig. 1-1. The total free-particle $\pi^{\pm}p$ cross sections.

reactions at the same incident pion energy should also relate to the free-particle pion nucleon cross sections. For example, the measured ratio of cross sections $R_{\pi^-/\pi^+} = \sigma(\pi^-,\pi^-n)/\sigma(\pi^+,\pi N)$ (the notation $(\pi^+,\pi N)$ is compact for the $(\pi^+,\pi^+n + \pi^0p)$ reaction) for a target nucleus with N (the number of neutrons) equal to or very nearly equal to Z (the number of protons) would be expected to be approximately equal to the ratio of corresponding free-particle cross sections at a given energy. Thus

$$R_{\pi^-/\pi^+} = \sigma(\pi^-,\pi^-n)/\sigma(\pi^+,\pi N)$$
$$= \sigma(\pi^-n)/\sigma(\pi^+n) = \sigma(\pi^+p)/\sigma(\pi^-p) \qquad (1\text{-}1)$$

according to a simple impulse approximation treatment and applying the principle of charge symmetry to pion-nucleon systems.(59)

The most famous and interesting case is near the (3,3) resonance where the reactions

1)	$\pi^+ + p \rightarrow \pi^+ + p$	Elastic scattering	
2)	$\pi^- + p \rightarrow \pi^- + p$	Elastic scattering	(1-2)
3)	$\pi^- + p \rightarrow \pi^0 + n$	Charge exchange	

have cross sections in the ratio 9:1:2. These relative values come from appropriate combinations of Clebsch-Gordan coefficients in pion-nucleon eigenfunctions, and are derived in Appendix B. (60) Since $\sigma(\pi^+p) = \sigma(\pi^-n)$ and $\sigma(\pi^-p) = \sigma(\pi^+n)$ by charge symmetry (small Coulomb effects are ignored), one has that

$$\sigma(\pi^+p)/\sigma(\pi^-p) = \sigma(\pi^-n)/\sigma(\pi^+n) = 9/(1+2) = 3 \qquad (1\text{-}3)$$

This ratio would be expected to be approximately 3 from 100 to 250 MeV, above which point inelastic pion-nucleon collisions become important. Below 100 MeV, the longer mean free path and DeBroglie wavelength of the incident pion tends to make the impulse ratios less valid. In comparison, the ratio of corresponding experimental pion-nucleon cross sections is 2.9 at 180 MeV.(58)

1.2 Review of Prior Experimental and Theoretical $(\pi,\pi N)$ Studies

The PIONeering work of Reeder and Markowitz was the first to illustrate a broad peak at 180 MeV in the excitation function for the $^{12}C(\pi^-,\pi^-n)^{11}C$ reaction (61). This observation was not only ascribed to the dominance of the (3,3) free-particle πN resonance, but was also interpreted in terms of a CKO mechanism (see Section 1.2 of Part I of this thesis).

This original study initiated considerable interest in the area of pion reactions related to free-particle πN collisions in the nucleus. Excitation functions for (π^-,π^-n) reactions on ^{12}C and ^{19}F were measured above 450 MeV and compared with simple calculations based on π^-n cross sections and approximations to attenuation factors for scattering of the incident pion projectile in the nucleus. (62-64) An interesting study of the $^{40}Ar(\pi^-,\pi^-p)\ ^{39}Cl$ reaction showed preservation of the π^-p resonances in its excitation function at 600 and 900 MeV (65). Excitation functions determined in the vicinity of the (3,3) resonance for the $^{19}F(\pi^-,\pi^-n)\ ^{18}F$(66) and $^{19}F(\pi^+,\pi N)\ ^{18}F$(67) reactions displayed very narrow peaks near 180 MeV. Cross sections measured in several of the above mentioned studies for the more complex spallation reactions $^{27}Al(\pi^-,X)\ ^{11}C$, ^{18}F(62) and $^{40}Ar(\pi^-,\pi^-2p)\ ^{38}S$(65) above 450 MeV failed to exhibit any structure in

their excitation functions that could be correlated to the π^-p resonances at 600 and 900 MeV.

Theoretical treatments followed to explain the observed shape of $(\pi,\pi N)$ excitation functions. Kolybasov(68) achieved fair agreement with the shape of the $^{12}C(\pi^-,\pi^-n)\ ^{11}C$ excitation function by employing a plane wave impulse approximation apprach, later modified by Dalkarov(69) to get even better agreement with the shape. Selleri(70) attained excellent agreement with the ^{12}C data by incorporating kinetmatical corrections. The Monte Carlo LEVI-DFF calculations of Harp and co-workers(54), based on possible formation and interaction of isobars, were also in good agreement with the shape and magnitude of the $^{12}C(\pi^-,\pi^-n)\ ^{11}C$ excitation function. The Monte-Carlo intranuclear cascade-evaporation computations of Bertini(52), based on effects due to absorption and a diffuse nuclear surface, reproduced the peaks in the $^{40}Ar(\pi^-,\pi^-p)\ ^{39}Cl$ excitation function at 600 and 900 MeV and also demonstrated, as the experiment showed, lack of structure in the $^{40}Ar(\pi^-,\pi^-2p)\ ^{38}S$ reaction at the same energies.

The first extensive preliminary investigation using both positively and negatively charged pions was performed by Chivers et al.(71) This study measured activation cross sections and excitation functions for several nucleon knockout (including $^{12}C(\pi^{\pm},\pi N)\ ^{11}C$) and charge-exchange reactions on light nuclei, and discovered the surprising result that the π^-/π^+ cross section ratio for $(\pi,\pi n)$ reactions on ^{12}C, ^{14}N, and ^{16}O was 1.0 ± 0.1 at 180 MeV. As pointed out in the paper at that time, this ratio was in conflict with the simple impulse value of 3 at 180 MeV. Other determinations of pion-nucleon knockout ratios at various pion energies for ^{4}He thru ^{64}Zn(71-81) have also been in disagreement with the impulse

approximation prediction. These measured and predicted ratios are summarized in Table 1.1.

These discrepancies of the Chivers data with the impulse approximation continued to be a puzzle with regard to the exact reaction pathway or mechanism of these simple (π,πN) reactions. Several theories, none of which were entirely convincing in resolving the discrepancy, were applied to explain the results. These proposals included the ideas of "quasi-alphaparticles"(82), excitation of intermediate isospin states (71,83), Fermi averaging(84,85), compound nucleus effects(86), formation of nucleon isobars, and nucleon charge exchange (87). Until recently, the nucleon charge exchange model developed by Hewson(87) and the final state interaction theory of Robson(86) have appeared to be the most viable of the numerous considerations.

A redetermination(88) of the $^{12}C(\pi^{\pm},\pi N)\ ^{11}C$ excitation functions through the (3,3) resonance for the purposes of monitoring pion beams at high intensities has shown a cross section ratio at 180 MeV for $\pi^-/\pi^+ = 1.55\pm0.10$, in serious disagreement with the ratio of 1.0±0.1 by Chivers et al.,(71) and still in discrepancy with the impulse model value of 3. However, the ratio of these newly measured cross sections as a function of incident pion energy has recently been interpreted successfully in terms of a semi-classical nucleon charge exchange model by Sternheim and Silbar.(89)

1.3 Definition and Purpose of Project-Part II

The overall scope of this thesis, which was defined in Part I, is continued with the following experiments. In light of the introductory remarks and review of past work, the specific purpose of the project was

Table 1-1. Comparison of measured pion knockout cross section ratios with impulse approximation predictions

Energy (MeV)	Target	Isospin	Cross Section Ratio	Measured Ratio	Impulse Approximation[a]	Reference
30	^{12}C	0		0.41±0.06	—	73
50	^{12}C	0		0.50±0.12	1.3	73
70	^{12}C	0		0.80±0.10	1.8	73
90	^{12}C	0		0.80±0.10	2.5	73
180	^{12}C	0		0.97±0.09	3	71
180	^{12}C	0	$\frac{\sigma(\pi^-,\pi^-n)}{\sigma(\pi^+,\pi N)}$	1.4 ±0.1 [b]	3	75
70	^{14}N	0		0.52±0.11	1.8	76
90	^{14}N	0		0.75±0.13	2.5	76
180	^{14}C	0		0.95±0.09	3	71
180	^{16}O	0		1.02±0.09	3	71
184	^{19}F	1/2		1.11±0.14	~ 3	80
190	^{19}F	1/2		1.52±0.05[c]	~ 3	79
184	^{31}P	1/2		1.61±0.31	~ 3	80
184	^{64}Zn	2		2.94±1.12	~ 3	80
180	^{9}Be	1/2	$\frac{\sigma(\pi^+,\pi^+p)}{\sigma(\pi^-\pi^-N)}$	2.1 ±0.6	~ 3	71
153	^{4}He	0	$\frac{\sigma(\pi^-\pi^-n)}{\sigma(\pi^-\pi^-p)}$	4.7 ±1.1	8.7	72
250	^{12}C	0	$\frac{\sigma(\pi^-,\pi^-n\gamma)}{\sigma(\pi^-\pi\ N\gamma)}$	1.3 ±0.4	2.7	74
215	^{16}O	0	$\frac{\sigma(\pi^-,{}^{15}N[6.32(3/2)^-])}{\sigma(\pi^-,{}^{15}O[6.18(3/2)^-])}$	1.8 ±0.4	3	77

(continued)

Table 1-1. (continued)

Energy (MeV)	Target	Isospin	Cross Section Ratio	Measured Ratio	Impulse Approximation[a]	Reference
180	^{16}O	0	$\frac{\sigma(\pi^+, {}^{15}O\ 6.18(3/2)^-)}{\sigma(\pi^+, {}^{15}O\ 6.32(3/2^-))}$	1.7±0.4	3	78
70	^{27}Al	1/2	$\frac{\sigma(\pi^+, \pi^+ p)}{\sigma(\pi^-, \pi\ N)}$	0.52±0.16	~ 1.8	81
70	^{28}Si	0		0.28±0.13	~ 1.8	81

[a]Free-particle pion-nucleon experimental cross sections were taken from reference 58. It is noted here that these impulse ratios may not strictly apply at energies less than 100 MeV, due to potentially increasing contributions to the reaction mechanism from the ISE process.

[b]Measured ratio is based on a redetermined $(\pi^+,\pi N)$ cross section of 50 ± 4 mb.

[c]Based on the $^{12}C(\pi^{\pm},\pi N)\ ^{11}C$ cross sections in reference 85.

multifold.(1). To firmly establish the appearance of the (3,3) resonance in the excitation functions for $(\pi,\pi N)$ reactions on the light nuclei ^{14}N, ^{16}O, and ^{19}F (2). To provide a set of π^-/π^+ cross section ratios for $(\pi,\pi N)$ reactions on the light nuclei ^{14}N, ^{16}O, and ^{19}F as a function of pion energy for potential insight into the reaction mechanism puzzle. (3). To recheck the activation results of Chivers et al.$(\pi^+,\pi N)$ reactions on ^{14}N and ^{16}O, using the intense pions beams at the Clinton P. Anderson Meson Physics Facility in Los Alamos, New Mexico (LAMPF).

The light nuclei ^{14}N, ^{16}O, and ^{19}F are good choices as targets for this reaction study because their constituent nucleons are essentially all on the "surface", where knockout reactions are thought to occur. There exist some small differences in nucleus structure among these nuclei: ^{14}N and ^{16}O both have N = Z (T = 0) while ^{19}F has N = Z + 1 (T = 1/2); ^{14}N is also "odd-odd" and has spin angular momentum of 1.

2. EXPERIMENTAL PROCEDURE

The experimental procedure used to study pion reactions on the light nuclei mentioned involved activation of thick (0.3-2.5 g/cm^2) target discs in the secondary pion beams at the Lawrence Berkeley Laboratory 184-inch synchrocyclotron and the Clinton P. Anderson Meson Physics Facility in Los Alamos, New Mexico (also referred to as LAMPF-Los Alamos Meson Physics Facility). Generally, pion fluxes attained at LAMPF were 5-10 times greater that those obtained at Berkeley. Postirradiation assay of target and monitor discs was achieved by coincidence detection of the two 511 keV gamma rays from positron (β^+) annihilation. Decay curves obtained in this manner generally consisted of from one to three components. The unfolding of separate radionuclides from these decay curves provided their yields.

The reactions $^{12}C(\pi^{\pm},\pi N)^{11}C$ for which cross sections have been accurately determined, were used to monitor the pion fluxes.(90) The details of the experimental procedure employed are given in the following sections.

2.1 Targets

The relatively low secondary pion-beam fluxes if 10^5-10^6/sec (compared to an average synchrocyclotron current of $1\mu A=6\times10^{12}$protons/sec) encountered in this work required the use of thick targets for activation studies. For well focused pion beams with fluxes exceeding 10^6sec, target discs having thinner and smaller diameters than those run at lower fluxes could be exposed.

Targets for ^{12}C, ^{14}N, and ^{19}F took the form of machined discs of plastic scintillator or polyethylene, boron nitride, and polytetrafluoroethylene (commerically known as "Teflon"), respectively. The dimensions of these discs varied from 4 to 6 cm in diameter by 0.3 to 1.3 cm thick. The target for ^{16}O consisted of powdered boric acid packed tightly in a 0.013 cm thick aluminum can with dimensions 5 cm, in diameter by 1.3 cm thick. A summary of the targets and their respective chemical compositions is given in Table 2-1.

2.2 Bombardments

Although the targets used in this pion study were generally much thicker than the evaporated thin targets used in the proton bombardments, a similar stacked arrangement was used. This picture is illustrated in Fig. 2-1. For each run, the combined target consisted of two discs of equal diameter and thickness, one being a disc of plastic scintillator or polyethylene and the other being a disc of either boron nitride, Teflon, or a can of boric acid. The plastic disc was always the first target to receive the beam and acted as a beam flux monitor by the reaction

Table 2-1. A summary of pion targets

Target Nucleus		Empirical Formula	Diameter (c.m.)	Thickness (c.m.)	Surface Density (g/cm^2)	Chemical Composition
^{12}C (monitor)	"Pilot B" [a] Plastic Scintillator (Polyvinyltoluene)	$CH_{1.1}$	3.8-5.0	0.3-1.3	0.3-1.3	91.4% C 8.5% H 0.2% impurities
	Polyethylene	$(CH_2)_n$	5.0-6.3	0.6-1.3	0.6-1.2	85.4% N 14.4% H 0.2% impurities
^{14}N	Boron Nitride	BN	3.8-5.0	0.3-1.3	0.6-2.6	95.5% BN [b] 1.5-2.5% O 1% B_2O_3
^{16}O	Boric Acid (in 0.013 cm Al can)	H_3BO_3	5.0	1.3	1.1-1.4	77.6% O 17.4% B 0.1% sulfates metals, phosphates metals, phosphates
^{19}F	"Teflon" (Polytetrafluoroethylene)	$(CF_2)_n$	3.8-5.0	0.3-1.3	0.6-2.6	75.8% F 24.0% C 0.2% impurities

[a] Obtained from Pilot Chemicals Division, New England Nuclear Corporation, Watertown, Massachusetts

[b] D. Malone, private communication.

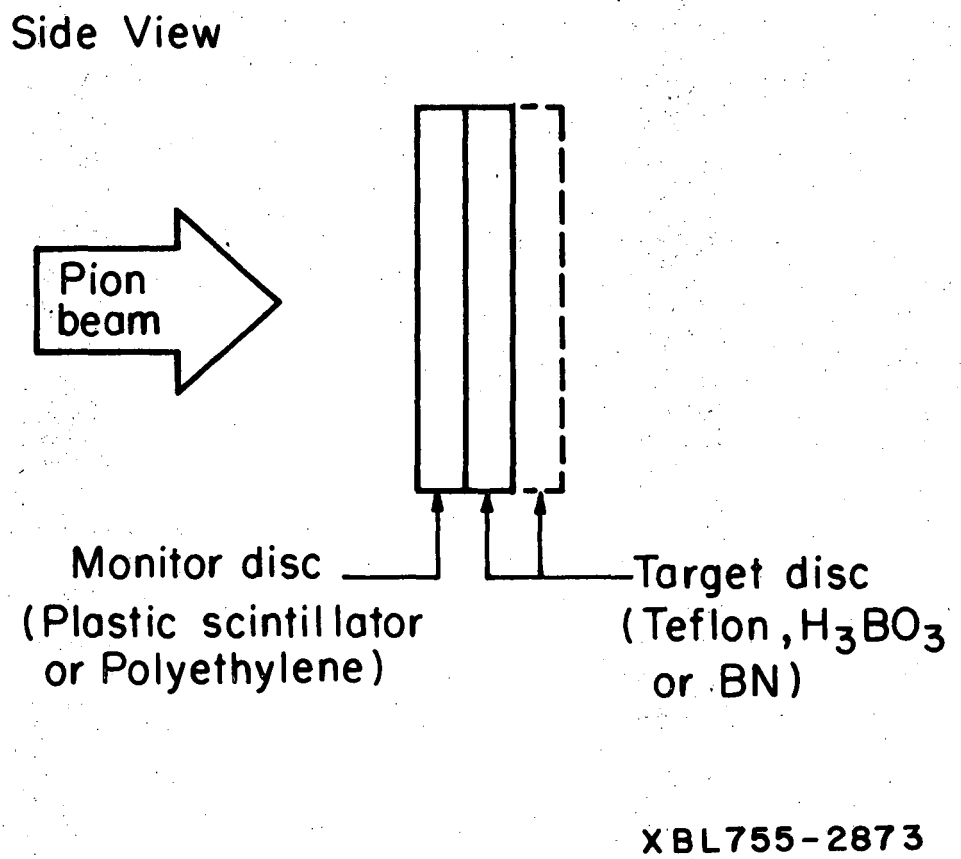

Fig. 2-1. The target stack.

$^{12}C(\pi^{\pm},\pi N)\ ^{11}C$, for which cross sections from 50-550 MeV incident pion energy are known.(88). These target discs were aligned in a stack and taped together. For the first few experiments, a third primary target disc was added to the stack in order to maximize the efficiency of the exposure time. This policy was not employed later because of the potential problem of increasing seconary particle transmutation effects from overly thick targets. Exposure times were from 10-20 minutes for boron nitride targets, 10-40 minutes for Teflon targets, and 2-4 minutes for a boric acid target. Weighing of the targets between experiments showed only negligible changes in masses.

The importance of making the targets the same shape and dimension is twofold. Equal face areas will insure that the beam intercepts both equally. In addition, for each disc, the efficiency for coincidence detection of the two positron annihilation quanta would be equal, with the exception of small self-absorption differences. This last point will be discussed further later in the text.

In order to check the contribution of stray neutron background in the experimental meson caves to the production of the desired nuclei, thick "dummy" targets were periodically exposed out of the pion beam, simultaneously with the real targets. The dummy targets, which were identical to the actual targets, showed negligible activity relative to the pion activated targets. Thus, the stray neutron effect was ignored.

2.3 Secondary Pion Beams

The study of pion-induced nuclear reactions was initiated at the Lawrence Berkeley Laboratory 184-inch synchrocyclotron, where secondary

pion fluxes of generally 10^5/sec could be obtained in the Meson and Physics Cave. The advent of the Clinton P. Anderson Meson Physics Facility (LAMPF) at the Los Alamos Scientific Laboratory made it possible to complet the project in the Land of Enchantment. During this period, the main proton beam at LAMPF was run at an energy of 800 MeV at an average intensity of 5-10 μA. The fluxes obtained in the Low Energy Pion (LEP) and the Pion and Particle Physics (P^3) channels averaged 5×10^5 pions/sec and toward the last running cycle of the machine, approached 10^7 pions/sec. Final design specifications of the LAMPF accelerator would allow an average main proton beam current of 1 milliampere. Average fluxes of 10^9-10^{10} π/second could be achieved under these conditions.

2.3.1 The 184-Inch Synchrocyclotron

The main proton beam of the LBL synchrocyclotron was used to produce secondary pion beams in two different experimental areas. Brief descriptions of these beams are given in the following sections.

2.3.1 A The Meson Cave (LBL)

The method for obtaining typical external pion beams in the Meson Cave is illustrated in Fig. 2-2. An internal proton beam of approximately 1 μA current at the maximum energy of 730 MeV is allowed to strike an internal beryllium or polyethylene target. The charged pions produced from the inelastic nucleon-nucleon collisions are then bent out of the vacuum tank by the fringing magnetic field of the synchrocyclotron through a thin aluminum window. A quadrupole magnet just outside the window focuses the beam before it proceeds into the cave. After passing through an iron wheel, the pions, having many different energies, are filtered for a

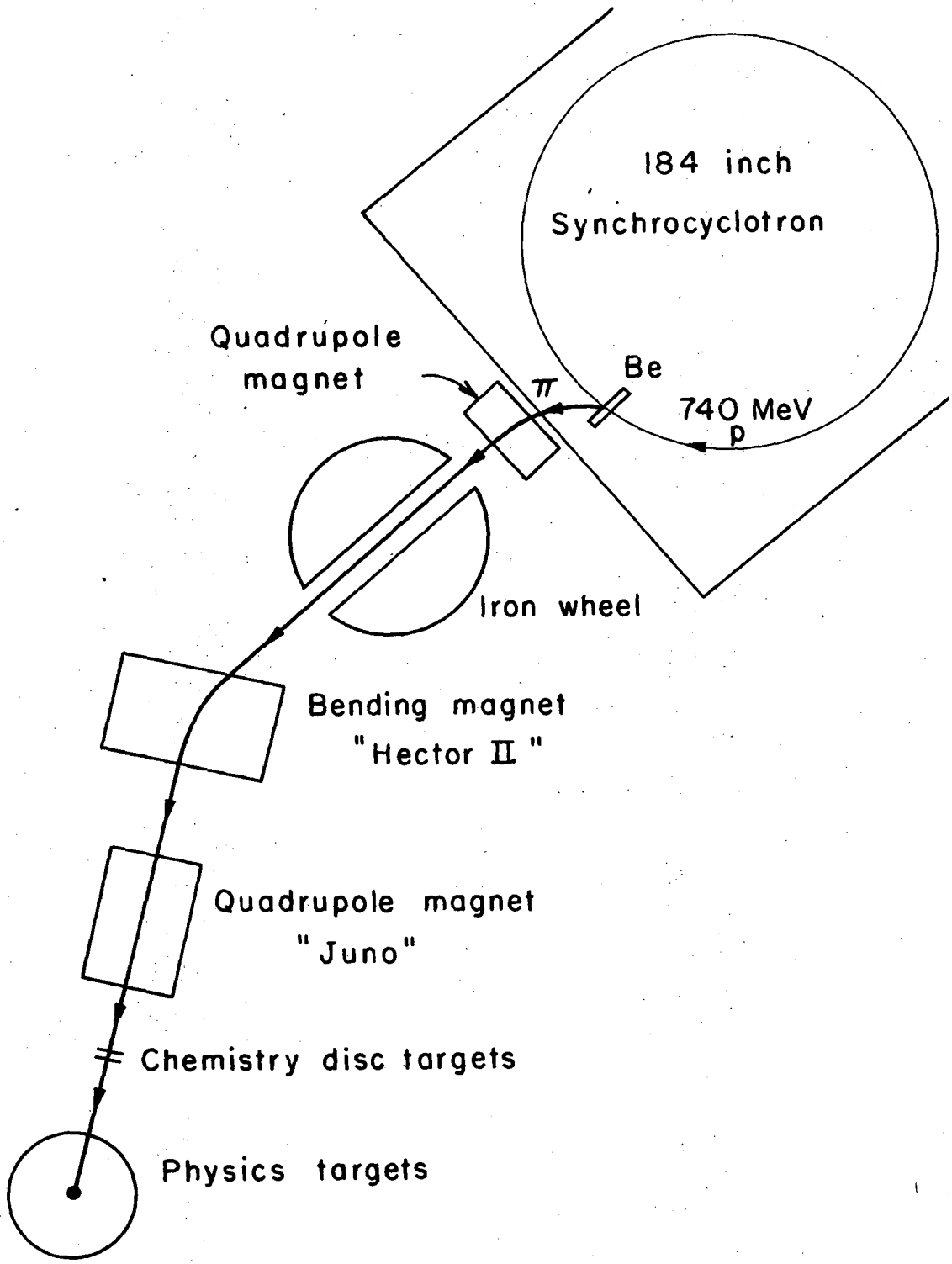

Fig. 2-2. The Meson cave at Berkeley.

specific momentum by a bending magnet ("Hector II") and then focused again by another quadrupole magnet ("Juno") before striking a target. The chemistry disc targets were exposed in a parasitic fashion just upstream of the physics targets. Pion fluxes in the Meson Cave averaged 10^6/second over an area of about 100 cm^2 at 1μA of main proton beam. The effective flux at the disc targets was approximately 2×10^5 /sec.

The pion energies were determined accurately from range energy curves taken by the physics group using the beam. The energy of the π^- beam, determined in this manner, was found to be 100±10 MeV.(91) This was the only beam available in the Meson Cave during the course of these experiments. Several 45 MeV beams were obtained by degrading the energy of the original pion beam with several inches of polyethylene.

Calculations of the beam contamination by leptons was also performed by the physics group(91) and indicated that about 20% of the beam striking the target position contained u^- and e^- resulting from the decays

$$\pi^- \rightarrow u^- + \nu \qquad \tau = 2.5\times10^{-8} \text{ sec.}$$

$$u^- \rightarrow e^- + \nu + \bar{\nu} \qquad \tau = 2.2\times10^{-6} \text{ sec.}$$

These decay muons and electrons have the same momentum as the pions and hence, cannot be discriminated aginst by the bending magnet. It may be assumed that these weakly interacting leptons contribute only negligibly, compared to the strongly interacting pions, to the desired nuclear reactions.(60)

For several irradiations, the exposure of thick "dummy" targets out of the pion beams simultaneously with the real targets revealed a

negligible contribution by stray neutrons in the cave to the nuclear reactions under study.

2.3.1 B The Physics Cave (LBL)

The setup for obtaining well defined pion beams in the Physics Cave is illustrated in Fig. 2-3. The pions are initially produced when an external proton beam from the synchrocyclotron collides with a polyethylene target. These pions are respectively focused by a quadrupole magnet ("Hera"), selected for a desired momentum by a bending magnet ("Ulysses") and focused again ("Hero"). A polyethylene block just after this quadrupole serves to eliminate the proton component of the beams containing positive pions. These protons in π^+ beams have the same momentum as the pions, but much lower kinetic energies due to their greater mass. The absorber, then, can completely eliminate the proton comtination of the beam with negligible effect on the pions. After passing through the absorber, the beam is bend ("Amphion"), and focused ("Belona") once more before striking a physics target. For exposures relevant to this work, it was possible to interrupt the long-running physics experiments to perform short, independent irradiations. These chemistry targets were always placed just upstream of the liquid hydrogen targets.

Pion beams from 160-340 MeV incident $\pi^{\pm}$ energy were used for the study of the pion reactions in this work. Typical fluxes averaged $10^6\pi^+$/sec and $10^5\pi^-$/sec, with a momentum resolution $\Delta p/p$ of ±2.6% at 300 MeV and ±4% near 160 MeV. Figures on the beam momentum resolution were determined by either range curve measurements, magnetic field sweeps, or a Monte Carlo computer reconstruction of $\pi^{\pm}p$ scattering.(92) The percentage of beam contaminants was (7±1)% u^+, and (0.5±0.5)% e^+ of beams

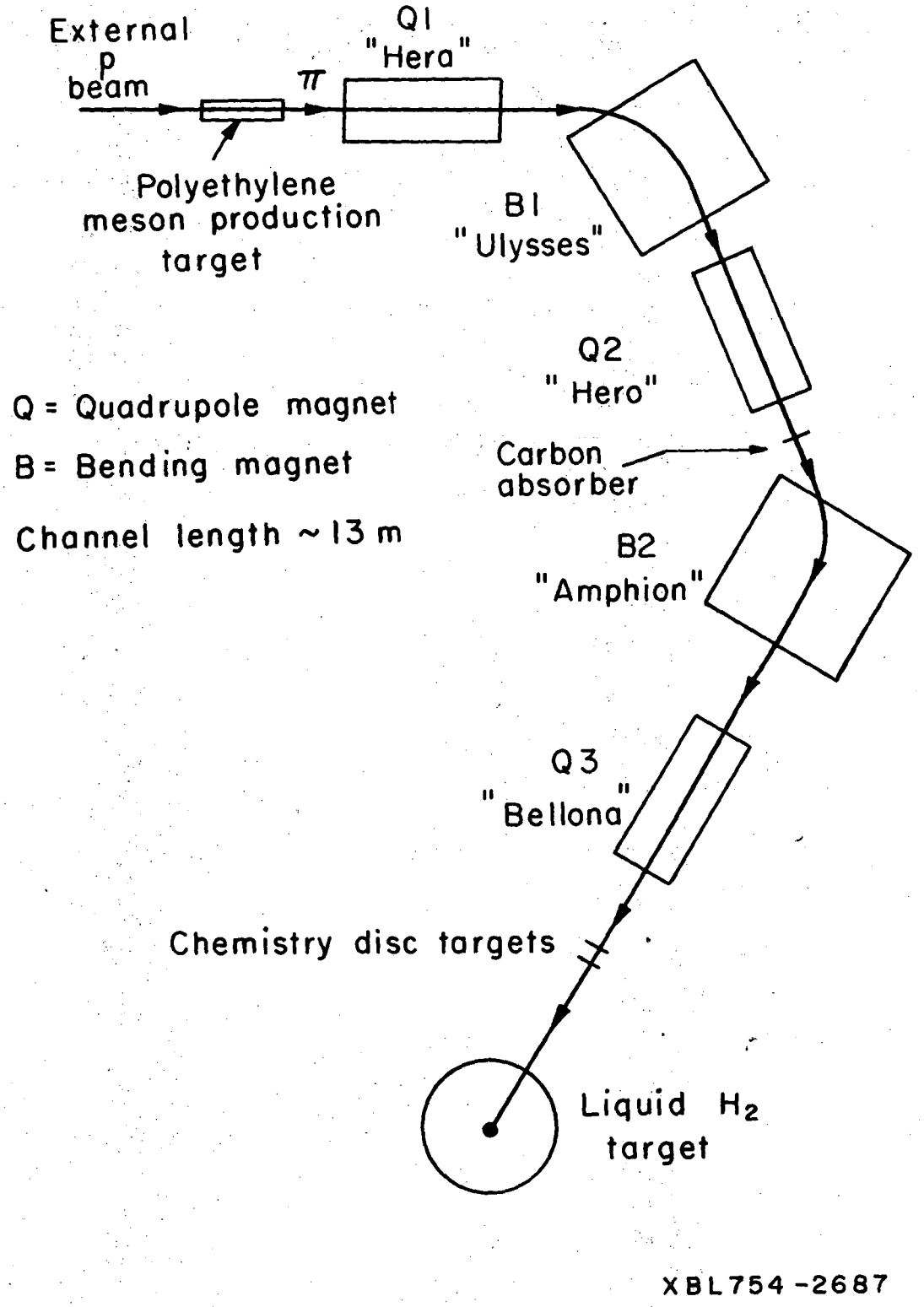

Fig. 2-3. The Physics cave at Berkeley.

containing π^-, between 260-300 MeV incident pion energy and remained very approximately equal at lower energies. These contamination figures were measured by Cerenkov counters or differential range curves in Cu and were obtained from the physics group resonsible for setup of the beam.(92)

Neutron counters used in the physics experiments yielded backgrounds of 2-5 neutrons/cm^2 sec in the Physics Cave. Exposure of thick dummy targets outside of the beams during a run showed no significant effect caused by his low neutron background.

2.3.2 The Clinton P. Anderson Meson Physics Facility (LAMPF)

This facility, operated by the Los Alamos Scientific Laboratory (LASL) was designed to deliver an average proton beam current of 1 milliampere at 800 MeV energy. The intent of LAMPF was to provide the scientific community with a tool for carrying out a broad spectrum of research in such fields as atomic and nuclear physics, radiochemistry, and biology. Important practical applications of this facility would encompass the areas of medicine and isotope production.

This pion work was completed at LAMPF during a period while average main proton beam intensities were 5-10 μA. These currents are low compared to the final design capabilities and were kept at these levels to be consistent with the amount of shielding stacked around the experimental areas. Pion fluxes at this time were an average of about 5×10^5-10^6/sec. The final design current of 1 mA would correspond to approximately 10^9 π/sec in the secondary channels.

The project at LAMPF was performed in conjunction with the remeasurement of the $^{12}C(\pi^{\pm},\pi N)\ ^{11}C$ excitation functions from 50-550 MeV incident pion energy by members of the nuclear chemistry divisions from

LASL, Argonne and Brookhaven National Laboratories.(88) The purpose of this companion experiment was to develop a suitable monitor reaction for use at high pion fluxes. The exposures relevant to this work were done by parasiting targets downstream from the targets of the Pion Monitoring Group, or by using the time between their irradiations to do an independent run.

Secondary beam channels were set up by this group for all pion runs. The quadrupole and bending magnet voltage settings for a desired pion energy were calculated by a computer code (TRANSPORT). After the tuning of the channel to these settings, further beam refinements could often be made. A magnetic field sweep of the last bending magnet in the channel, for example, could position the beam in a desired spot. The last quadrupole in the channel could be set to focus or defocus the beam as suited the needs of the experiment.

The pion monitoring experiment was initially limited to low beam intensities of 3×10^5 particles/sec in order to minimize the accidental counting rate through the 3 element counter telescope and to prevent the phototubes attached to the scintillation paddles from damage by excessive current. Toward the end of the scheduled shutdown when Al and heavier metals such as copper and molybdenum were exposed, the emittance and momentum slits in the channels were opened to give secondary pion fluxes approaching 10^7/sec. Consequently, it then became possible to irradiate thinner targets than previously at the lower pion fluxes. Throughout this work at LAMPF, post-exposure counting rates of the samples were an average of 5-10 times larger than they had been for comparable runs at the LBL synchrocyclotron.

A layout of the LAMPF facility is illustrated in Fig. 2-4. A 50 mA ion source and a 750 keV Cockcroft-Walton accelerator inject H^+ ions into a 100 MeV Alvarez drift-tube linac. The beam out of the Alvarez section is then injected into a wave-guide linear accelerator which increases the proton energy from 100 MeV to a maximum of 800 MeV. A separate ion source can inject H^- ions if desired. Thus, the LAMPF machine has the capability of accelerating H^+ and H^- ions simultaneously, with average currents of 1 mA and 100 μA, respectively.

The main proton beam passes into Area A, illustrated in Fig. 2-5. Pions are produced when the beam strikes the graphite or aluminum oxide rotating wheels, which are the meson targets labeled A-1 and A-2. The four main experimental channels using the mesons created from these targets are the Energetic Pion Channel and Spectrometer (EPICS), the Stopped Muon Channel (SMC), the Low Energy Pion Channel (LEP), and High Energy Pion Channel (P^3). Since the LEP and P^3 channels were used in this study, a brief description of these beam lines is given. Details concerning the accelerator and secondary beam lines are contained elsewhere(93).

2.3.2 A The High Energy Pion Channel (P^3)

The P^3 channel was used to obtain pions from 100 to 550 MeV for π^- and up to 450 MeV for π^+. Above the energy of 450 MeV, beams containing π^+ were intolerably contaminated by protons. This condition was not acceptable for pion activation experiments, since the proton induced reactions have cross sections comparable to the pion reactions of interest.

A schematic representation of the P^3 channel is shown in Fig. 2-6. The total length of this channel is about 20 m. The pions created at A-2 are transported through various quadrupoles for focusing, bending magnets

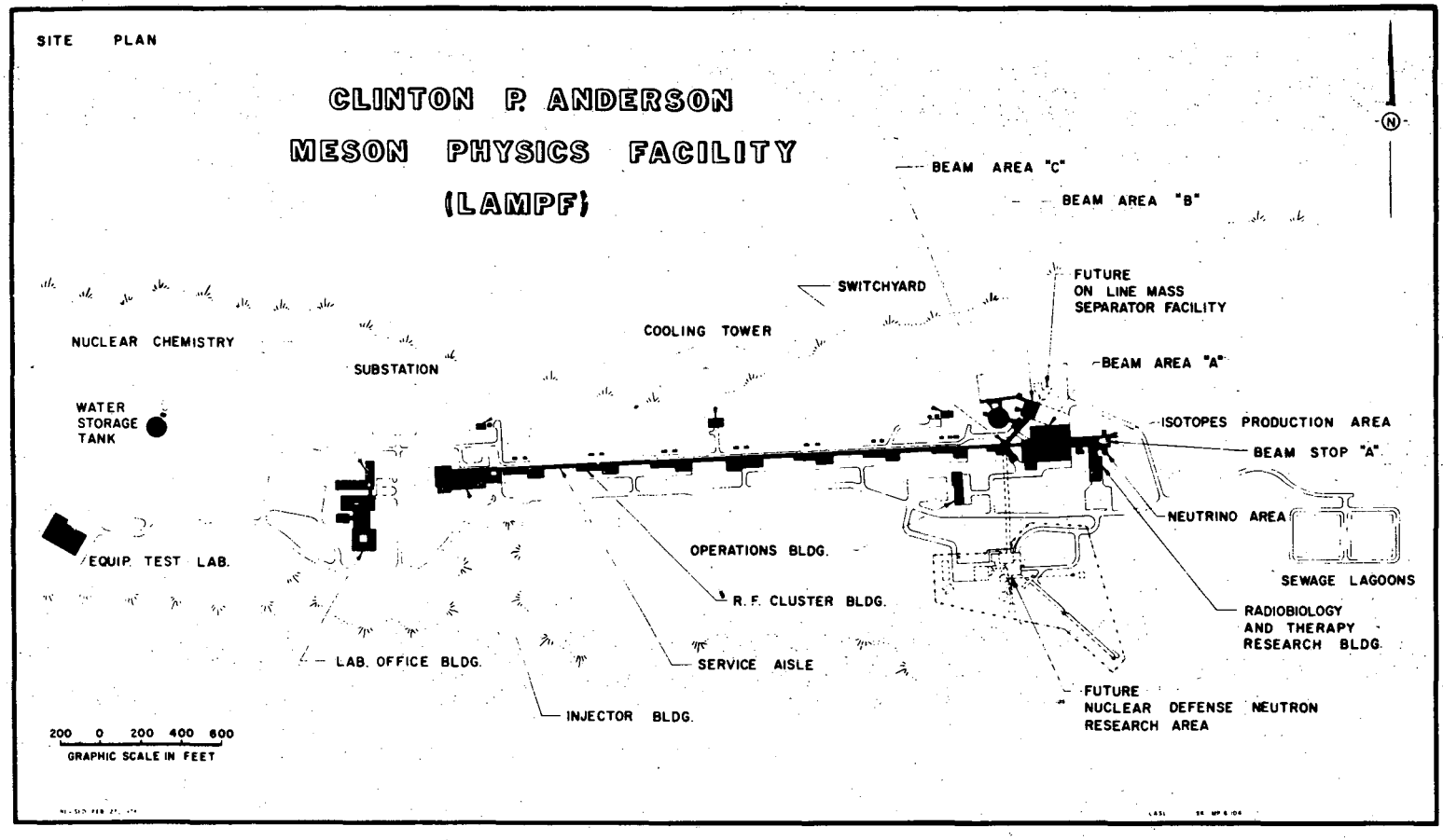

XBL 755-1344

Fig. 2-4. A layout of LAMPF.

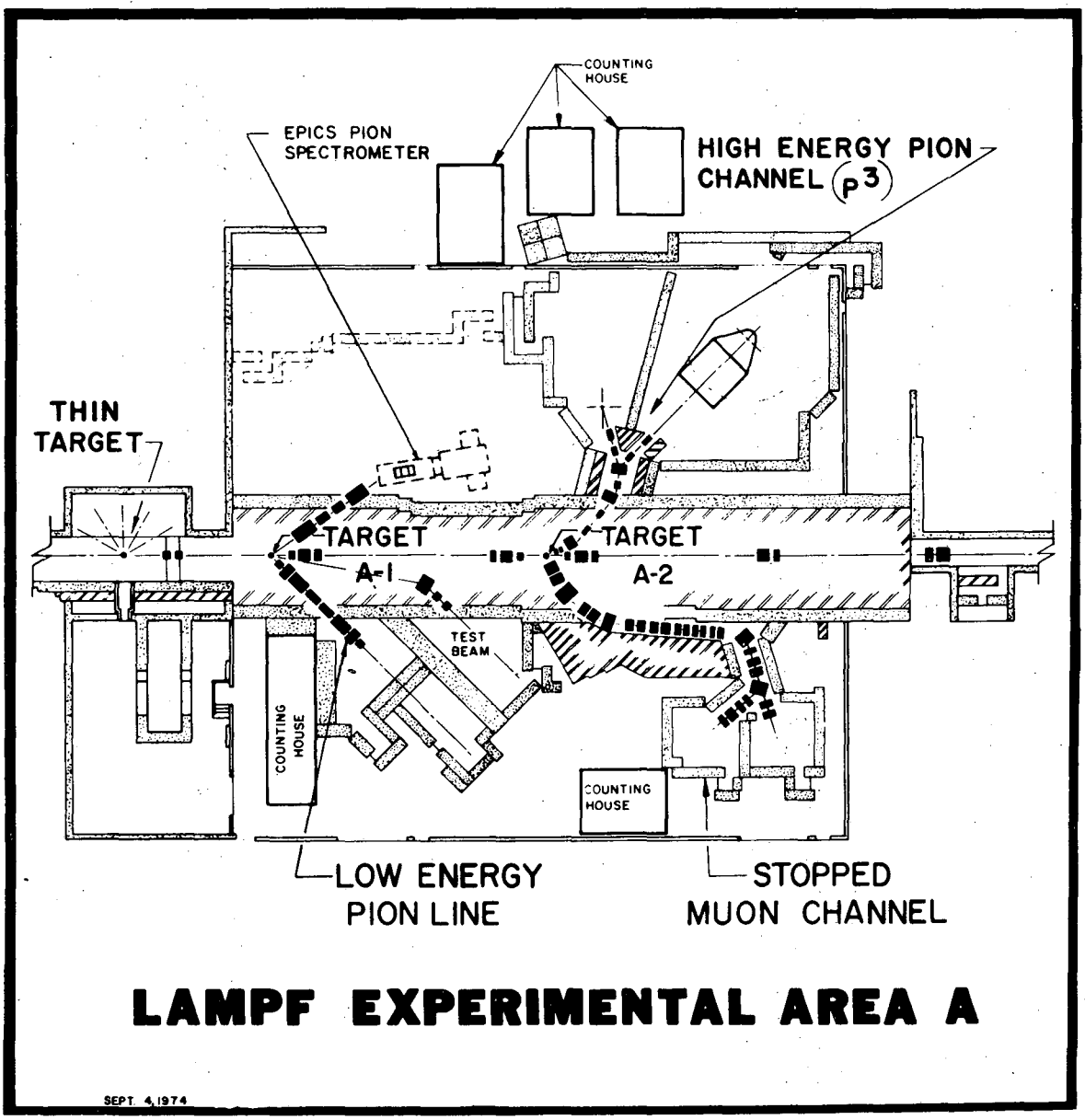

XBL 755-1343

Fig. 2-5. LAMPF experimental area A.

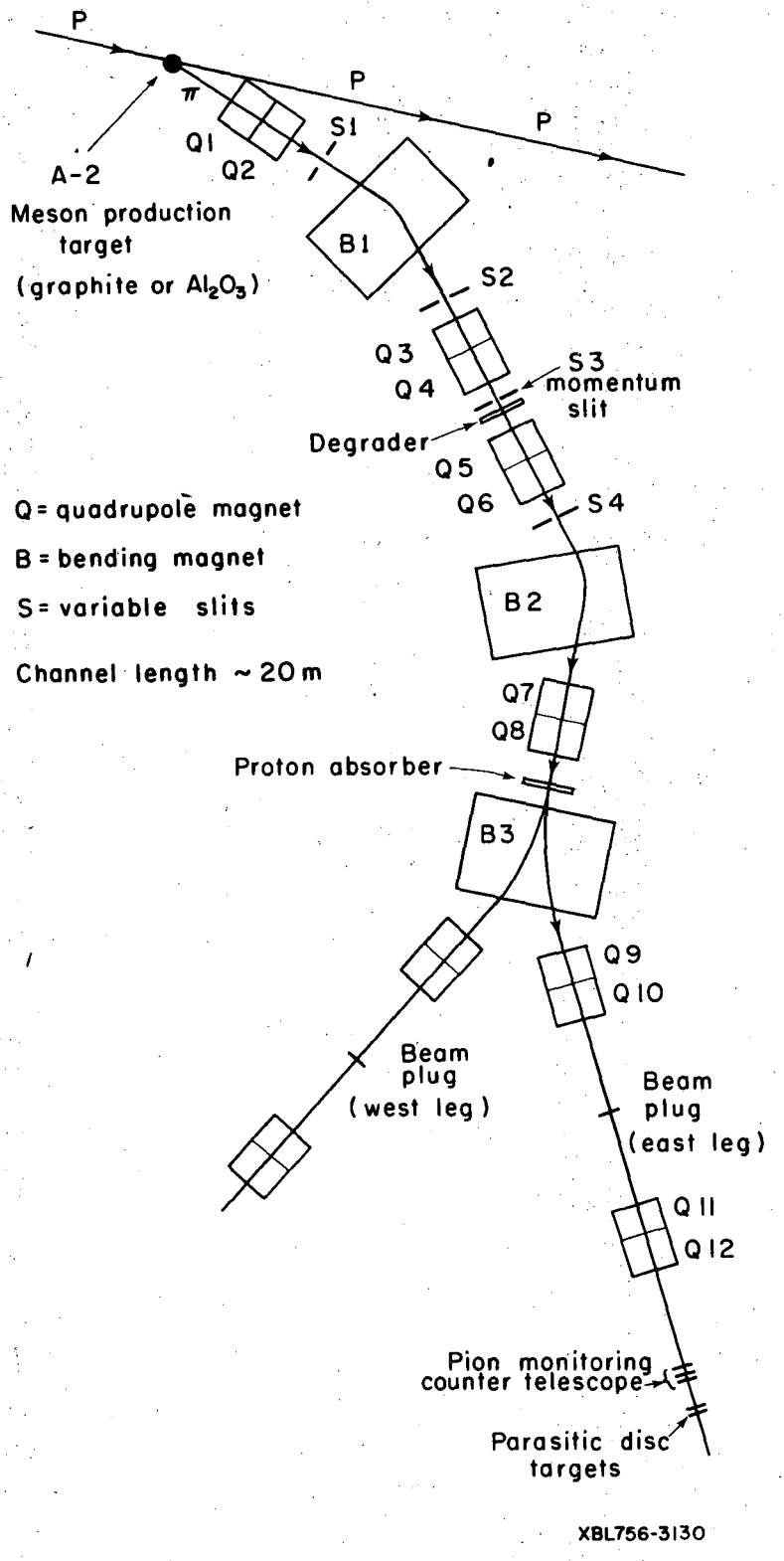

Fig. 2-6. The high energy pion channel (P^3) at LAMPF.

for momentum purification, and beam slits, for defining emittance and momentum. Located just down stream from the momentum slit S3 is a graphite degrader for removing protons from the π^+ beams. A proton absorber located after Q8 serves to remove low energy protons that pass through the degrader and still remain in the beam. The third bending magnet can steer the beam to either leg of the channel (east or west) and can be tuned to position the beam spot where desired. The last four quadrupoles in each beam leg can be adjusted to modify the beam phase space. The normal beam distribution emerging from the exit quadrupole was a well-focused spot with a 2.5 cm diameter. During the course of this work, both legs of the channel were used. For high energy π^+ experiments exceeding about 350 MeV, it was discovered that the West leg of the beam line yielded less proton contamination that the East leg. This phenomenon was thought to be due to the fact that the proton absorber shadowed the entire beam more thoroughly in the West than the East leg. Therefore, the West leg of the P^3 Channel was most useful for exposures requiring π^+ energies exceeding 350 MeV.

Magnet settings for obtaining pions of the desired energy were determined by the computer code TRANSPORT.(88) Momentum resolution of the beam was adjusted by S3, and was calculated according to the digital voltmeter readout on this slit. Throughout these experiments, momentum resolution for pion beams in this channel varied from $\Delta p/p$ = 2-10%. Contamination of the beam by muons and electron was measured by a time-of-flight technique. (88) These figures varied from 60% u^- and e^- for beams containing π^- and 30% u^+ and e^+ for beams containing π^+ at 100 MeV; and less than 10% muons and electrons for beams containing π^+ or π^-

at 350 MeV. Proton contamination in high energy pion beams exceeding 350 MeV was measured by a dE/dx technique.(88) With the proper thickness of degrader, this was kept to less than about 5% of the π^+ beam.

Periodic exposure of dummy targets revealed negligible contribution of fast neutron background to the measured cross sections.

2.3.2 B The Low Energy Pion Channel (LEP)

The LEP Channel was useful in obtaining low energy pion beams with a minimum amount of contamination from muons and electrons. This is due to its relatively shorter length of 14 meters, compared to the length of the P^3 channel of 20 meters. For example, for 180 MeV π^+, the percentage of muons and electrons in the beam was about 25% on the P^3 channel, but less than 3% on the LEP channel. For this channel, energies from 90 to 220 MeV were used.

A schematic layout of this channel is illustrated in Fig. 2-7. This channel utilizes 4 rectangular bending magnets and two extrance and exit quadrupoles. Removal of protons from beams containing π^+ is accomplished by means of an absorber located between the second and third ending magnets. The pion momentum resolution is set by a slit also located here. For most of the runs on this beam line $\Delta p/p$ was around 0.1%. Several runs near the scheduled shutdown of LAMPF were made at $\Delta p/p$ of about 4%. Beam size at the exit quadruple was a spot about 1 cm in diameter.

Typical beam contamination figures measured by the Nuclear Chemistry Pion Monitoring Group were about 10% u^+ and e^+ at 100 MeV and less than 1% at 220 MeV for beams containing π^+; and about 25% u^- and e^- at 100 MeV and less than 1% at 220 MeV for beams containing π^-. These figures

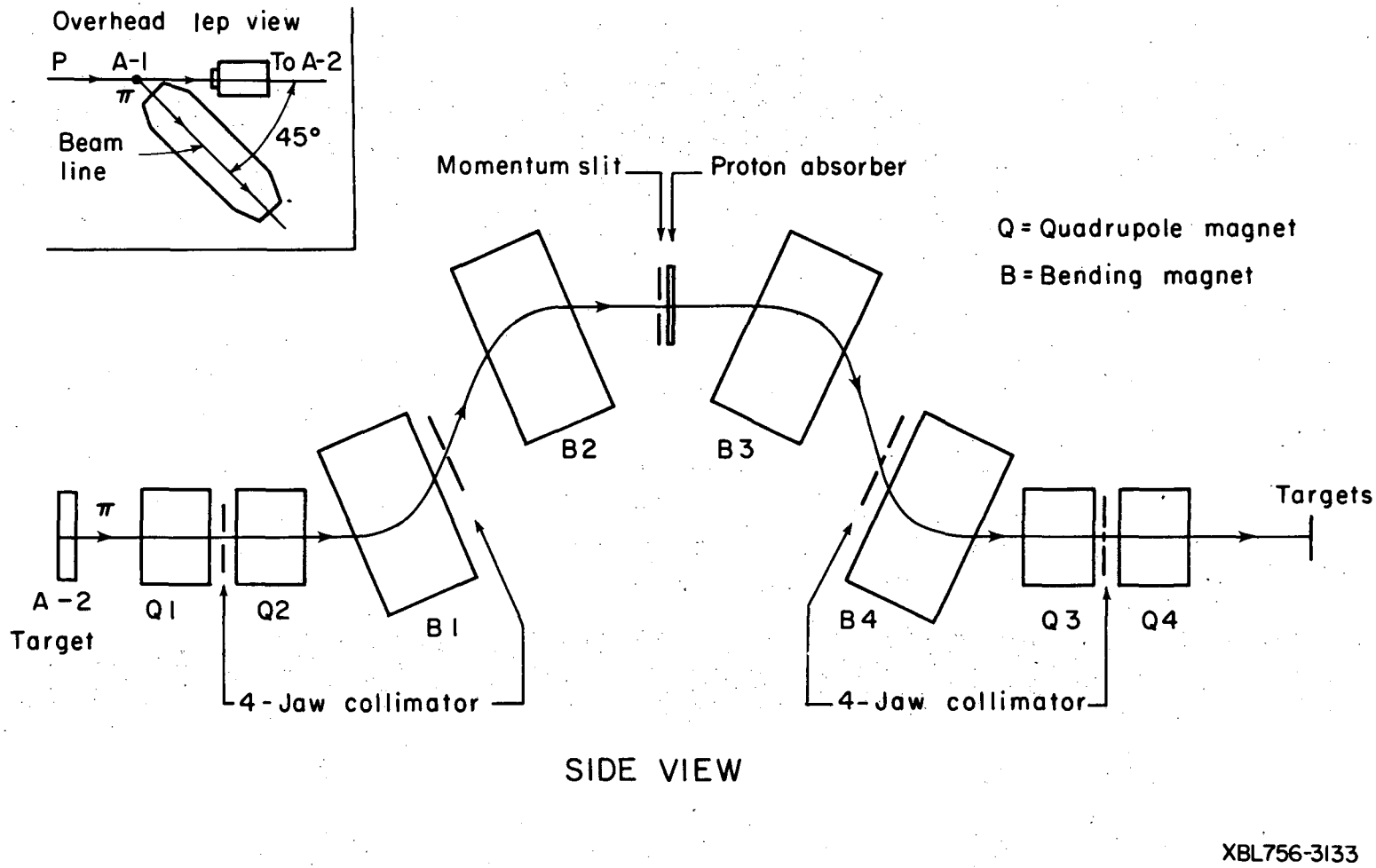

Fig. 2-7. The low energy pion channel (LEP) at LAMPF.

were obtained by employing the dE/dX techniques used previously for determining proton contamination in the P^3 π^+ beams.(88)

2.4 Counting Procedure

After exposure in the pion beams, the targets were quickly removed to a counting area. The decay of the product nuclei in the target and monitor discs was then followed for several half-lives by counting the two 511 keV gamma rays from positron annihilation in coincidence. The two detectors used in this work were each composed of a pair of 7.5 cm×7.5 cm NaI(Tl) crystals oriented at 180°. The counting for boron nitride and Teflon targets was initiated about 6 and 20 minutes respectively, after the beam shutoff in a coincidence detector in the Nuclear Chemistry Building and within 2 minutes for the boric acid target in a coincidence detector conveniently located in a P^3 counting house. The carbon monitor and target discs were wrapped in copper sheaths sufficiently thick (0.025, 0.05, 0.1, and 0.1 cm for Teflon, plastic, boron nitride, and boric acid targets, respectively) to annihilate all emitted positrons and were counted in identical geometries between the NaI(Tl) scintillators. Generally, the samples were alternated after every counting interval. Because the disc dimensions for target and monitor were equal, the efficiency for detection of positron annihilation quanta would also be equal, aside from small self-absorption corrections. This approach allowed relative reaction cross sections to be measured without knowing absolute detector efficiency. The backgrounds for the detectors in the Nuclear Chemistry laboratory and the P^3 counting house were about 2 and 25 counts/min respectively.

One exposure in which the pions in the beam were counted directly by a counter telescope required a knowledge of the coincidence efficiency for the detector in the Nuclear Chemistry Building. This was measured by first determining the absolute decay rate of ^{11}C in an irradiated plastic scintillator disc of size equal to a target disc in a β - γ coincidence detector and then by counting the positron annihilation gamma rays with the 511-511 keV counter. Several steps were taken prior to counting of the sample in the γ - γ detector. The exposed scintillator was first wrapped in a sheath of copper 0.05 cm. thick. Second, care was taken to make certain that the activated area in the plastic scintillator was very nearly equal in size to that produced by the beam spot in the actual irradiation. The γ - γ efficiency determined in this manner was then corrected for the greater self-absorption factors for Teflon versus the plastic scintillator. Derivation of these self absorption factors is discussed later in the text.

A final efficiency of (9.5±0.5)% was determined for the nuclear chemistry detection system by the above described method. Both γ - γ and β - γ detection systems are briefly discussed in the next section. The subject of counting of coincidence radiation for determining absolute disintegration rates has been previously reviewed by Remsberg.(94)

2.4.1 The Positron Annihilation Detector

A diagram of the system used to detect the 2 511 keV gamma rays from positron annihilation is illustrated in Fig. 2-8. Narrow energy windows were set on the 511 keV gamma ray peak in each channel. The delays in each branch were then set to maximize the coincidence rates, and the resolution time 2τ was adjusted to accept two pulses within a certain time interval.

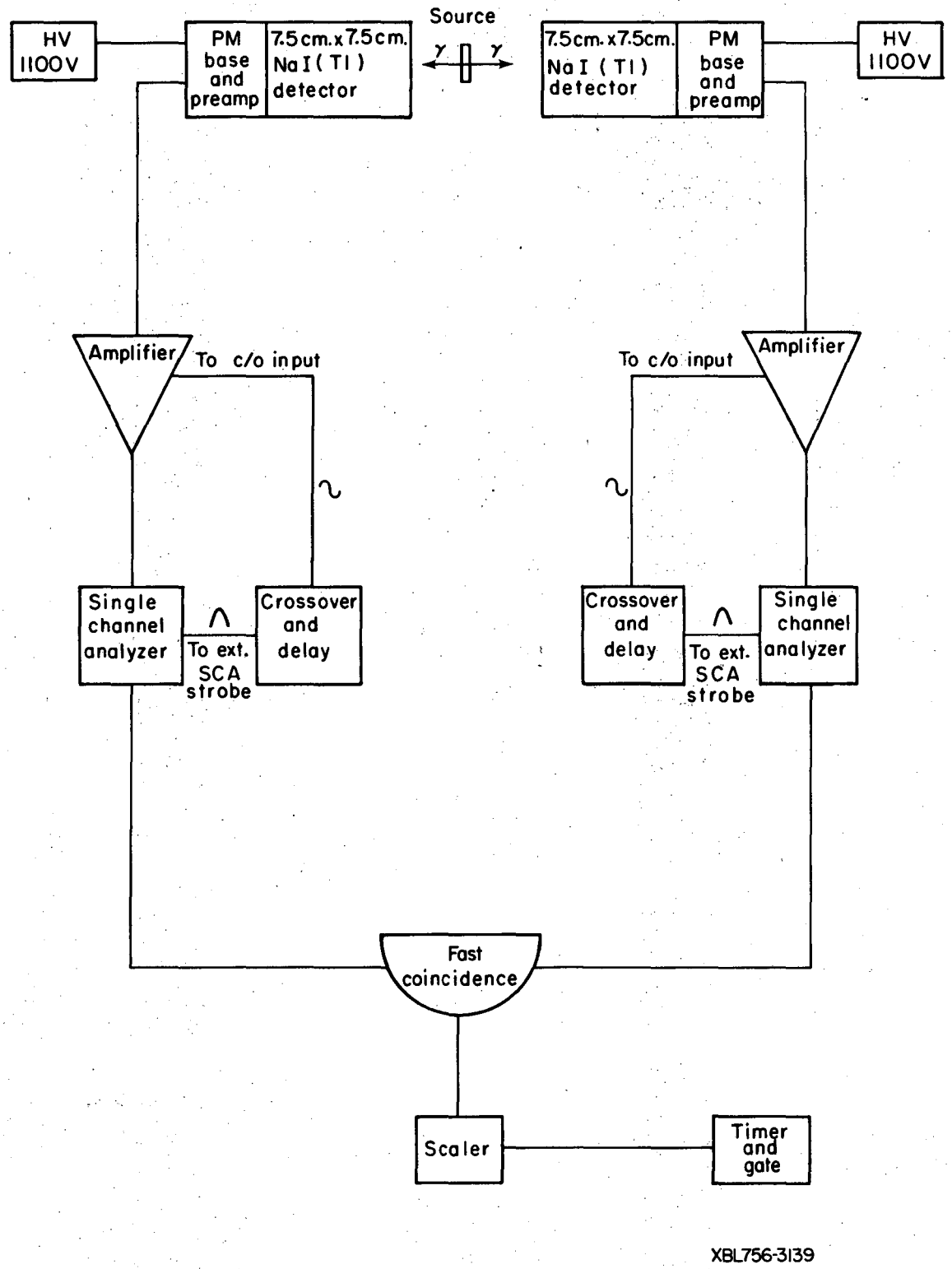

Fig. 2-8. The γ - γ coincidence detector.

For these experiments, the resolving time of each coincidence detector was 110 nanoseconds, which was the maximum limit on the coincidence modules.

2.4.2 The β - γ Coincidence Detector

This detector was used to determine absolute ^{11}C decay rates in an irradiated plastic scintillator by counting the coincidence between the emitted positron and one 511 keV annihilation gamma. The chief advantage for employing this method is its high efficiency for detection of positrons. This detection system is shown in Fig. 2-9.

The exposed plastic scintillator was first attached with optical coupling grease to an RCA 6655A phototube. Flashes of light, caused by the emitted positrons in the scintillator are detected by the phototube, which outputs pulses proportional to the energy deposited. The NaI(Tl) branch of the detector has its energy windows set to encompass the 511 keV annihilation gamma, while the lower threshold in the positron branch was set to discriminate against noise and still accept most of the spectrum of positrons. Beta, gamma, and beta-gamma coincidence rates were always output on scalers. From these numbers, the absolute counting rate of the ^{11}C in the plastic scintillator is given by

$$N_{abs} = \frac{N_\beta N_\gamma}{N_{\beta\gamma}}$$

where N_β is the number of counts observed in the beta branch, N_γ is the number of counts observed in the gamma branch, and $N_{\beta\gamma}$ is the number of observed beta-gamma coincidence counts. Generally, the positron detection efficiency, given by N/N_{abs} was about (90±3)%, a figure very consistent with the magnitudes of positron efficiencies attainable with

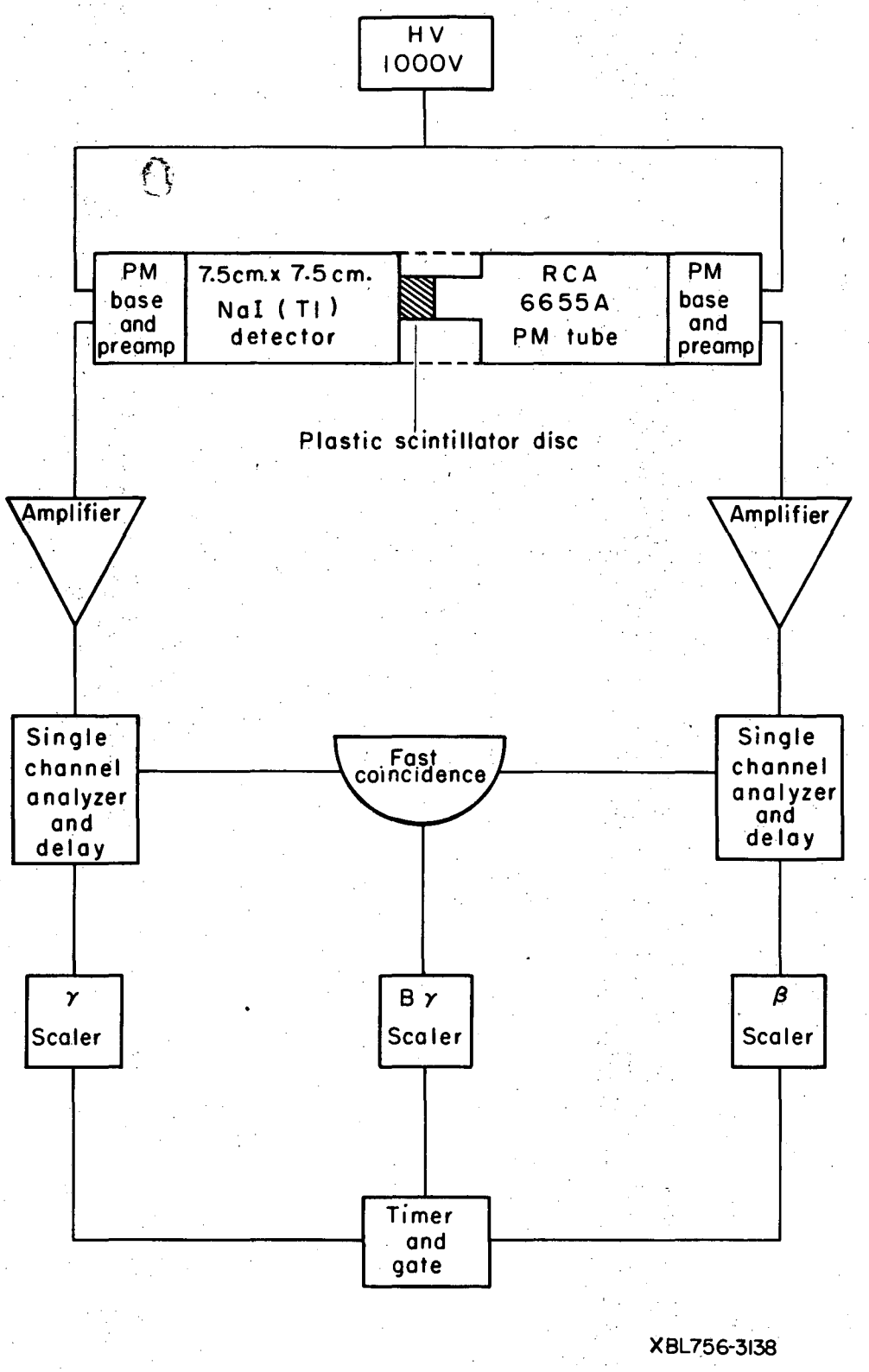

Fig. 2-9. The β - γ coincidence detctor.

the arrangement. Further corrections, such as for extended source size or for γ-ray efficiency of the β counter, could be added to improve the accuracy of this method to within 1%. The above formula, however, is acceptable for determining counting rates to within 3-4%.(94)

Typical backgrounds for the beta, gamma, and beta-gamma branches were about 60, 250, and less than 2 counts per minute, respectively.

2.5 Data Analysis

2.5.1 Decay Curves

All decay curves synthesized from counting of the exposed disc targets were fit by the standard least squares program CLSQ,(28) using fixed half-lives for each radioactive component. A summary of the product nuclei and their respective half-lives used in obtaining end of bombardment activities is given in Table 2-2.

2.5.1 A ^{12}C Monitor Target

The irradiation of a plastic scintillator or polyethylene disc in the high energy pion beams yielded only ^{11}C as the single component in the decay curve (^{7}Be is not produced singificantly). Figure 2-10 represents a typical ^{11}C decay curve obtained after exposure of a plastic scintillator disc with dimensions 3.8 cm diameter by 0.6 cm thick in a 180 MeV π^- beam in the LEP channel at LAMPF. Generally, the standard deviation of the initial activities as given by CLSQ was less than 3%.

2.5.1 B ^{14}N Target

Exposure of machined boron nitride discs in the high energy pion beams yielded ^{11}C and ^{13}N as detectable components of the decay curve. The decay curve from a 190 MeV π^- experiment at the P^3 channel at

Table 2-2. Decay Characteristics for the Observed Radionuclides

Nucleus	Half-Life (minutes)	Fraction of Decays leading to β^+ emission	Reference
^{11}C	20.4	1.0	22
^{13}N	9.96	1.0	22
^{15}O	2.05	1.0	22
^{18}F	109.8	0.97	22

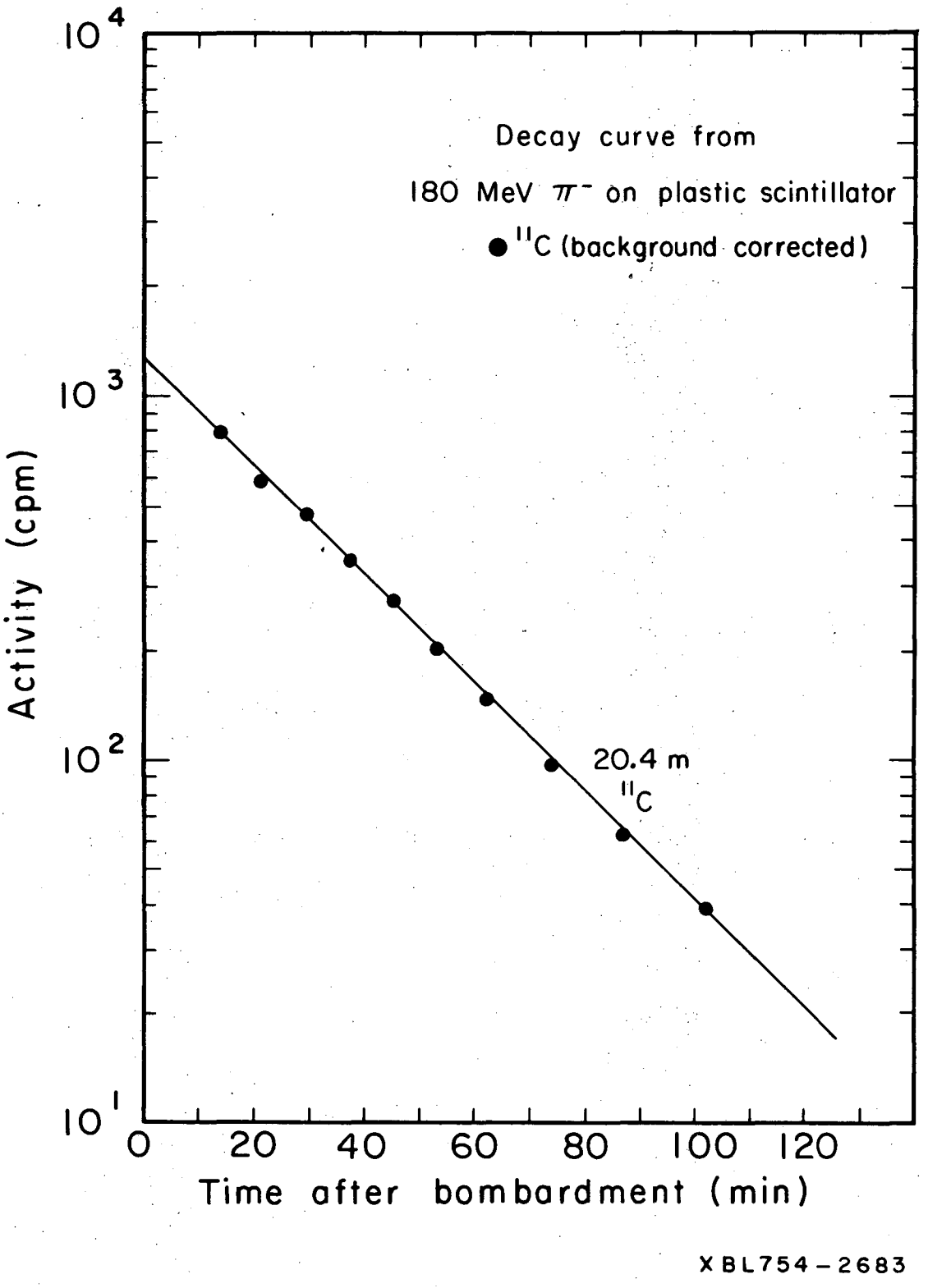

Fig. 2-10. Decay curve from 180 MeV π^- on plastic scintillator. The solid line is a CLSQ fit.(28)

LAMPF is illustrated in Fig. 2-11. The target dimensions in this case are 3.8 cm in diameter × 0.6 cm thick. It is noted here that the closeness in half-lives for ^{11}C and ^{13}N, 20.4 and 9.96 minutes respectively, in addition to the low yield of ^{13}N observed in this work, may be responsible for the standard deviations being a large 7-10% of the corresponding end of bombardment activities, as determined by CLSQ. The decay curve standard deviation for the ^{11}C component averaged less than 3%.

2.5.1 C ^{16}O Target

Three detectable radioactive nuclei ^{15}O, ^{13}N, and ^{11}C were unfolded from the gross decay curve from the exposure of boric acid targets in the high energy pion beams. A representative decay curve is shown in Fig. 2-12. Two different analyses showed ^{14}O to be formed in such relatively low yield that it could be ignored in the decay curve. The first approach was to include ^{14}O with a half-life of 1.19 minutes in the decay curve analysis. In every case in which this was done, a decay rate with a positive value, but having over 100% uncertainty, or a negative decay rate was obtained. The second method was to omit the first few points in the decay curve and then to compare the results of a CLSQ fit of this modified data to a CLSQ fit of the original data. If ^{14}O were present in sufficient quantities, a large difference in the ^{15}O end of bombardment activity between the two different fits should be observed. This difference, however, was always found to be less than 2-3%. The ^{14}O component in the decay curve was thus ignored.

Because of low statistics and low yield for the ^{13}N component in the decay curve, the CLSQ standard deviation for this nuclide was generally high 25% of the end of bombardment activity. The ^{15}O and ^{11}C initial

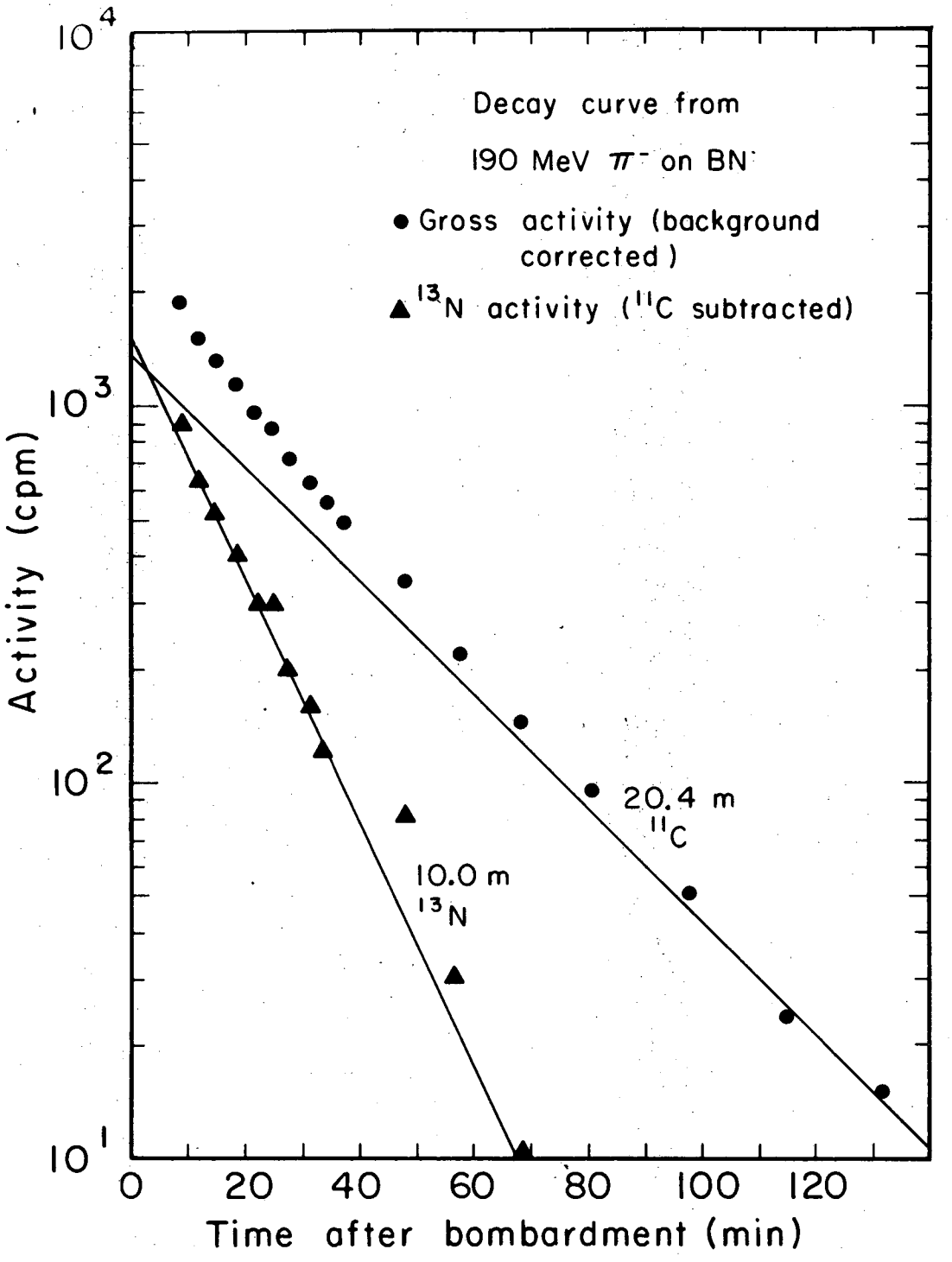

XBL754-2688

Fig. 2-11. Decay curve from 190 MeV π^- on BN. The solid lines are CLSQ fits to individual decay nuclides.(28)

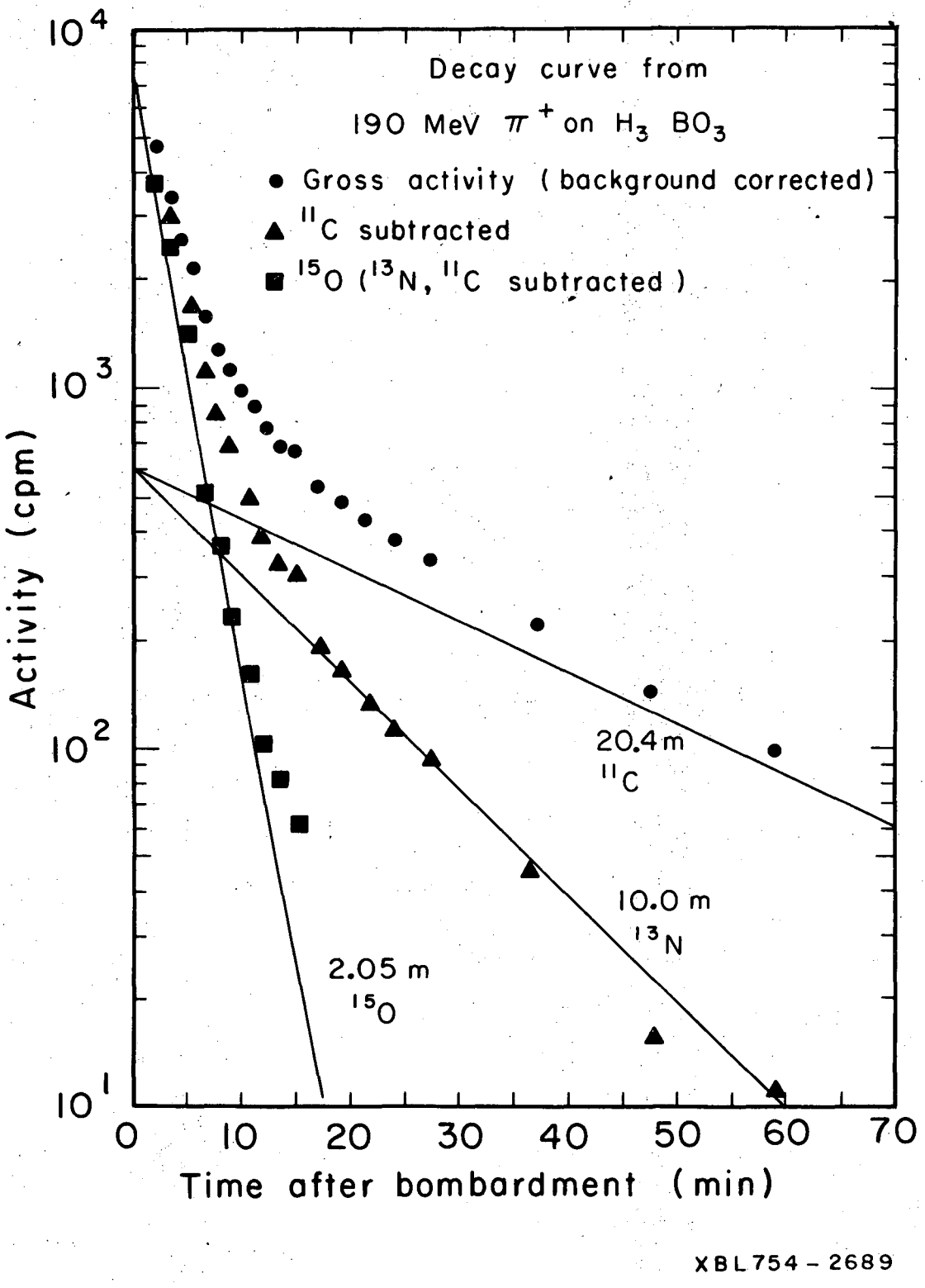

Fig. 2-12. Decay curve from 190 MeV π^+ on boric acid. The solid lines are CLSQ fits to individual decay nuclides (28)

activities could usually be determined statistically to within 5% and 10% respectively.

2.5.1 D ^{19}F Target

Generally, only ^{11}C and ^{18}F were present in the decay curve obtained by counting the activity induced in a Teflon disc target. A representative decay curve is shown in Fig. 2-13. Sufficient time was often allowed before counting to permit any ^{13}N produced in the reaction to decay. For experiments where many targets required judicous alternating in the counters, only the ^{18}F activity was usually measured.

The production of ^{11}C in the Teflon targets is a result of contributions from both the ^{12}C and ^{19}F present (Teflon = $(CF_2)_n$). In order to determine the cross section for formation of ^{11}C from ^{19}F, a large correction must be applied. The large error induced in cross section from this approach is a consequence of subtracting two large numbers. Errors to the ^{19}F(π,X) ^{11}C cross sections vary from about 10-25%.

Decay curve resolutions were less than 3% for the ^{18}F component and less than 5% for the gross ^{11}C component (from ^{19}F and ^{12}C) as given by CLSQ.

2.5.2 Corrections to the Data

2.5.2 A Beam Fluctuations

Intensity fluctuations in the pion beams during irradiations were monitored with almost every experiment either directly or indirectly. For the work done at the LBL 184-inch synchrocyclotron, the main proton beam rates were continuously measured by what essentially constituted an ammeter, set up by the physics experimenters. (91,92) During the course of these experiments at LBL, little or no main proton beam fluctuations

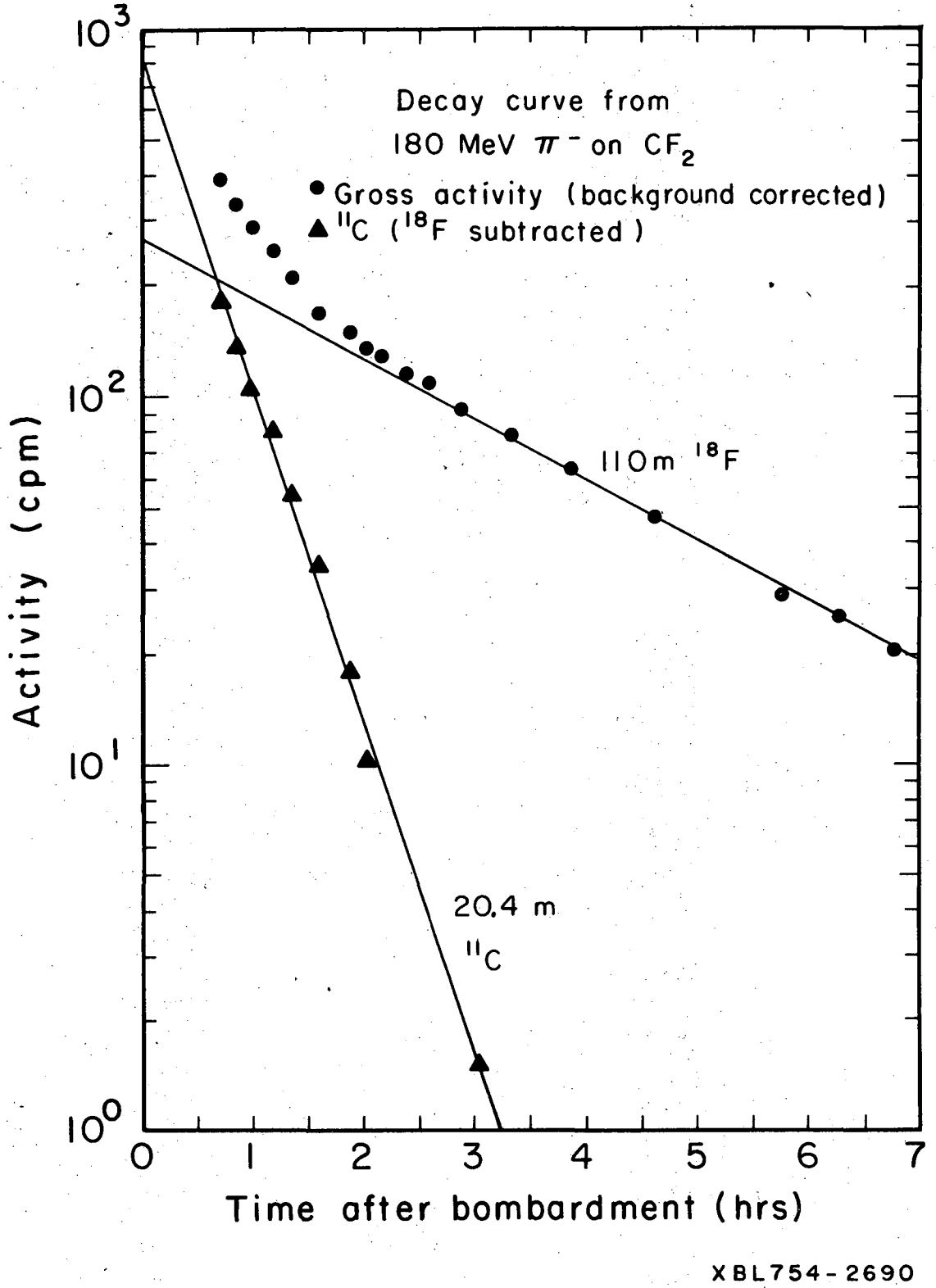

Fig. 2-13. Decay curve from 180 MeV π^- on Teflon. The solid lines are CLSQ fits to individual decay nuclides.(28)

were observed. It was assumed, then, that no fluctuations had occured in the pion beams. Thus, no corrections for beam fluctuations were made for the data accumulated at Berkeley. For the parasitic and independent exposures at LAMPF where fluxes less than 5×10^5 were encountered, the pion beam intensity was multiscaled continuously by counting the number of particles that passed through the counter telescope over a short time interval, storing this information in the memory of a multichannel analyzer, and then, repeating this procedure for the duration of the run. Then, for irradiations where the intensity of the beam varied significantly corrections could be applied to the reaction cross sections. Using the equation given in Nuclear and Radiochemistry by Friedlander, Kennedy, and Miller(95) for a varying rate of formation of product nuclei, the cross section $\sigma_T(X)$ for the production of X from target T, in terms of the $^{12}C(\pi^{\pm}, \pi N)\ ^{11}C$ monitor reaction is expressed as

$$\sigma_T(x) = \frac{D_0(X)}{D_0(^{11}C)} \frac{n_{^{12}C}}{n_T} \cdot \sigma_{^{12}C}(^{11}C) \frac{\sum_{i=1} I_i \left[1-e^{-\lambda 11_C \Delta t_i}\right] e^{-\lambda 11_C (t-t_i)}}{\sum_{i=1} I_i \left[1-e^{-\lambda_X \Delta t_i}\right] e^{-\lambda_X (t-t_i)}} \qquad (2\text{-}1)$$

where $D_0(X)$ and $D_0(^{11}C)$ are the end of bombardment decay rates of product x and ^{11}C, respectively, $n_{^{12}C}$ and n_T are the respective atomic surface densities of the monitor and target, Δt_i is the time interval over which the flux is measured, I_i is the number of particles counted in the time interval Δt_i, t_i is the time at the end of the ith interval, t is the length of bombardment, λ is the decay constant for a specific nuclide,

and $\sigma_{^{12}C}(^{11}C)$ is the cross section for the $^{12}C(\pi^{\pm},\pi N)\ ^{11}C$ reaction.

Only a few irradiations required saturation corrections, none of which amounted to more than 5% with application of Eq. (2-1).

2.5.2 B Proton Contamination in the π^+ Beams

For all experiments at the 184-inch synchrocyclotron, the proton component in the π^+ beams was completely filtered out by the carbon absorber in the beam line of the Physics Cave (Fig. 2-3). Proton contamination of the π^+ beams in the LAMPF P^3 channel (Fig. 2-6), however, became a problem beginning at approximately 350 MeV. Above this point, the graphite degrader in the channel could no longer completely eliminate the high energy protons in the beam. As a consequence, a substantial, if not at times intolerable fraction of the beam striking the final target contained protons, having the same momentum as the pions. In the worst cases, the p/π^+ ratio was observed to be as high as 1/1 at 400 MeV using the normal thickness of graphite degrader in P^3 East.

Later, proton contamination was significantly reduced to less than about 5%, by using degrader 5 to 8 cm thick, and by running instead on the P^3 West Leg. Apparently, the proton absorber, which functioned to absorb low energy protons still remaining in the channel, was more effective when the West Leg of P^3 was used.

The actual corrections to the cross sections obtained from using beams with contamination from protons was made in the following manner. Letting R(x) be the measured cross section for the formation of product X relative to the cross section for the monitor reaction $^{12}C \rightarrow {}^{11}C$, one obtains

$$R(x) = \frac{D_s(X)n_T}{D_s(^{11}C)n_{^{12}C}} = \frac{\sigma_\pi(X) + f\,\sigma_p(X)}{\sigma_\pi(^{11}C) + f\,\sigma_p(^{11}C)} \qquad (2\text{-}2)$$

where the various symbols are defined as follows:

$D_s(X)$ = saturation activity of product X

$D_s(^{11}C)$ = saturation activity of ^{11}C

n_T = surface density of the target atoms

$n_{^{12}C}$ = the surface density of ^{12}C atoms

$\sigma_\pi(X)$ = pion cross section for the reaction $T \rightarrow X$

$\sigma(^{11}C)$ = pion cross section for the reaction $^{12}C \rightarrow {}^{11}C$

f = the ratio of protons/pions in the beam

$\sigma_p(X)$ = the proton cross section for the reaction $T \rightarrow X$

$\sigma_p(^{11}C)$ = the proton cross section for the reaction $^{12}C \rightarrow {}^{11}C$.

Since cross sections for (p,pn) (33) but not for the more complex (p,X) spallation reactions are well-established for the targets in this work, only corrections to the (π,πN) cross sections were made.

The first four quantities defined above are determined as a consequence of the experiment. Cross sections for the monitor reaction $^{12}C(\pi^{\pm},\pi N)^{11}C$ have been accurately measured.(88) The cross sections for the (p,pn) reactions needed in the correction were taken from the compilation by Caretto.(33) The kinetic energy of the proton striking the target was calculated by assuming that all particles in the beam (u^+, e^+,π^+,p) had the momentum for which the channel was originally tuned.

Values for f were independently obtained from a dE/dX measurement made by the Nuclear Chemistry Pion Monitoring Group. Generally, for the four exposures in this work that required correction (368,370,380 and 430 MeV), the proton contamination in the beams never exceeded 5%.

The remaining quantity $\sigma_{\pi}(X)$ then, may easily be calculated. The corrections to the $(\pi,\pi N)$ cross sections from (p,pn) reactions were generally low and found to be in the range of 1-5%.

2.5.2 C Self-Absorption of 511 keV Quanta

As mentioned previously in the text, the efficiencies of the γ-γ detector for coincident 511 keV gamma rays from positron annihilation for disc targets of equal thickness are also equal, except for small self-absorption corrections. For example, discs of boron nitride and Teflon are approximately twice as dense as a plastic scintillator of the same dimensions. Furthermore, nitrogen and fluorine have greater atomic numbers than carbon. The boron nitride and Teflon discs, then, should attenuate the two 511 keV gamma rays originating within the samples to a greater degree than would the plastic disc.

In this work, the relative attenuation factors for the primary disc targets relative to the plastic monitor disc were measured for each different target thickness in the following manner. A standard ^{22}Na IAEA source was taped to what was defined as the "back" side of a primary disc target. With this back side of the disc turned away, a Ge(Li) measurement was made of the number of counts in the 511 keV photopeak (from positron annihilation). This entire procedure was then repeated for a plastic monitor disc of equal dimensions. Then, the ratio of primary target to monitor intensities yielded a good experimental measurement

of the relative self-absorption factors. Table 2-3 provides a summary of these relative self-absorption factors determined from such measurements. Effectively, these corrections imply a lower counting efficiency of the coincidence detector for Teflon and boron nitride relative to the plastic monitor, and essentially no efficiency difference between the boric acid and monitor discs.

2.5.2 D Secondary Reactions from Thick Targets

The use of targets on the order of g/cm^2 for this study presented the possibility of internally generated cascade nucleons causing secondary nuclear reactions leading to the desired product nuclides. A usual empirical approach to the measurement of this effect would be to irradiate a "sandwich" of the usual target between two thick targets of the same material.

A slightly modified procedure was used. Since all the cross sections in this work were originally measured relative to the $^{12}C(\pi^{\pm},\pi N)^{11}C$ reaction, a study of the relative cross section increase as a function of two different target thicknesses was made. This was accomplished by varying the thickness of the monitor and primary target discs, but still keeping the thicknesses of these discs equal for every exposure. These results are given in Table 2-4 for Teflon and boron nitride targets with both positive and negative pions. The data show that the change in relative cross section from the use of thick targets is small, and not significantly outside of statistical errors to warrant correction.

As seen from Table 2-4 secondary effects may be considered not important for the more complex reactions as well. Contributions from secondary particles to these more complex spallation reactions would be

Table 2-3. Self-Absorption Factors (relative to a plastic disc)[a]

Primary Target Material	Primary Target Thickness (cm)		
	0.3	0.6	1.25
Teflon	0.975	0.945	0.901
Boron Nitride	0.990	0.975	0.950
Boric Acid	-----	-----	1.02

[a]These figures were also applied for the few experiments that used a polyethylene monitor.

Table 2-4. A Summary of Relative Cross Section Versus Total (Monitor + Primary Target) Thickness

^{14}N: Target= BN + Plastic

Pion Kinetic Energy (MeV)	Relative Cross Section[b] ^{13}N 1.25 cm	^{11}C 1.25 cm	^{13}N 2.54 cm	^{11}C 2.54 cm	σ(Rel)/cm(%) ^{13}N	^{11}C
293±10 π^+ [a]	0.238±0.033	0.587±0.028	0.220±0.015	0.595±0.016	-6.1±12.2	1.1±4.4

^{19}F: Target=$(CF_2)_n$ + Plastic

Pion Kinetic Energy (MeV)	Relative Cross Section[b] ^{18}F 1.25 cm	^{11}C 1.25 cm	^{18}F 2.54 cm	^{11}C 2.54 cm	σ(Rel)/cm(%) ^{18}F	^{11}C
177±12 π^+	0.687±0.011	--------	0.694±0.010	--------	0.8±0.7	-------
297±10 π^+	0.724±0.018	0.380±0.024	0.616±0.014	0.343±0.029	-11.9 ±2.5	-16.0±6.4
			0.683±0.014	0.343±0.029	-4.5±2.5	-7.8±7.9
157±11 π^-	0.799±0.037	--------	0.754±0.027	--------	-4.5±4.6	------
297±11 π^-	0.744±0.025	0.223±0.054	0.698±0.023	--------	-4.9±3.7	------

[a]This energy is the mean of two runs at 290±9 and 296±11 MeV.

[b]Errors on the relative cross sections are rms errors of the end of bombardment activities as given by CLSQ for the plastic and primary discs.

expected to be small because of the high reaction thresholds. Thus, no corrections to any of the cross sections (including ^{16}O, although no independent study was performed) were deemed necessary.

2.5.2 E Other Considerations

Attention was also given to the following effects:

(1). The Fast Neutron Background - As mentioned previously in the text, the exposure of dummy targets outside of the area of the beam revealed no significant contribution from this effect.

(2). Lepton Reactions - Although no independent determination was made for the contribution of lepton reactions to the measured cross sections, it may be safely assumed that the muons and electrons in the pion beams are too weakly interacting, compared to the strongly interacting pions, to cause significant nuclear transmutations.

(3). $^{11}B \rightarrow {}^{11}C$ "Impurity" Charge Exchange Reactions

(a) $\pi^{\pm}$ + BN- the cross sections for the formation of ^{11}C from boron nitride have contributions not only from the primary $^{14}N(\pi^{\pm},X)^{11}C$ reaction, but also, from the secondary $^{11}B(p,n)\ ^{11}C$ and for the case of π^{+}, the $^{11}B(\pi^{+},\pi^{0})\ ^{11}C$ reaction. Since the one BN thickness experiment (Table 2-4) showed no effect that could be ascribed to secondary production, corrections to the ^{11}C cross section for the (p,n) reaction were ignored. The $^{11}B(\pi^{+},\pi^{0})\ ^{11}C$ reaction, however, has a cross section of about 5 mb at the (3,3) resonance, as measured in the work of Chivers et al.(71) This compares to a gross cross section of about 25 mb for the π^{+} + BN $\rightarrow\ ^{11}C$ reaction. Because ^{11}B constitutes approximately 35% of the mass of BN, the pion charge-exchange reaction may contribute up to 8% of the gross ^{11}C cross section from BN. Due to a lack of

accurate cross section data for the charge-exchange reaction, no correction could be applied for its effect.

(b) $\pi^{\pm}$ + H_3BO_3 - The proton and pion charge-exchange possibilities discussed in the preceding paragraph may also produce ^{11}C. Since secondary effect corrections were shown to be small for BN and Teflon targets (Table 2-4), no corrections for the $^{11}B(p,n)$ ^{11}C reaction were deemed necessary. In boric acid, the boron constitutes only about 1/6 of the mass and the charge exchange cross section of about 5 mb at 180 MeV is roughly 1/4 of the total cross section for the production of ^{11}C from the target (the gross cross section measured in this work if about 21 mb at the (3,3) resonance). Thus, one can expect an estimated contribution of about 5% from the $^{11}B(\pi^+,\pi^0)$ ^{11}C reaction, and the remainder coming from the primary reaction $^{16}O(\pi^+,X)$ ^{11}C.

(4). Production of ^{11}C from Teflon - In order to determine the cross section for the $^{19}F(\pi,X)$ ^{11}C reaction, corrections must be made for the contribution of the ^{12}C in the Teflon to the ^{11}C production. Since the $^{12}C(\pi^{\pm},\pi N)$ ^{11}C reaction has appreciable cross sections (45 mb for π^+, 70 mb for π^- at about 180 MeV) (88) and ^{12}C is about 25% of the mass of the Teflon target, rather large correction factors were applied. The cross sections determined in this manner are believed accurate to only about 25%.

(5). Reactions from the aluminum can - Since the aluminum can that contained the boric acid power was only 0.013 cm thick (compared to the sample of boric acid inside that was 1.3 cm thick), one may safely assume that it made no significant contributions to the $\pi^{\pm}$ + boric acid cross sections.

(6). Accidental Counts in the γ-γ Detector - The low counting rates and moderately short resolving time of about 0.1 μsec for the coincidence detector imply low or insignificant contribution from this effect. A calculation to this end for the case of the most intense sample generated in this work demonstrated that at most, only 2% of the observed counting rate was due to accidental counts.(94) Since all other exposed samples were less intense, no corrections were made.

3. RESULTS

The cross sections for the $(\pi^{\pm},\pi N)$ and other more complex spallation reactions are summarized in Tables 3-1 through 3-3. Also tabulated at each individual pion energy is the number of determinations (in parentheses), the cross section for the $^{12}C(\pi,\pi N)\ ^{11}C$ reaction, the dimensions of the monitor and primary discs, and the external beam used for that particular exposure. The energy of the pion at the midpoint of the thick targets was taken as the effective bombarding energy. Initial pion energies were corrected for energy losses suffered in traveling through upstream targets (at LAMPF, for example, the pion beams often traveled through four (4) thin scintillators of total thickness 1.3 cm prior to striking the disc targets used in this study)and from the face of the disc stack to its midpoint. The spread in a pion energy is the root-mean-square combination of the beam momentum resolution Δ obtained from the group responsible for the beam line, and the energy loss in the target itself (δ). Quantitatively, then, the effective bombarding energy may be expressed as

$$E_{\pi} = (E_1 - \delta) + (\Delta^2 + \delta^2)^{\frac{1}{2}} \qquad (3\text{-}1)$$

where E_1 is the pion energy prior to striking the targets. The values for δ were estimated from the range curves of Trower.(96).

Errors on the reaction cross sections are purely statistical, and

Table 3-1. Cross section for pion reactions ^{14}N

π^- Energy (MeV)	$\sigma_N(^{13}N)$ [mb]	$\sigma_N(^{11}C)$ [mb]	$\sigma_C(^{11}C)$[a] [mb]	Target and Monitor Disc (cm) Dimensions	Beam[b]
96±10	6.8±0.4(2)	10.8±0.3(2)	30.4±10%	5×1.3	MC
126± 2	10.7±1.3(1)	13.0±0.9(1)	48.7	3.8×0.6	LEP
144± 4	13.1±0.8(1)	17.3±0.6(1)	59.4	5×0.6	$P^3(\varepsilon)$
166± 4	15.3±1.4(1)	18.0±1.1(1)	67.5	3.8×0.6	$P^3(\varepsilon)$
188±15	14.8±0.5(1)	21.1±0.4(1)	69.9	3.8×0.6	$P^3(\varepsilon)$
233± 6	14.8±0.5(1)	22.6±0.3(1)	64.2	5×0.6	$P^3(\varepsilon)$
256± 4	12.1±0.9(1)	16.1±0.6(1)	56.7	3.8×0.6	$P^3(\varepsilon)$
296±11	10.6±1.3(2)	20.1±1.4(2)	45.2	5×1.3	PC
328± 9	8.4±0.5(1)	14.8±0.4(1)	37.8	5×0.6	$P^3(\varepsilon)$
433± 9	5.8±0.5(1)	8.4±0.4(1)	23.5	5×0.6	$P^3(\varepsilon)$
π^+					
98± 2	6.9±0.7(1)	19.5±0.6(1)	32.5±10%	3.8×0.6	LEP
136± 2	8.6±1.0(1)	23.1±0.8(1)	43.7	3.8×0.6	LEP
146± 2	8.8±1.3(1)	24.1±1.2(1)	44.9	3.8×0.6	LEP
156± 2	8.6±0.8(1)	25.0±0.6(1)	45.7	3.8×0.6	LEP
167± 5	8.0±0.8(1)	25.6±0.7(1)	45.8	3.8×0.6	$P^3(\varepsilon)$
176± 2	8.9±0.9(1)	24.6±0.7(1)	45.2	3.8×0.6	LEP
256±10	7.1±0.7(1)	17.3±0.6(1)	30.9	5×1.3	PC
290± 9	6.1±0.8(1)	15.0±0.7(1)	25.5	3.8×0.6	$P^3(\varepsilon)$
296±11	5.5±0.9(1)	15.0±0.7(1)	25.5	5×1.3	PC(ε)
336±11	5.9±0.4(1)	12.1±0.4(1)	25.2	5×1.3	$P^3(\varepsilon)$

(continued)

Table 3-1 (continued)

π^- Energy (MeV)	$\sigma_N(^{13}N)$ [mb]	$\sigma_N(^{11}C)$ [mb]	$\sigma_C(^{11}C)$[a] [mb]	Target and Monitor Disc (cm) Dimensions	Beam[b]
370±10	4.2±0.8(1)	12.7±0.6(1)	21.1	3.8×0.6	$P^3(\omega)$
430±10	5.9±0.9(1)	12.9±0.4(1)	23.7	3.8×0.6	$P^3(\omega)$

[a]Reference 88. Errors on these cross sections are conservatively assumed to be ± 10%.

[b]MC = Meson Cave (LBL)
PC = Physics Cave (LBL)
LEP = Low Energy Pion Channel (LAMPF)
P^3 = High Energy Pion Channel (LAMPF) (ε = East, ω = West)

Table 3-2. Cross sections for pion reactions on ^{16}O

π^- Energy (MeV)	$\sigma_0(^{15}O)$ [mb]	$\sigma_0(^{13}N)$ [mb]	$\sigma_0(^{11}C)$ [mb]	$\sigma_0(^{11}C)^a$ [mb]	Target and Monitor Disc (cm) Dimensions	Beam[b]
98±10	34.6±2.2(1)	3.6±1.5(1)	10.8±1.1(1)	31.7±10%	6.4×1.3	MC
188± 8	70.6±2.1(2)	7.1±2.0(2)	17.7±1.8(2)	69.9	6.4×1.3	$P^3(\varepsilon)$
348±23	31.6±0.9(1)	3.4±0.8(1)	10.9±0.8(1)	33.6	6.4×1.3	$P^3(\omega)$
π^+						
82± 4	25.1±1.5(1)	7.5±0.4(1)	17.2±2.7(1)	25.9±10%	6.4×1.3	LEP
188± 9	41.9±0.5(2)	8.2±0.5(2)	20.8±0.5(2)	44.9	6.4×1.3	$P^3(\varepsilon)$
298±10	24.6±0.9(2)	1.9±1.0(1)	15.5±0.5(2)	25.0	6.4×1.3	PC
380±10	21.6±1.3(1)	6.8±0.6(1)	14.0±1.4(1)	21.2	6.4×1.3	$P^3(\omega)$

[a]Reference 88. Errors on these cross sections are conservatively assumed to be ±10%.

[b]MC = Meson Cave (LBL)
PC = Physics Cave (LBL)
LEP = Low Energy Pion Channel (LAMPF)
P^3 = High Energy Pion Channel (LAMPF) (ε = East, ω = West)

Table 3-3. Cross sections for pion reactions on ^{19}F

π^- Energy (MeV)	$\sigma_F(^{18}F)$ [mb]	$\sigma_F(^{11}C)$ [mb]	$\sigma_C(^{11}C)$[a] [mb]	Target and Monitor Disc (cm) Dimensions	Beam[b]
45± 5	7.6±0.2(2)		4.0±10%	5×0.6	MC
96± 2	26.3±0.5(1)	3.5±0.6(1)	30.5	3.8×0.6	LEP
98±10	30.5±0.3(3)		31.7	5×0.6	MC
116± 4	34.7±0.8(1)	5.6±1.0(1)	43.4	3.8×0.6	LEP
157±11	50.4±1.4(2)		65.0	5×(0.6-13)	PC
178± 2	52.4±0.7(1)	9.4±1.0(1)	69.4	5×0.6	LEP
178± 2	50±3 (1)	7.0±0.7(1)	69.4	5×0.6	LEP
206± 4	49.6±0.8(1)	9.3±1.1(1)	69.7	3.8×0.6	$P^3(\varepsilon)$
247±17	44.0±0.4(1)		59.9	3.8×0.6	$P^3(\varepsilon)$
280± 6	33.6±0.3(1)	7.6±0.5(1)	49.5	5×0.6	$P^3(\varepsilon)$
297±11	32.5±0.8(2)	10.0±2.4(1)	45.2	5×(0.6-1.3)	$P^3(\varepsilon)$
328± 9	28.1±0.8(1)	9.0±0.8(1)	37.8	5×0.6	$P^3(\varepsilon)$
433± 8	16.9±0.2(1)	5.2±0.6(1)	23.5	5×0.6	$P^3(\varepsilon)$
546±10	15.4±0.5(1)		18.6	5×0.6	$P^3(\varepsilon)$
π^+					
96± 3	22.4±0.5(1)	7.3±0.6(1)	32.1±10%	3.8×0.6	$P^3(\varepsilon)$
117± 4	27.2±0.2(1)		39.7	3.8×0.6	LEP
146± 3	29.4±0.4(2)	12.7±0.6(2)	44.9	3.8×0.6	LEP
177±12	31.2±0.3(2)		45.2	5×(0.6-1.3)	PC
226± 4	25.7±0.4(1)	11.3±0.6(1)	37.5	3.8×0.6	$P^3(\varepsilon)$

(continued)

Table 3-3 (continued)

π^- Energy (MeV)	$\sigma_F(^{18}F)$ [mb]	$\sigma_F(^{11}C)$ [mb]	$\sigma_C(^{11}C)$[a] [mb]	Target and Monitor Disc (cm) Dimensions	Beam[b]
258± 9	19.1±0.5(1)	9.4±0.7(1)	30.6	5×0.6	PC
297±10	16.7±0.2(3)	8.4±0.3(3)	25.0	5×(0.6-1.3)	PC
336±12	15.5±0.2(1)	7.9±0.3(1)	22.2	5×0.6	PC
368±10	14.4±0.4(1)	8.4±0.8(1)	21.3	5×0.6	$P^3(\omega)$

[a]Reference 88. Errors on these cross sections are conservatively assumed to be ± 10%.

[b]MC = Meson Cave (LBL)
PC = Physics Cave (LBL)
LEP = Low Energy Pion Channel (LAMPF)
P^3 = High Energy Pion Channel (LAMPF)

were established from the root-mean-square combinations of standard deviations of the end of bombardment activities for monitor and target discs as given by the least squares code CLSQ. On the average, these statistical errors were 10%, 5%, and 3% for the $(\pi,\pi N)$ cross sections for ^{14}N, ^{16}O, and ^{19}F respectively, about 10% or less for the more complex spallation reactions. Where duplicate measurements were made, a weighted mean $\bar{\sigma}$ and standard deviation $\bar{X}$ were calculated according to the following formulas

$$\bar{\sigma} = \sum_i \omega_i \sigma_i / \sum_i \omega_i \qquad (3\text{-}2)$$

$$\bar{X} = \left[\sum_i \omega_i\right]^{-\frac{1}{2}} \qquad (3\text{-}3)$$

where σ_i = the individual cross section measurement and $\omega_i = (\frac{1}{s.d})^2$ with the notation s.d. representing the standard deviation of an individual cross section. This approach was applied in order to weight the statistically superior cross section measurement(s) more heavily. For example, it was not uncommon in this work to perform duplicate measurements at one energy where the two pion fluxes differed by a factor of 10-20. (This difference was often clearly reflected in the observed activities in the targets after exposure).

Since decay characteristics for the observed nuclei are well-known and the efficiencies (with corrections) for γ-γ detection of target and monitor discs were equal, the only dominant systematic error for the pion work would be attributed to the $^{12}C(\pi^{\pm},\pi N)\ ^{11}C$ cross sections. From the work of Dropesky et al., (88) this error appears to be about 5-10%. For the one exposure where the pions passing through the Teflon target were counted with the 3-element scintillation telescope belonging to the Pion Monitoring Group,(88) the γ-γ detector efficiency was

measured to within 6%. Thus, the total root-mean-square error in absolute cross section determination would vary from 5-15%. The cross sections for the $^{19}F(\pi^{\pm},X)\ ^{11}C$ reaction would be larger (about 25%) due to the nature of corrections applied to this data (see Section 2.5.2 E).

The excitation functions for the $(\pi^{\pm},\pi N)$ and other more complex (π,X) spallation reactions are presented in Figs. 3-1 through 3-4. The cross section value of 50 ± 3 mb for the $^{19}F(\pi^{-},\pi^{-}n)\ ^{18}F$ reaction at 178 MeV measured by the direct counting of pions is in very good agreement with the value of 52.4 ± 0.7 determined by simultaneous exposure of a plastic scintillator monitor and Teflon disc.

4. DISCUSSION

4.1 Features and qualitative Interpretation of the Results

The broad peaks that appear in the $(\pi^{\pm},\pi N)$ and the $(\pi^{\pm},X)$ excitation functions at about 180 MeV incident pion energy clearly illustrate the preservation of the (3,3) resonance, and thus, lend credence to the concept of quasi-free pion-nucleon collisions in these reactions. An additional clue for anticipating the resonance behavior for the more complex reactions is that the $\pi^{-} + {}^{12}C$ inelastic (reaction) cross section exhibits a broad peak at about 150 MeV.(97)

Figure 4-1 demonstrates the striking differences in cross section magnitudes for the $(\pi^{\pm},\pi N)$ reactions. In order, however, to compare these excitation function shapes and magnitudes more systematically, a normalization analysis similar to that made for comparing (p,2p) cross sections (Section 4.2.4 for Part I) was employed. By scaling all the $(\pi^{\pm},\pi N)$ curves to match the $^{12}C(\pi^{\pm},\pi N)\ ^{11}C$ data of Dropesky and coworkers,(88) one obtains two sets of "universal" π^{+} and π^{-} excitation

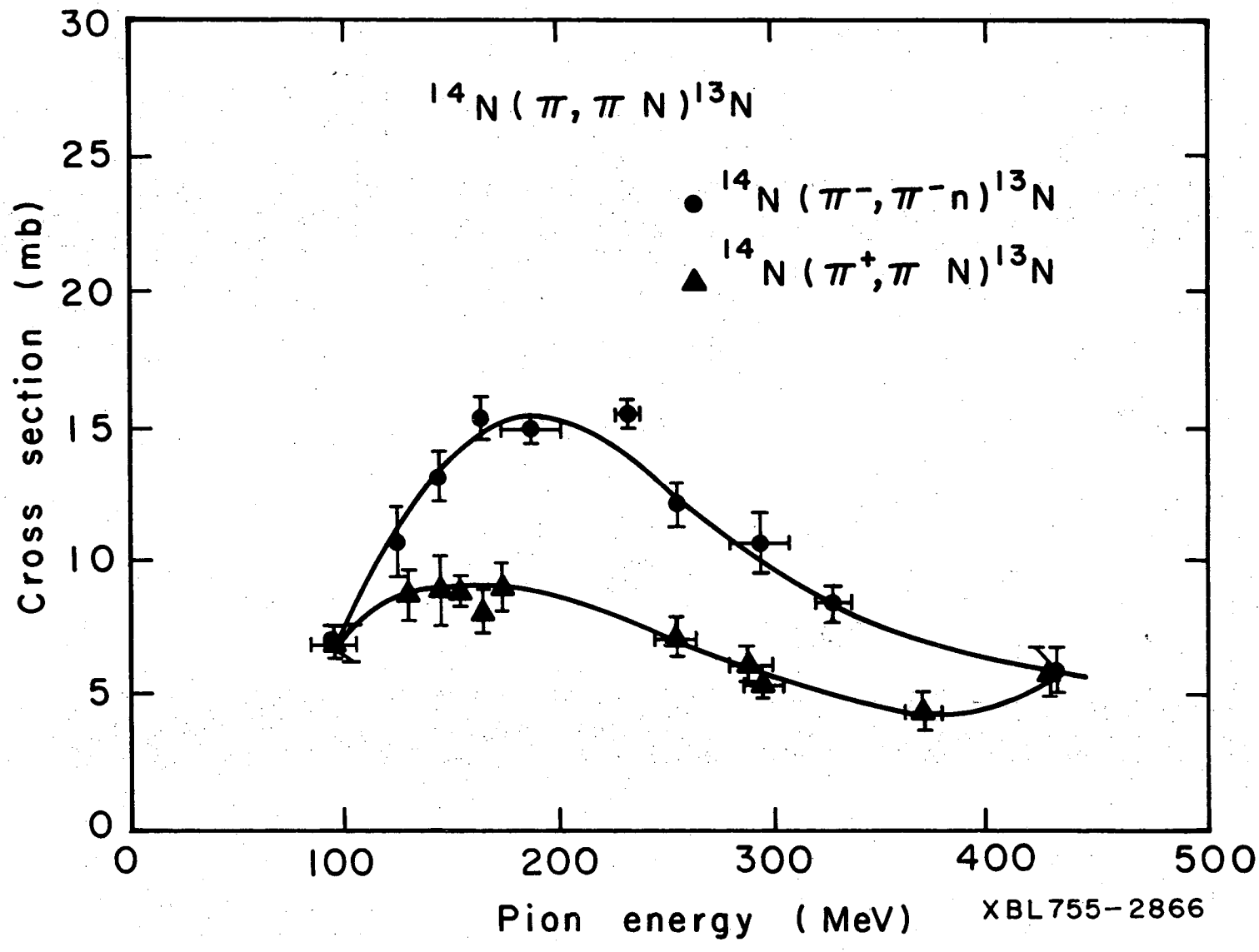

Fig. 3-1. Excitation functions for the $^{14}N(\pi^{\pm},\pi N)\,^{13}N$ reactions. Smooth curves have been drawn through the points as a visual aid.

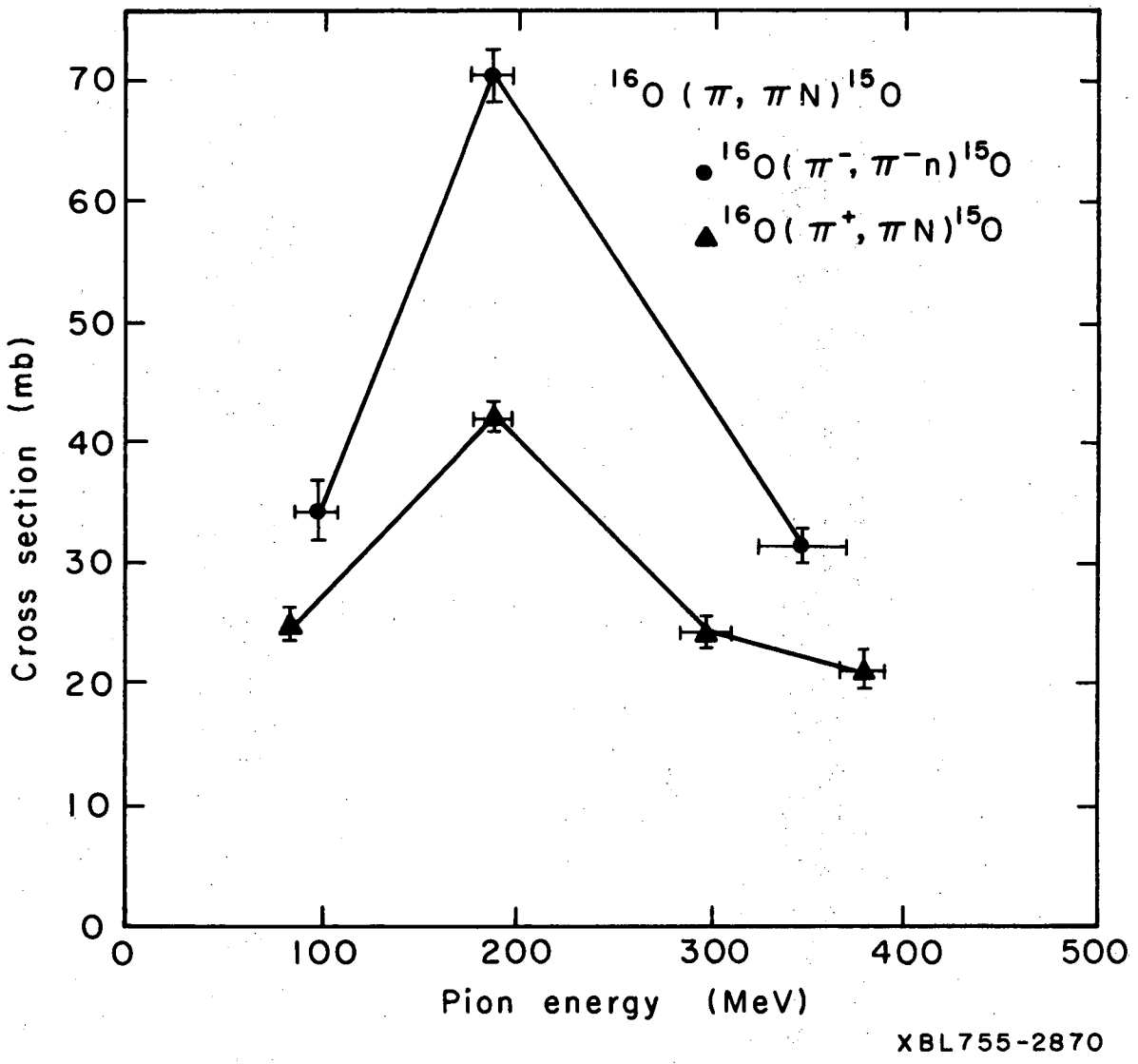

Fig. 3-2. Excitation functions for the $^{16}O(\pi^{\pm},\pi N)\ ^{15}O$ reactions. Lines connecting the points have been drawn as a visual aid.

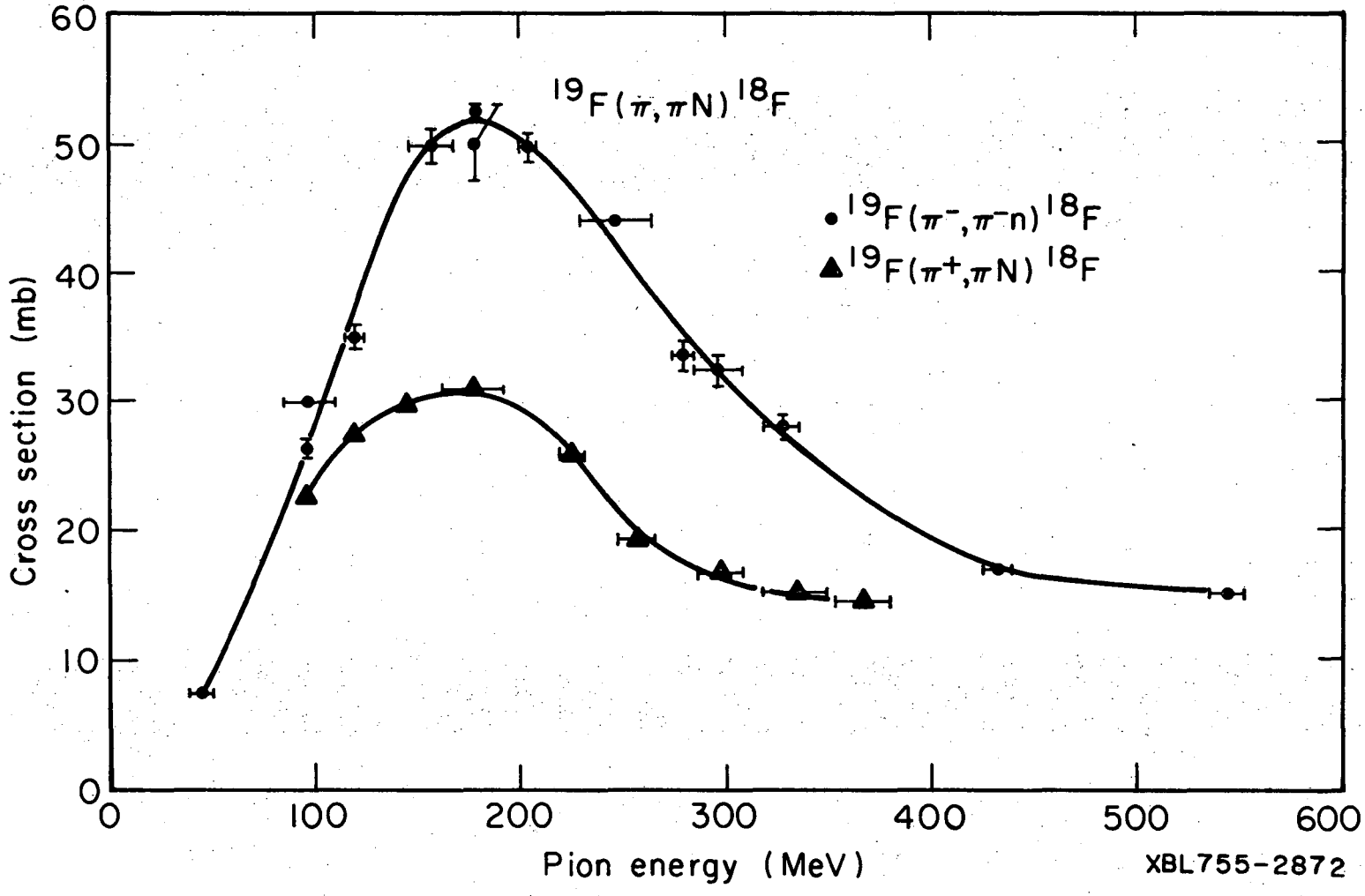

Fig. 3-3. Excitation functions for the $^{19}F(\pi^{\pm},\pi N)\ ^{18}F$ reactions. Smooth curves have been drawn through the points as a visual aid.

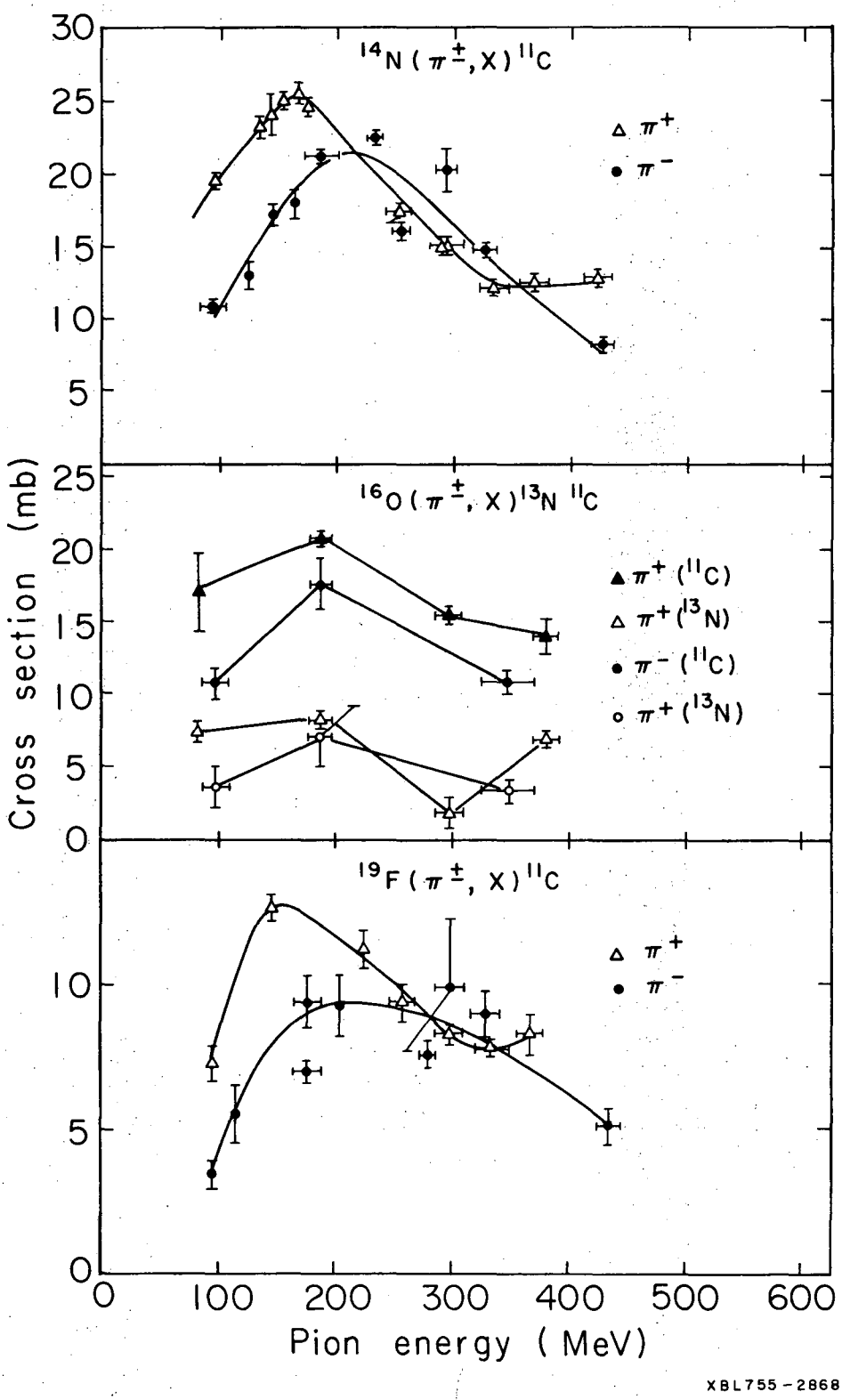

Fig. 3-4. Excitation functions for the more complex pion-induced spallation reactions. Lines have been drawn through the points as a visual aid.

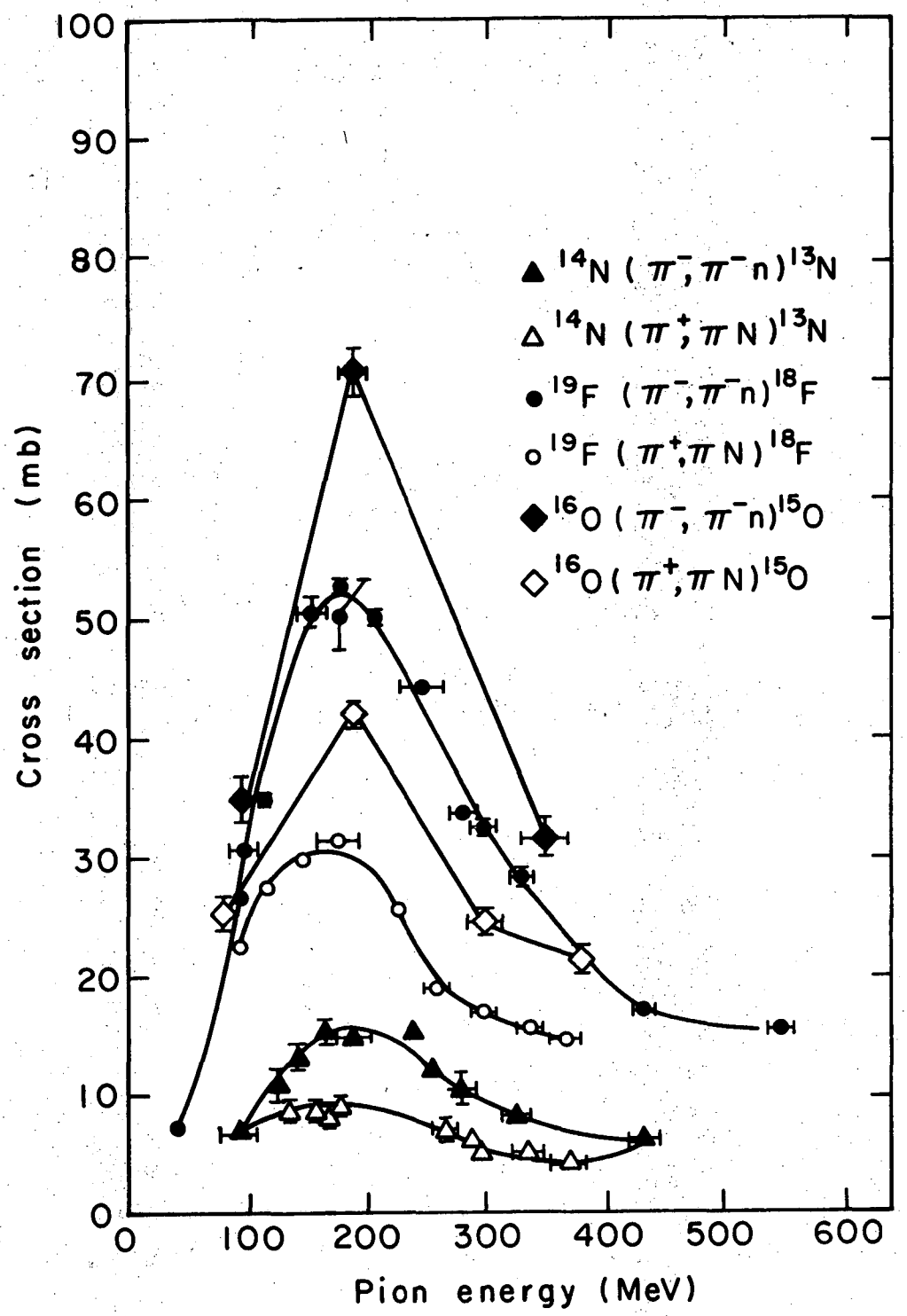

XBL755-2869

Fig. 4-1. Excitation functions for $(\pi^{\pm},\pi N)$ reactions.

functions, shown in Fig. 4-2. The following information is yielded as a result: (1) The universal π^- curve shows that the $(\pi^-,\pi^- n)$ excitation functions for ^{12}C, ^{14}N, ^{16}O, and ^{19}F have the same shape, width (250±20 MeV FWHM) and peak maximum at 180-190 MeV (2) The universal π^+ curve shows that the $(\pi^+,\pi N)$ excitation functions for ^{12}C, ^{14}N, ^{16}O, and ^{19}F have the same shape, width (also 250 ± 20 MeV FWHM) and peak maximum at about 180 MeV (3) The $(\pi,\pi N)$ excitation functions are considerably broader that the free-particle pion-nucleon resonances, which are about 140 ± 10 MeV (4) Cross sections for the $(\pi^-,\pi^- n)$ reactions on ^{14}N, ^{16}O, and ^{19}F relative to $(\pi^-,\pi^- n)$ cross sections for ^{12}C are respectively, 0.23 ± 0.02, 1.01 ± 0.06, and 0.75 ± 0.04 (5) Cross sections for $(\pi^+,\pi N)$ reactions on ^{14}N, ^{16}O, ^{19}F relative to $(\pi^+,\pi N)$ cross sections for ^{12}C are respectively, 0.21 ± 0.03, 0.97 ± 0.04, and 0.68 ± 0.03 (6) From (4) and (5) above, the relative $(\pi^-,\pi^- n)$ and $(\pi^+,\pi N)$ cross section magnitudes are very similar.

In emphasizing trends for the more complex reactions, the text will refer only to the dominant reaction occuring in the target (see Section 4.2.5 of Part II of this thesis). For these more complex spallation reactions, it is seen that (1) The $^{14}N(\pi^+,X)$ ^{11}C cross sections are somewhat larger than the $^{14}N(\pi^-,X)$ ^{11}C cross sections above 225 MeV, and thereafter, the excitation functions essentially coincide. This difference in the excitation functions would be reduced slightly after corrections for the contributing $^{11}B(\pi^+,\pi^0)$ ^{11}C reaction. (2) The $^{16}O(\pi^+,X)$ ^{11}C cross sections are slightly larger than the $^{16}O(\pi^-,X)$ ^{11}C cross sections, while the $^{16}O(\pi^\pm,X)$ ^{13}N excitation functions have nearly equal magnitudes. (3) The $^{19}F(\pi^+,X)$ ^{11}C cross sections are larger than the

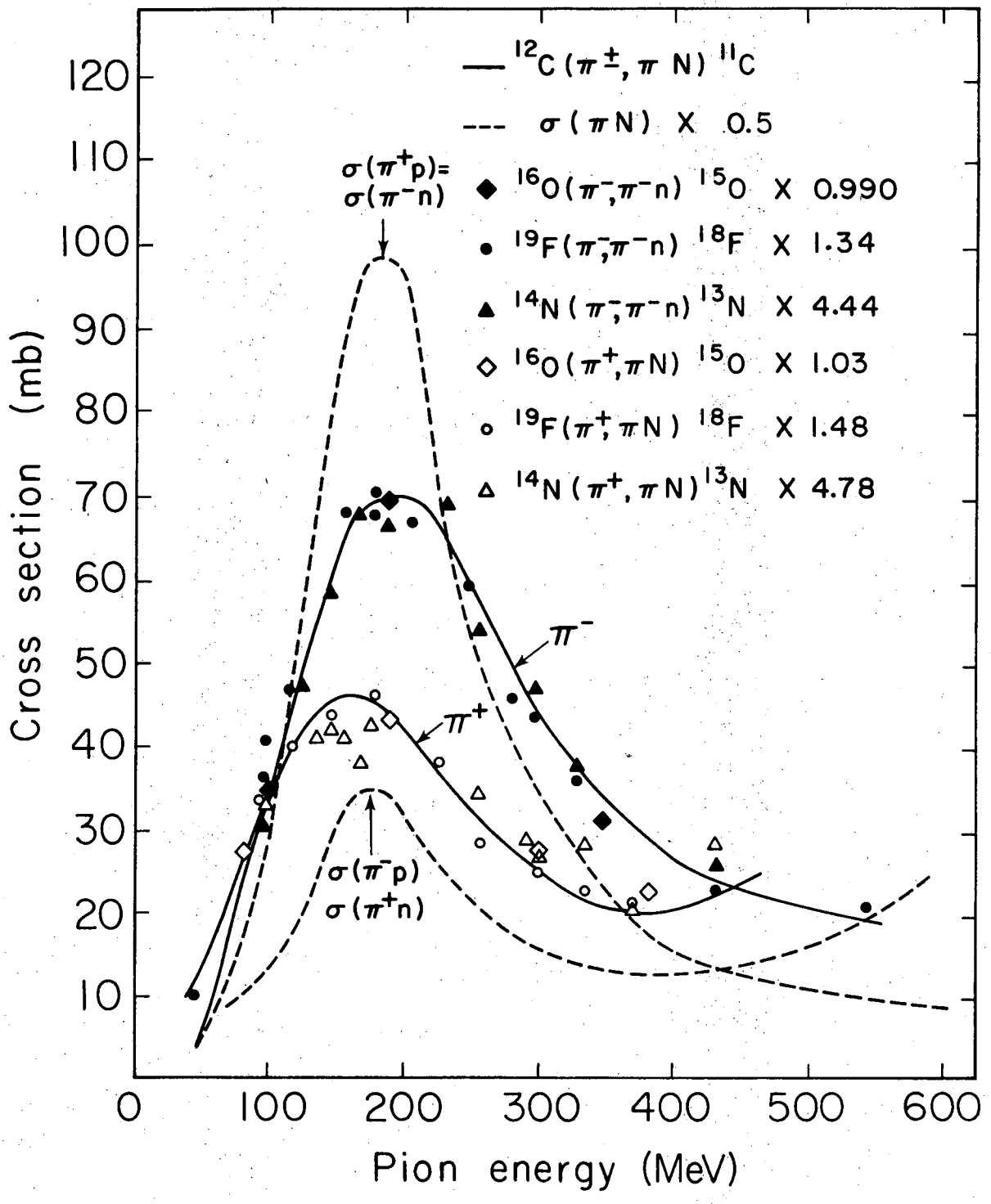

XBL 755-2865

Fig. 4-2. Comparison of experimental excitation functions. The numbers given are factors by which an individual excitation function curve must be multiplied to fall on the "normal" $^{12}C(\pi,\pi N)$ ^{11}C excitation function curve.(88) The free-particle cross sections, reduced by a factor of 0.5, are also shown in the plot for comparison.(58).

$^{19}F(\pi^-,X)\ ^{11}C$ cross sections below about 250 MeV, and are approximately equal, as in the case of the ^{14}N reactions, at higher energies. It should be emphasized that the errors on these ^{19}F excitation functions are necessarily large (about 25%) due to the required corrections and that definitive comparisons should be attempted with caution (4) All the complex reactions exhibit a broad peak near 180 MeV with perhaps some downshift in peak maximum to lower energies for the (π^+,X) excitation functions, particularly for ^{14}N and ^{19}F.

4.1.1 $(\pi,\pi N)$ Cross Section Magnitudes

As mentioned in the previous section, striking differences in $(\pi,\pi N)$ cross section magnitudes were observed. Several explanations similar to those discussed in Part I are considered here.

4.1.1 A Stability of the Residual Nucleus

A clue to the stability of the residual post-knockout nucleus may be found by considering the first excited, particle unbound energy level in the system. Table 4-1 summarizes this correlation between nuclear stabilities and relative cross section magnitudes. For the cases studied in this work, it is seen that the cross section magnitudes may be satisfactorily understood in terms of this phenomenon. Further experimental examples would be required to either establish more firmly or refute this consideration.

4.1.1 B Number of Bound Levels in the Residual Nucleus

The number of bound levels for each observed nuclide is given in Table 4-2. The low $^{14}N(\pi,\pi N)\ ^{13}N$ cross sections appear to be consistent with the fact that all excited levels of ^{13}N are unbound, and that consequently, only the ground state of ^{13}N may be formed. The other cross

Table 4-1. A correlation of residual nucleus stability to cross section magnitude

Nucleus	First particle unbound level (MeV)	Particle emitted	Relative cross section
^{11}C	8.4[a]	α	1
^{13}N	2.4[b]	p	0.2
^{15}O	7.6[b]	p	1
^{18}F	5.4[c]	α	0.7

[a]Reference 98.
[b]Reference 35
[c]Reference 99

Table 4-2. A comparison of $(\pi,\pi N)$ cross section magnitudes to the number of residual bound levels

Reaction	Approximate relative cross section (to $^{12}C \xrightarrow{\pi} {}^{11}C$	Number of bound excited levels
$^{12}C(\pi^{\pm},\pi N)\ ^{11}C$	1	10-12 [a]
$^{14}N(\pi^{\pm},\pi N)\ ^{13}N$	0.2	1 [b]
$^{16}O(\pi^{\pm},\pi N)\ ^{15}O$	1	7 [b]
$^{19}F(\pi^{\pm},\pi N)\ ^{18}F$	0.7	20 [c]

[a] Reference 98
[b] Reference 35
[c] Reference 99

sections, however, do not clearly correlate with the number of residual bound levels.(35,98,99) For example, the $^{19}F(\pi^{\pm},\pi N)\ ^{18}F$ cross sections are approximately 70% of the $^{12}C(\pi^{\pm},\pi N)\ ^{11}C$ cross sections, even though ^{18}F has twice as many particle bound levels as ^{11}C. It is concluded, then, that the number of residual bound levels can only partly rationalize the relative $(\pi,\pi N)$ cross section magnitudes.

4.1.1 C Availability of Neutron Shells

Again, as in Part I, one may use the neutron shell availability theory of Benioff(42) for (p,pn) reactions to roughly estimate relative $(\pi,\pi N)$ cross section magnitudes in this work. The necessary assumptions made to perform the calculation were (1) The effective πN cross sections in ^{12}C, ^{14}N, ^{16}O, and ^{19}F are equal (2) The nuclear radius parameter r_0 was equal to 1.30 F, a figure consistent with the results from high energy electron scattering experiments(100) (3) The values of M_{nl}, the fractional availability, for $(\pi,\pi N)$ reactions are equal or at least proportional to M_{nl} for (p,pn) reactions.

Finally, the following neutron levels were considered available for a $(\pi,\pi N)$ reaction:

^{12}C $1p_{3/2}$ (4)

^{14}N $1p_{1/2}$ (1)

^{16}O $1p_{3/2}$ (4), $1p_{1/2}$ (2)

^{19}F $1d_{5/2}$ (2) .

From Eq. 4-2 in Section 4.1.2 D in Part I and the fractional availability charts in the Benioff paper, a calculation of $(\pi^{\pm},\pi N)$ cross sections for

^{14}N, ^{16}O, and ^{19}F relative to the $^{12}C(\pi^{\pm},\pi N)\ ^{11}C$ reactions yields $\sigma_{^{14}N}(^{13}N):\ \sigma_{^{16}O}(^{15}O):\ \sigma_{^{19}F}(^{18}F) = 0.24:\ 1.3:\ 0.64$ which is in good agreement, considering the rough nature of the calculation with the observed relative cross sections for π^-

$$\sigma_{^{14}N}(^{13}N):\ \sigma_{^{16}O}(^{15}O):\ \sigma_{^{19}F}(^{18}F) = 0.23:\ 1.0:\ 0.75$$

and for π^+

$$\sigma_{^{14}N}(^{13}N):\ \sigma_{^{16}O}(^{15}O):\ \sigma_{^{19}F}(^{18}F) = 0.21:\ 0.97:\ 0.68.$$

This agreement can be taken, then, as reinforcing the plausibility of shell structure effects on the magnitude of $(\pi,\pi N)$ reactions on the light targets studied in this work.

4.1.2 Widths of $(\pi^{\pm},\pi N)$ Excitation Functions

The observed FWHM of 250 ± 20 MeV for all the $(\pi^{\pm},\pi N)$ excitation functions is much broader than the free-particle πN FWHM of about 140 ± 10 MeV due to the Fermi motion of the struck neutron. This broadening has also been previously observed for the $^{12}C(\pi^+,\pi N)\ ^{11}C$ reactions through the (3,3) resonance.(61,88) Qualitatively, the momentum distribution of the struck nuetron will cause a smearing out of the resonance, because the center of mass energy will have a range of values at each incident pion energy.

In estimating the effect of the neutron momentum, it would be necessary to average the free-particle pion-nucleon cross section over the neutron momentum distribution. For a given pion kinetic energy T, this cross section is given by(65)

$$\langle\sigma\rangle = \frac{\int\int\sigma(E[T,p,\theta])\ P(p_N)\sin\theta\ dp_N\ d\theta}{\int\int P(p_N)\ \sin\theta\ dp_N\ d\theta} \qquad (4\text{-}1)$$

where $P(p_N)$ is the distribution of struck neutron momenta p_N, θ is the angle between the struck neutron momentum vector and the beam direction, and $\sigma(E\,[T,p,\theta])$ is the πN cross section at a center of mass energy E corresponding to a given T, p, and θ. Normally, one could use a Gaussian momentum distribution of the form $P(p_N) \sim p_N^{\ell}\, e^{-p_N^2/p_0^2}$, where ℓ is the angular momentum number corresponding to the struck neutron shell, and p_0 a parameter characteristic of the momentum distribution.[44]

Conversely, a quantitative estimate of the average momentum of the struck neutron may be obtained from a simpler approach. Using the formula of Reeder[15] and by assuming an average incident pion momentum of 288 MeV/c (this corresponds to a pion with 180 MeV kinetic energy) one obtains $p_N \sim 180$ MeV/c, a value very consistent with the average momentum figures of $p_N \sim$ (160-170) MeV/c for 1p protons in light nuclei.[44] Thus, the $(\pi,\pi N)$ reaction may serve as a tool for measuring average "allowed" nucleon momentum.

4.1.3 $(\pi^{\pm},x)$ Cross Section Magnitudes

From this work, the $A(\pi^+,X)B$ excitation functions are larger in magnitude than the $A(\pi^-,X)B$ excitation functions until about 350 MeV. At this energy, the two curves are seen to cross and remain approximately equal thereafter. If it is assumed that the mechanisms of π^+ and π^- spallation reactions are identical (a discussion of these more complex mechanisms is given in Section 4.3), then it might be possible that the (π,x) cross section difference at lower pion energies may be sensitive to some aspect of compound nucleus formation and/or de-excitation following pion capture.

Considering, then, the various pion absorption reactions for the light targets in this work and the compound systems formed following the capture of the incident pion, one would have the following processes

1) $^{14}N \xrightarrow{\pi^+} [^{16}O]^* \longrightarrow {}^{11}C$

$^{14}N \xrightarrow{\pi^-} [^{14}C]^* \longrightarrow {}^{11}C$

2) $^{16}O \xrightarrow{\pi^+} [^{16}F]^* \longrightarrow {}^{11}C$

$\qquad\qquad\qquad\qquad\qquad\qquad\qquad\qquad\qquad\qquad \longrightarrow {}^{11}C$

$^{16}O \xrightarrow{\pi^-} [^{16}N]^* \longrightarrow {}^{13}N$

$\qquad\qquad\qquad\qquad\qquad\qquad\qquad\qquad\qquad\qquad \longrightarrow {}^{11}C$

3) $^{19}F \xrightarrow{\pi^+} [^{19}Ne]^* \longrightarrow {}^{11}C$

$^{19}F \xrightarrow{\pi^-} [^{19}O]^* \longrightarrow {}^{11}C$

where the bracketed nucleus denotes an excited compound intermediate. Two observations are derived from the above reactions; (i) All the products formed following nuclear de-excitation are neutron poor (ii) The π^+ capture reactions lead to intermediate compound nuclei that are neutron poor, like the final products, in contrast to the neutron rich compound nuclei formed following π^- capture. These facts may suggest that the formation of neutron poor nuclei following pion absorption is enhanced from neutron poor compound systems relative to neutron rich compound systems.

At higher energies (> 250 MeV), pion absorption should become less important compared to a pion scattering-cascade-evaporation scheme (again,

see Section 4.3). Assuming this particular mechanism to dominate at higher energies, and the fact that the total inelastic (reaction) cross sections for π^+ and π^- are equal for N = Z nuclei (by charge symmetry), one could infer that $\sigma(\pi^+,X) \approx \sigma(\pi^+,X)$ in the considered energy regime.

The above proposals appear to correlate reasonably, at least qualitatively, with the observed magnitude trend for complex pion induced reactions. More work on other target systems is needed.

4.1.4 Comparison to Previous Pion Studies

4.1.4 A $(\pi, \pi N)$ Reactions

Part of the purpose of this project was to check the activation cross sections and ratios of Chivers and co-workers.(71) Figure 4-3 illustrates comparisons between prior and present $(\pi,\pi N)$ cross sections for ^{14}N and ^{19}F. The $^{14}N \xrightarrow{\pi^\pm} {}^{13}N$ excitation functions from this work appear to be in generally good agreement with the measured cross sections from the work of Zaider et al.(76) and Karol et al.,(79), but are in serious disagreement with the cross sections of Chivers et al. at 180 MeV. The Chivers ^{13}N cross sections as seen from the figure are about 4-6 times the value for the ^{13}N cross sections from this work. The reason for this large difference is unclear. As mentioned earlier in the text, the low ^{13}N cross sections observed in this work are consistent with the instability of excited ^{13}N states with respect to proton emission. The $^{19}F(\pi^\pm,\pi N)^{18}F$ data of Hogstrom et al.(67) and Plendl et al.(66) are in serious disagreement not only with the magnitudes, but also with the general shape of the excitation functions from this work. The excitation functions of Plendl (66) and Hogstrom (67) appear to be too narrow and do not exhibit the expected

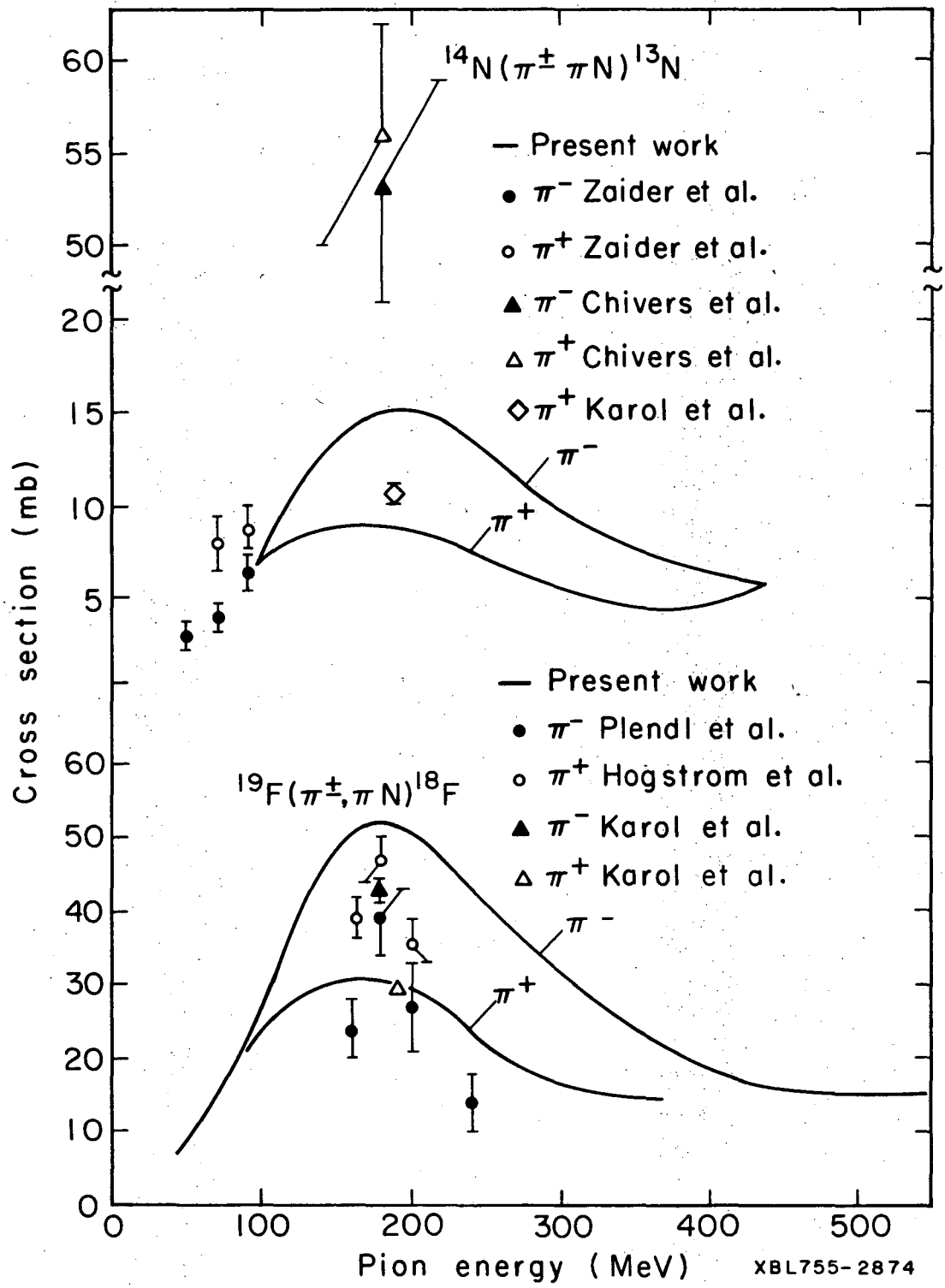

Fig. 4-3. Comparison of previous and present $(\pi^{\pm},\pi N)$ section measurements. Refences: Zaider et al., (76) Chivers et al., (71) Karol et al.,(79) Plendl et al.,(66) Hogstrom et al.,(67)

broadening of the free-particle πN curves by the Fermi motion of the struck nucleon. Generally, as discussed previously, the (π,πN) excitation function would be anticipated to be approximately 1.5 to 2 times the FWHM of the free-particle excitation function. This would imply a FWHM for the (π,πN) excitation function of 240 ± 30 MeV, a figure that correlates nicely with the observed widths from the present work.

Finally, the $^{16}O(\pi^{\pm},\pi N)^{15}O$ cross sections of Chivers et al.(71) at 180 MeV of 41 ± 3 mb for π^+ and 42 ± 4 mb for π^- are in good and poor agreement respectively with the corresponding cross sections from this work at 188 MeV of 41.9 ± 0.5 mb and 70.6 ± 2.1 mb.

The ratios R_{π^-/π^+}, discussed in the Introduction to Part II as important indicators of the (π,πN) reaction mechanism, are compared for past and present work in Table 4-3. At about 180-190 MeV, the ratio $R_{\pi^-/\pi}$ for all (π,πN) reactions in this work can be taken as 1.7 ± 0.2. This is in disagreement with Chivers et al.(71) result of 1.0 ± 0.1, in fair agreement with the ^{18}F ratio of 1.52 ± 0.05 from the work of Karol et al.(79) and in very good agreement with the ratios of 1.8 ± 0.4 and 1.7 ± 0.4 for (π,πN) reactions on ^{16}O measured by Lieb et al.(77) These measurements, however, are still at variance with the impulse approximation value of about 3 at 180 MeV. Close agreement is also observed between the ratio from this work $R_{\pi^-/\pi^+} = 1.7 \pm 0.2$ and the value of $R_{\pi^-/\pi^+} = 1.6 \pm 0.1$ for the $^{12}C(\pi^{\pm},\pi N)^{11}C$ reactions near 180 MeV.(88)

A broader comparison of the ratios from this work to those for the ^{12}C data as a function of incident pion energy is shown in Fig. 4-4. From this diagram, it is seen that the ratio R_{π^-/π^+} for (π,πN) reaction on ^{12}C, ^{14}N, ^{16}O, and ^{19}F have similar energy dependences and nearly equal

Table 4-3. Comparison of π^-/π^+ cross section ratios for nucleons knockout

Reaction	Pion energy (MeV)	R_{π^-/π^+}	Reference
$^{12}C(\pi,\pi N)\ ^{11}C$	180	0.97±0.09	71
	180	1.55±0.10	88
$^{14}N(\pi,\pi N)\ ^{13}N$	180	0.95±0.09	71
	188±15	1.68±0.18[a]	present work
$^{16}O(\pi,\pi N)\ ^{15}O$	180	1.02±0.09	71
	188± 9	1.68±0.05	present work
	215	1.8 ±0.4 [b]	77
	180	1.7 ±0.4 [b]	78
$^{19}F(\pi,\pi N)\ ^{18}F$	190	1.52±0.05	79
	178± 2	1.68±0.03	present work
	184	1.11±0.14	80

[a]The π^+ cross section used to calculate this ratio was interpolated from the excitation function.

[b]Ratio measured here is for $\pi^\pm + {}^{16}O \rightarrow {}^{15}O,\ {}^{15}N$ 6 MeV $3/2^-$ states.

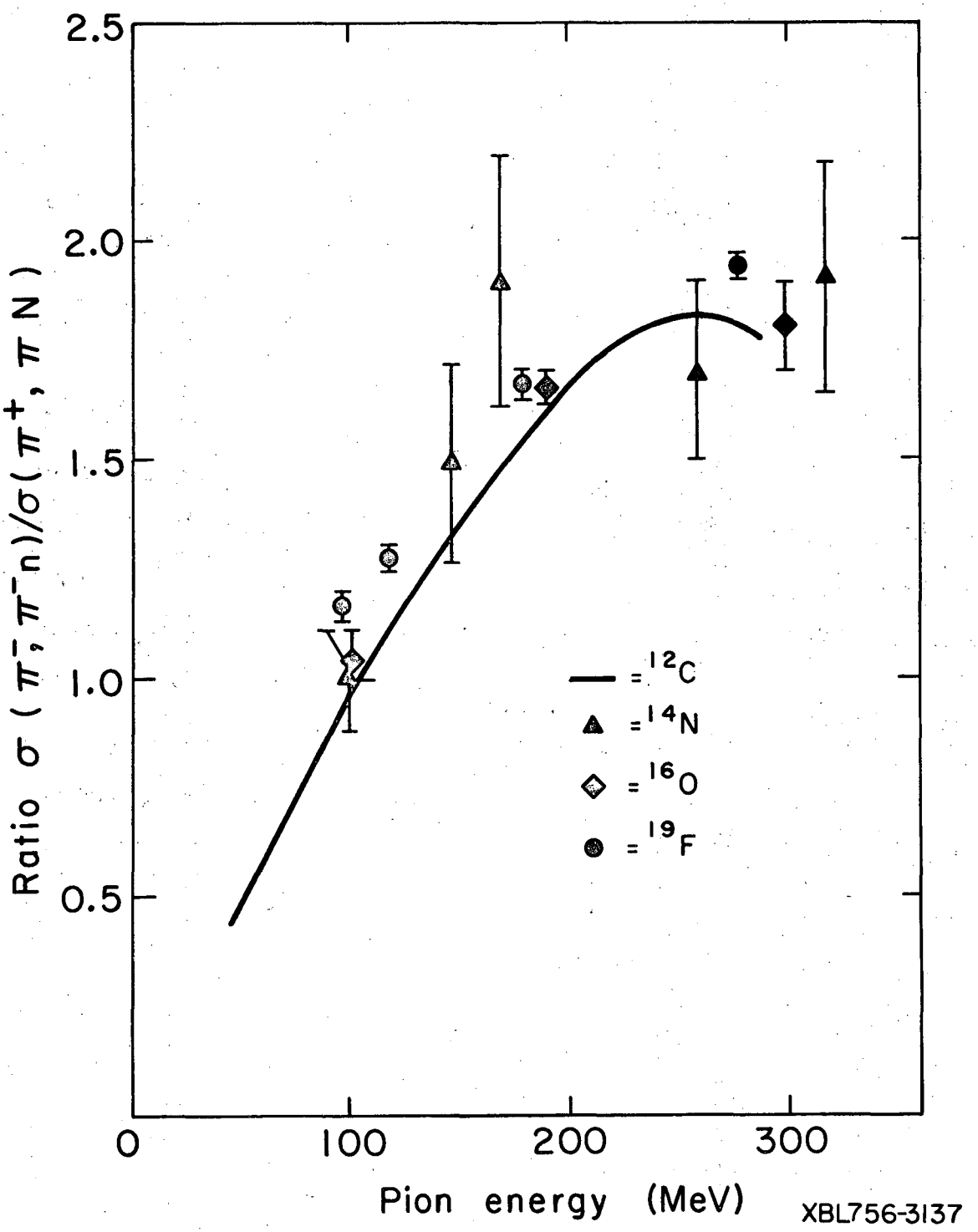

Fig. 4-4. Experimental ratios R_{π^-/π^+} for ^{12}C, ^{14}N, ^{16}O, and ^{19}F.

magnitudes. Such a comparison implies that the mechanism of $(\pi,\pi N)$ reactions on these nuclei should be also similar.

4.1.4 B (π,X) Reactions

Thus far, there exists no cross section data in the literature for complex pion reactions on the nuclei studied as targets in this work. Furthermore, prior excitation function studies for high energy pions (> 100 MeV) on other nuclei are few. The excitation functions for the $^{27}Al(\pi^-,X)^{11}C$, $^{18}F(62)$ and $^{40}Ar(\pi^-,\pi^-\ 2p)\ ^{38}S$ (65) above 450 MeV pion energy display no structure that could be related to higher energy pion-nucleon resonances. The preliminary measurements performed by the LASL pion monitoring group, however, of the $^{27}Al(\pi^{\pm},X)\ ^{18}F$ excitation functions[101] illustrate very broad peaks in the region of the (3,3) resonance, as found for the (π,X) reactions from this work. In addition, the $^{27}Al(\pi^+,X)\ ^{18}F$ excitation function is slightly larger in magnitude than the $^{27}Al(\pi^-,X)\ ^{18}F$ excitation function until about 300 MeV, at which point the curves cross and become approximately equal thereafter. The low energy 65 MeV $\pi^{\pm}$ spallation study on a Cu target[102] also shows generally larger cross sections for π^+ than π^-. These previously observed magnitude trends correlate well with those observed for the (π,X) reactions in the present study. Additional work on the spallation of heavier nuclei through the (3,3) resonance would be desirable.

4.1.5 Comparison to Proton-Induced Reactions

4.1.5 A (p,pn) Reactions

Since (a,aN) reactions are expected to occur by similar mechanisms, it would be interesting to compare cross sections for the well-studied (p,pn) reaction to those for the $(\pi^{\pm},\pi N)$ reaction. Such a comparison would

be especially valid for π^+, which like the proton, is a positively charged projectile that can change its identity through a charge exchange step.

A comparison of cross section magnitudes is summarized in Table 4-4. In synthesizing this table, two approaches were used. First, all cross sections were determined relative to the $^{12}C \longrightarrow {}^{11}C$ reaction for convenience of comparison. Second, since (p,pn) excitation functions have similar shapes, as do the (π,πN) reactions, it was possible to find only one "scaling" factor (which is actually the relative cross section value) for each (p,pn) target. This procedure is entirely analogous to the normalization performed earlier for the comparison of (π,πN) excitation function shapes. The method is attractive because it allows a comparison of cross section magnitudes to be made over a very broad energy range.

As Table 4-4 shows, striking similarities between relative (p,pn) and (π,πN) cross section magnitudes are seen. Several statements may be made from these results (1) The observed low cross sections for the $^{14}N(\pi^{\pm},\pi N)\ ^{13}N$ reactions are consistent with the experimental (p,pn) results (2) The (p,pn) and (π,πN) reactions may proceed by very similar mechanisms. The subject of (π,πN) mechanisms, a major concern of this thesis, will be covered later in the text.

4.1.5 B (p,X) Reactions

A comparison between high energy (p,X) and (π,X) reactions is somewhat more difficult than that made for ($\pi^{\pm}$,πN) and (p,pn) reactions for several reasons. First, the ($\pi^{\pm}$,X) cross sections do not "parallel" the $^{12}C(\pi^{\pm},\pi N)\ ^{11}C$ excitation functions as do the ($\pi^{\pm}$,πN) excitation reactions. Therefore, a single relative cross section for the entire excitation function energy region cannot be calculated. Secondly, the cross section data for high

Table 4-4. Comparison between $(\pi,\pi N)$ and (p,pn) cross sections, relative to the $^{12}C \rightarrow {}^{11}C$ reactions

Reaction		Relative Cross Section $\sigma(\pi^-,\pi^-n)$	$\sigma(\pi^+,\pi N)$	$\sigma(p,pn)$[a]
^{12}C	^{11}C	1.0	1.0	1.0
^{14}N	^{13}N	0.23±0.02	0.21±0.03	0.16±0.03[b]
^{16}O	^{15}O	1.01±0.06	0.97±0.04	1.31±0.38[c]
^{19}F	^{18}F	0.75±0.04	0.68±0.03	0.65±0.08[d]

[a]Cross sections obtained from Reference 38

[b]Derived from cross sections in Reference 38 above 200 MeV

[c]Derived from cross sections in Reference 38 above 400 MeV

[d]Derived from cross sections in Reference 38 above 460 MeV

energy (p, X) reactions on light nuclei in the lower GeV energy region ($\lesssim$0.6 GeV) are scarce and generally, only fair at best in accuracy.

Still, a limited but interesting comparison was made. Experimental and theoretical (Monte Carlo) studies have indicated that the yield distribution from pion-induced reactions should be about equal to those for protons with kinetic energies equal to the total energy (kinetic + rest) of the pion. Thus, Table 4-5 gives a comparison of cross sections for 260 MeV pions and 400 MeV protons on ^{14}N, ^{16}O, and ^{19}F. The similarities in cross section magnitudes between pions and protons is striking and tends to support the plausibility of the comparative approach. Comparisons at higher and lower energies could not be made due to a lack of pion and/or proton cross section data at the desired energies.

4.2 Mechanism of the $(\pi,\pi N)$ Reaction

Originally thought to occur by a CKO mechanism, the $(\pi,\pi N)$ reaction had been a puzzle until recently with regard to its exact reaction pathway. The theories (82-87) following the work of Chivers, (71) although successful in reducing the ratio R_{π^-/π^+} to a value less than the impulse approximation prediction of 3 at 180 MeV, could not satisfactorily explain the ratio $R_{\pi^-/\pi^+} = 1 \pm 0.1$. The semi-classical nucleon charge-exchange-exchange model of Sternheim and Silbar (89) applied to the $^{12}C(\pi^{\pm},\pi N)\ ^{11}C$ excitation functions measured by Dropesky et al.(88) has provided by far, the most satisfactory interpretation of the $(\pi,\pi N)$ mechanism.

The purpose of the immediate sections will be to reapply several prior theories for $(\pi,\pi N)$ reactions to the present work and to present comparisons of the measured cross section ratios to those calculated by the HEVI-DFF code, described in Part I, and by the NCE model of Sternheim and Silbar.

Table 4-5. A comparison between cross sections for complex pion and proton reactions on light elements

Reaction	Cross Sections (mb) 260 MeV π^+[a]	260 MeV π^-[a]	400 MeV p
$^{14}N \rightarrow {}^{11}C$	17.8±1.8	19.5±2.0	19.8±2.0[b,c]
$^{16}O \rightarrow {}^{11}C$	17.2±1.8	14.4±1.4	8.4±0.8[c]
$^{16}O \rightarrow {}^{13}N$	4.2±1.0	5.5±1.4	6.5±0.7[c]
$^{19}F \rightarrow {}^{11}C$	9.8±2.5	8.4±2.1	11.0±2.3[b,c]

[a]The cross sections at this energy were interpolated from the appropriate excitation function and assigned errors consistent with those observed experimentally.

[b]Reference 103; cross section adjusted to $\sigma_{^{27}Al}(^{24}Na) = 10.5$ mb

[c]Reference 104; cross section adjusted to $\sigma_{^{12}C}(^{11}C) = 32.3$ mb

4.2.1 Previous Theoretical Treatments

4.2.1 A Final State Interactions and Compound Nucleus Contributions

The method developed by Robson (86) for explaining the variance of the R_{π^-/π^+} ratios with the simple impulse approximation values is based on a treatment of the final state interaction of the outgoing nucleon with the residual nucleus. By choosing an isospin basis, Robson derives a formula for the cross section ratio for N = Z nuclei given by

$$R_{\pi^-/\pi^+} = \frac{5 + 4\chi}{7 - 4\chi} \qquad (4\text{-}2)$$

where the variable χ indicates the degree of coherence between the final nuclear states of different isospin, and in this approach, is adjusted to fit the available data. For example, for $\chi = 1$, $R_{\pi^-/\pi^+} = 3$, which implies a pure impulse approximation (CKO) mechanism. Thus, the value of χ should yield some insight into the $(\pi,\pi N)$ reaction mechanism.

Using the measured ratio $R_{\pi^-/\pi^+} = 1.7 \pm 0.2$ from this work at 180 MeV, one obtains from Eq. (4-2) that $\chi = 0.64 \pm 0.14$, a figure that implies some contribution from the ISE and/or CESE mechanism and a larger direct (CKO) contribution to the $(\pi,\pi N)$ reaction.

In the same spirit for ^{19}F, one uses the expression for $N \neq Z$ to obtain

$$R_{\pi^-/\pi^+} = \frac{9T^2}{3\,T^2-(1-\chi)(2T-1)} = \frac{9}{3} = 3 \qquad (4\text{-}3)$$

the impulse approximation ratio, which is in severe disagreement with the experimental value of $R_{\pi^-/\pi^+} = 1.68 \pm 0.03$. Equation (4-5) will always yield the value of 3 at 180 MeV for any $T = \frac{1}{2}$ nucleus (independent of a value for χ), which can be considered qualitatively surprising. Thus, the measured ratio for the $^{19}F(\pi^{\pm},\pi N)\ ^{18}F$ reactions partially refute the

Robson theory, although $(\pi,\pi N)$ mechanisms for N = Z nuclei appear to be reasonably explained.

4.2.1 B Enhancement of Isospin States

In an attempt to understand the Chivers results,(71) Seki (83) examined the $(\pi,\pi N)$ reaction from the viewpoint of isospin invariance. In his theory, various reaction amplitudes were expressed using the isospins of two particles in the three particle final states. Then, for any enhancement of a particular isospin state of the two particles, the ratio of cross sections could be calculated.

This may be briefly outlined. One begins with the final states from a $(\pi,\pi N)$ reaction on an N = Z target nucleus. It would be possible to have the following isospin possibilities

$$\begin{aligned} \vec{T}_{\pi} &= 1 \text{ (pion)} \\ \vec{T}_{N} &= \tfrac{1}{2} \text{ (nucleon)} \\ \vec{T}_{C} &= \tfrac{1}{2} \text{ (residual nucleus).} \end{aligned} \tag{4-4}$$

The initial state, however, has the incident pion with $\vec{T} = 1$, and an N = Z target nucleus with $\vec{T} = 0$. Thus, the total isospin must be $\vec{T}_{tot} = 1$. Since isospin is conserved

$$\vec{T}_{tot} = \vec{T} + \vec{T}_{N} + T_{C} \tag{4-5}$$

and when considering that the pion-nucleon coupled system $(\vec{T} + \vec{T}_{N}) = \tfrac{1}{2}$ or 3/2, one has that $\vec{T}_{C} = \tfrac{1}{2}$, 3/2, or 5/2.

The three couplings that are relevant would be

1) (πN) Residual Nucleus
2) π(N-Residual Nucleus) (4-6)
3) N(π-Residual Nucleus)

where the parentheses imply that the isospins for the particles within are added together and that this result is added to the remaining isospin number, etc.

The amplitudes for the three possible pion-nucleon scattering reactions (see Eq. (1-2)) are then written using appropriate Clebsch-Gordan coefficients, and the ratio of $(\pi,\pi N)$ cross sections is then formulated assuming an enhancement in a particular isospin state of two particles in the final state. These details are described elsewhere.(83)

By using the table in the paper by Seki, one notes that a value of $R_{\pi^-/\pi^+} = 1.5$ occurs for the (Neutron-Residual Nucleus) coupling in a T = 1 isospin state. Such a possibility is consistent with the measured value $R_{\pi^-/\pi^+} = 1.7 \pm 0.2$ at about 180 MeV for ^{14}N and ^{16}O target nuclei in this work.

4.2.1 C Nucleon Charge-Exchange (NCE)

The NCE model was first developed formally by Hewson (87) to account for the discrepancies observed first by Chivers (71) between the experimental and impulse approximation R_{π^-/π^+} ratios. Although Hewson did neglect the process of pion charge-exchange prior to nucleon charge-exchange, as pointed out in the Sternheim and Silbar paper,(89) it would still be interesting to compare the results of his calculation to this work.

Two of the final results in the Hewson paper are consistent with the data from this work for the following values for W_1, the imaginary part of the optical potential (1) $W_1 = 165$ MeV, which resulted in a calculated ratio of $R_{\pi^-/\pi^+} = 1.6$ (2) $W_1 = 120$ MeV, which yields $R_{\pi^-/\pi^+} = 1.90$. Both of these theoretical ratios can be considered to be in good agreement with the measured $R_{\pi^-/\pi^+} = 1.7 \pm 0.2$ at 180 MeV. The effect of ignoring

the (π^+, π° N) reaction channel, as discussed above, was not quantitatively estimated, but it should give calculated cross section ratios that are high.

The semi-classical NCE model of Sternheim and Silbar, conceptually similar to the above model by Hewson, is applied to the present data and is discussed later in this thesis.

4.2.1 Summary

It has been found that prior theories formulated to explain the Chivers results appear to propose viable mechanisms for the (π,πN) reactions on the light nuclei ^{12}C, ^{14}N, ^{16}O when recent results are used. The one theory that could be applied to ^{19}F ($N \neq Z$) was in severe disagreement with the experimental ratio from this work.

4.2.2 Monte Carlo Calculations

The previously described HEVI-DFF code[55] used to calculated (p,2p) cross sections in Part I of this thesis was also used for this pion study in an attempt to correlate the magnitude and shape of the (π,πN) (and (π,X)) excitation functions to a particular reaction model (cascade-evaporation) and nuclear model (Fermi gas with step distribution density of nucleons). Again, a brief survey of the two programs in this code is given in Part I and further details concerning the programs is given elsewhere.(55)

4.2.2 A Computational Procedure

All conditions, assumptions, and basic philosophy that were followed for the calculations in Part I of the thesis also applied here, with the exception that the pion potential was changed to V_π = 0 MeV. Preliminary calculations of several $^{19}F(\pi^-,\pi^- n)\ ^{18}F$ cross sections around 180 MeV with

V_π = 25 MeV displayed a downshift of about 25-30 MeV in the maximum of the excitation function.(57) Qualitatively, the direction and magnitude of this shift is anticipated for a positive pion-nucleus potential. However, since all $(\pi^{\pm},\pi N)$ excitation functions from this work did not generally display this downshift, a potential of V_π = 0 was used instead.

For purposes of economy, only three cross sections were calculated for each excitation function, yielding a total of 18 theoretical $(\pi,\pi N)$ cross sections. The energies chosen were about 100, 190, and 400 MeV inorder to obtain an idea of the predicted energy dependence of the cross sections.

In addition to the absolute $(\pi,\pi N)$ cross section calculations, a supplemental subroutine named KNOCK was included with each program to determine the "knockout" $(\pi,\pi N)$ cross seciton. For these particular calculations, a knockout event was defined as one that produced a residual $(\pi,\pi N)$ cascade nucleus with less than the excitation energy needed to evaporate a particle (generally the least bound).

The DFF program was first run to obtain these maximum excitation energies, which were 10 MeV for ^{13}N (obviously too high; this point will be discussed later), 9 MeV for ^{15}O and 8 MeV for ^{18}F. The routine KNOCK then, would scan the cascade output and count knockout events, and calculate the knockout $(\pi,\pi N)$ cross section. It was hoped that such information would be useful in the interpretation of the $(\pi,\pi N)$ reaction mechanism.

One further adaptation was made for the $^{14}N(\pi,\pi N)\ ^{13}N$ reaction. The subroutine KNOCK was used to choose only those residual ^{13}N nuclei with excitation energy less than 2.37 MeV, the energy of the first excited level, which (as all the levels above it) is unbound.

4.2.2 B Comparison of Calculated and Experimental Results

The computed $(\pi,\pi N)$ cross sections are plotted in comparison to the data in Figs. 4-5 through 4-7. Also shown are the calculations of Bertini, (52) which differ from the present code by assuming that isobars formed within the nucleus immediately decay, and thus, do not interact as an integral unit.

Generally, one observes the following results in a comparison between calculations and experiment (1). The value of $V_\pi = 0$ is seen to be satisfactory in reproducing the energy at which the peak maximum occurs (2). The general energy dependence of the $(\pi,\pi N)$ reactions is correctly predicted (3). Fair agreement between calculated and experimental cross section magnitudes is seen for the $^{16}O(\pi^{\pm},\pi N)\ ^{15}O$ reactions (4). Good agreement between the $^{19}F(\pi^+,\pi N)\ ^{18}F$ experimental and calculated cross sections is observed at 100 and 180 MeV. The calculated $^{19}F(\pi^-,\pi^-n)\ ^{18}F$ cross sections, however, are overestimated by a factor of about two. (5). The calculation overestimates the ^{13}N cross sections, even when the instability of its excited states is taken into account (6). The computed $(\pi^+,\pi N)$ cross sections for ^{19}F and ^{14}N show no drop, but rather a flat energy dependence above 180 MeV.

The knockout cross sections, also plotted in Figs. 4-5 through 4-7, are generally a high fraction of the total $(\pi,\pi N)$ cross section; greater than 90% for (π^-,π^-n) reactions and greater than 80% for $(\pi^+,\pi N)$ reactions on the light elements, indicating that at most, 20% of the total $(\pi,\pi N)$ cross section may be ascribed to an ISE and/or CESE (in the case of π^+) mechanism. These percentages are in agreement with the estimate of 85% for a CKO mechanism deduced from an angular distribution study of the

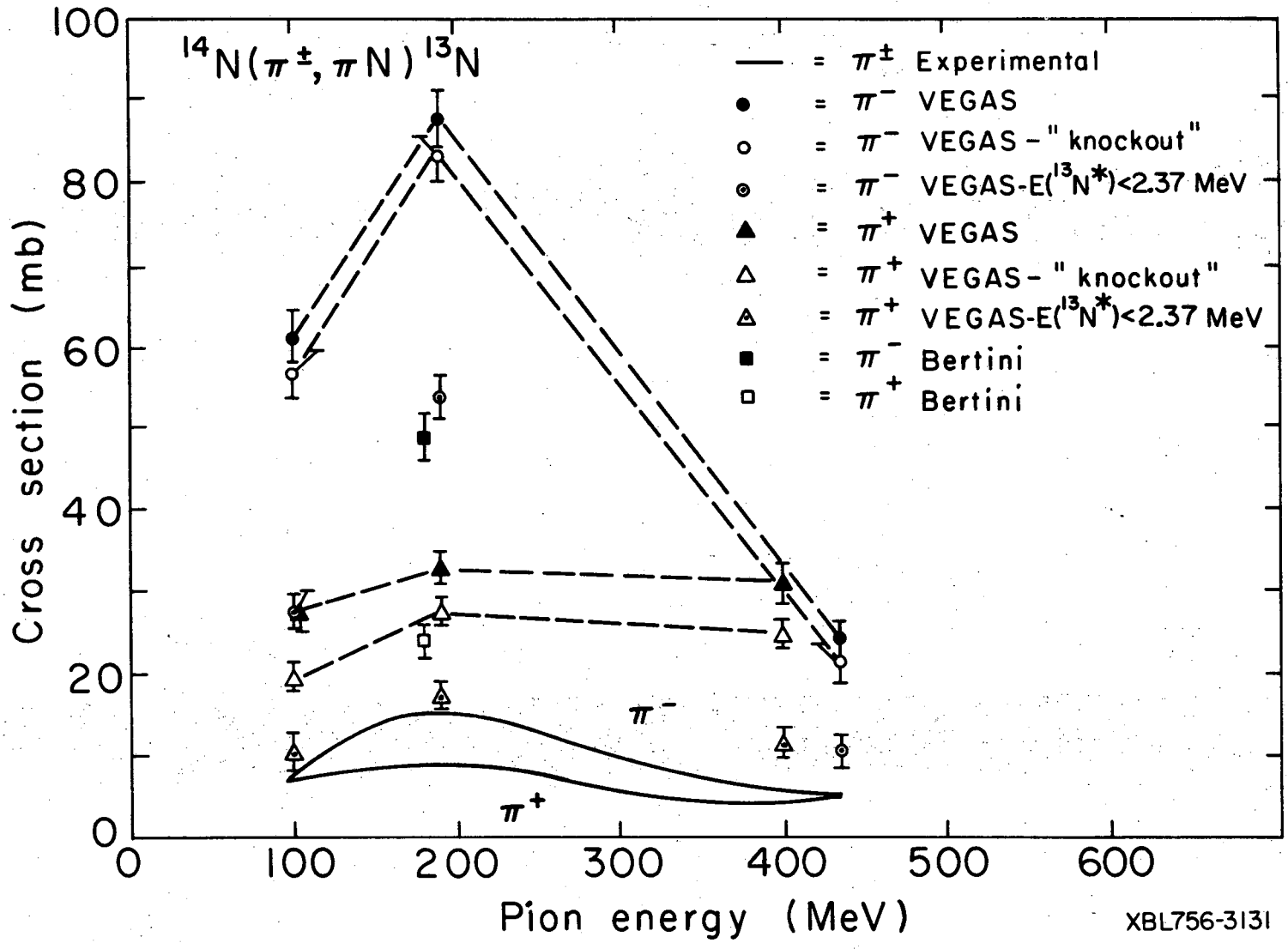

Fig. 4-5. Calculated and experimental $^{14}N(\pi^{\pm},\pi N)\ ^{13}N$ cross sections. The knockout cross sections were calculated assuming that the residual ^{13}N nucleus had less than 10 MeV of excitation energy. The case for which ^{13}N has less than the energy of its first (particle unbound) excited level is also shown. The results of Bertini (52) are shown as well.

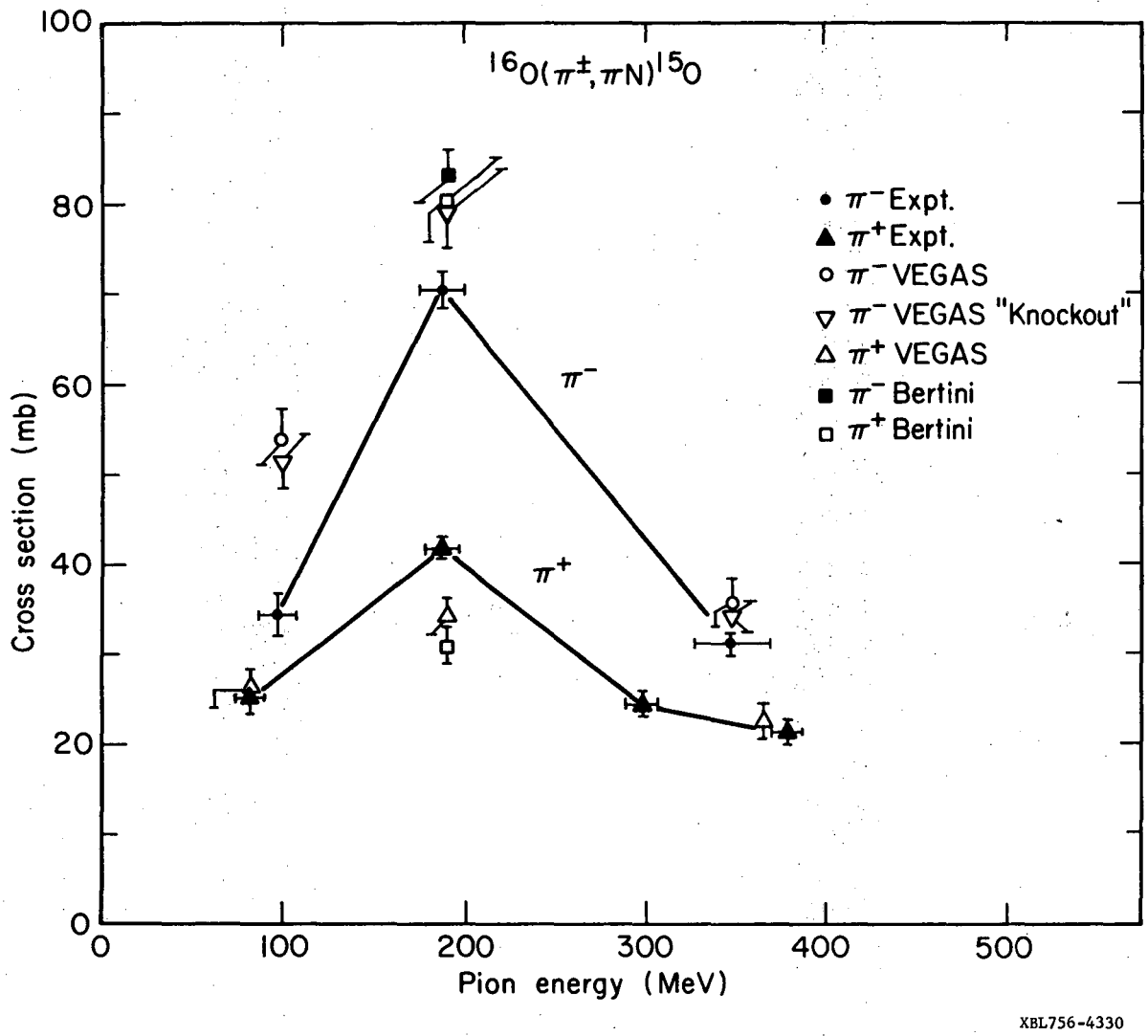

Fig. 4-6. Calculated and experimental $^{16}O(\pi^{\pm},\pi N)\ ^{15}O$ cross sections. The knockout cross sections were calculated assuming that the residual ^{15}O nucleus had less than 9 MeV of excitation energy. The results of Bertini (52) are also given.

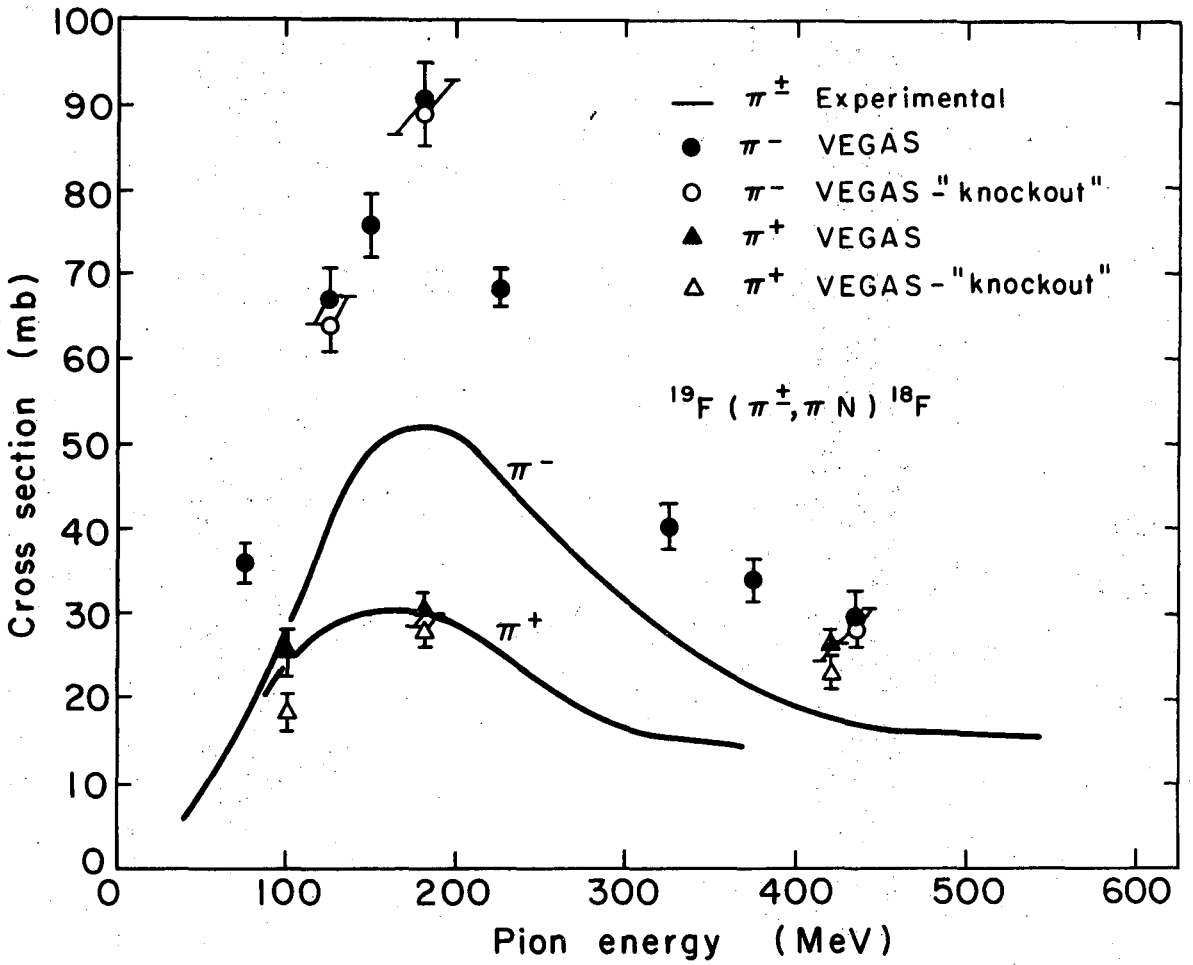

XBL756-3134

Fig. 4-7. Calculated and experimental $^{19}F(\pi^{\pm},\pi N)\ ^{18}F$ cross sections. The knockout cross sections were calculated assuming that the residual ^{18}F nucleus had less than 8 MeV of excitation energy.

$^{12}C(p,pn)\ ^{11}C$ reaction,(9) and imply that some form of low energy deposition knockout process, although not necessarily of the CKO variety, dominates the reaction mechanism.

It may be anticipated that although the calculated $(\pi,\pi N)$ cross sections generally disagree with the experimental values, the ratio of computed and measured cross sections ratios R_{π^-/π^+} may conform more closely. Therefore, this comparison among calculated, measured, and simple impulse approximation ratios is given in Table 4-6. The two most obvious trends are (1) The Monte Carlo results are always consistent with the simple impulse approximation predictions over the entire energy regime (2) The Monte Carlo and simple impulse approximation ratios are in disagreement with the experimental cross section ratios at the lowest two energies, but in excellent agreement at the highest energies (about 400 MeV) with the experiment. This last comparison may imply that a CKO process dominates the $(\pi,\pi N)$ mechanism at pion kinetic energies exceeding about 350 MeV, but that another mechanism contributes in the vicinity of the (3,3) resonance. It is noted here that the disagreement of the Monte Carlo results with the measured cross sections and ratios at lower energies is believed to be largely a consequence of the representative nuclear model, and not of the cascade-evaporation model of high energy nuclear reactions. Potential explanations for the observed discrepancies are given later in the the text.

4.2.2 C Contribution of Isobars to the $(\pi^{\pm},\pi N)$ Mechanism

It was speculated in Part I of this thesis that the mechanism of

Table 4-6. Comparison of measured and calculated cross section ratios

Nucleus	Pion Energy (MeV)	Measured	Calculated HEVI-DFF	Calculated Bertini[a]	Calculated Free-Particle[b]
^{14}N	100	0.99±0.12[c]	2.21±0.20		2.50±0.08
	190[d]	1.68±0.18[e]	2.74±0.23	2.04±0.21	2.85±0.10
	418[d]	0.98±0.17[e]	0.77±0.08		0.83±0.12
^{16}O	100	1.10±0.11[f]	2.06±0.20		2.50±0.08
	190	1.68±0.05[h]	2.36±0.20	2.68±0.20	2.85±0.10
	360[g]	1.53±0.15[h]	1.58±0.18		1.67±0.06
^{19}F	100	1.17±0.03[i]	2.60±0.25		2.50±0.08
	180	1.68±0.03[k]	2.95±0.23		2.95±0.10
	428[j]	1.11±0.11[k]	1.01±0.11		1.00±0.06

[a]Ratios are calculated at 180 MeV; Reference 52

[b]Reference 58

[c]Cross section ratio at 97±10 MeV

[d]Average of energies 400 MeV for π^+ and 435 MeV for π^-

[e]Interpolated from excitation function

[f]Interpolated ratio, assuming relative $^{16}O \xrightarrow{\pi} {}^{15}O$ cross section figures given in Section 4.1.; cross section ratio at 98±10 MeV

[g]Average of energies 370 MeV for π^+ and 350 MeV for π^-

[h]See f; cross section ratio at 360 MeV

[i]Cross section ratio at 96±3 MeV

[j]Average of energies 420 MeV for π^+ and 435 MeV for π^-

[k]Interpolated ratio, assuming relative $^{19}F \xrightarrow{\pi} {}^{18}F$ cross section figures given in Section 4.1.1.

$(\pi,\pi N)$ reactions could have a large contribution from isobar formation, i.e., a $(\pi^{\pm},I^{\pm})$ process, where I^{+} and I^{-} are respectively, positively (π° + p or π^{+} + n) and negatively (π^{-} + n) charged isobars. This process would involve an interaction of the incident pion with a single target nucleon and the subsequent prompt exit of the resultant isobar without disturbing the nucleus further (equivalent to a CKO process).

Table 4-7 summarizes the HEVI estimates of the contributions to the (π, N) reaction. In compiling the table, it was required that a $(\pi^{\pm},I^{\pm})$ event leave the residual nucleus with less excitation energy than necessary to evaporate the least bound particle (given by the DFF program). Generally, the isobar process constitutes between 7-10% of the $(\pi^{\pm}, N)$ cross section at the (3,3) resonance energy of about 180-190 MeV, and less than 2% at 100 and about 400 MeV.

Thus, the Monte Carlo cascade code HEVI, which takes isobar formation and interaction into account, has predicted that isobar processes may contribute to the $(\pi,\pi N)$ mechanism but, in general, would constitute a relatively small fraction of the total $(\pi,\pi N)$ cross section. These calculations are meant only as rough estimations of the isobar effect in simple pion-knockout reactions and, as evidenced by the previously mentioned discrepancies between calculated and measured results, should be viewed with some caution.

4.2.3 The Semi-Classical Nucleon Charge-Exchange (NCE) Model

An interesting NCE model, conceptually similar to that of Hewson,(87) has been advanced by Sternheim and Silbar(89) to explain the R_{π^-/π^+} ratios on ^{12}C as a function of incident pion energy. In this section, semi-classical NCE model is applied to the present work.

Table 4-7. Contributions to the $(\pi,\pi N)$ cross sections as calculated by the HEVI code

Nucleus	Pion Energy (MeV)	$\sigma(I^-)$ (mb)	% of total $\sigma(\pi^-,\pi^- n)$	$\sigma(I^+)$ (mb)	% of total $\sigma(\pi^+,\pi N)$
^{14}N	100	1.0±0.4	1.6±0.6	0.2±0.2	0.6±0.6
	190	8.4±1.2	9.5±1.4	3.0±0.7	9.5±2.3
	400 (π^+)				
	435 (π^-)	0	0	0	0
^{16}O	100	1.0 ±0.4	1.9±0.8	0.64±0.37	1.9±1.1
	190	7.4 ±1.1	9.1±1.4	2.4 ±0.6	6.8±1.8
	350 (π^-)				
	370 (π^+)	0.68±0.34	1.9±1.0	0.2 ±0.2	0.7±0.7
^{19}F	100	1.5±0.5	2.4±0.8	0.2 ±0.2	0.7±0.7
	180	7.9±1.2	8.7±1.4	1.6 ±0.5	5.2±1.7
	435 (π^-)				
	420 (π^+)	0	0	0.54±0.31	1.7±1.0

4.2.3 A Basic NCE Theory

The theory of Sternheim and Silbar(89) begins with the assumption, originally made by Hewson,(87) that the following single nucleon knockout reactions may occur in the nucleus:

Primary Interaction	Outgoing Particles	Relative Cross Section to give Observed Product
$\pi^- n$	$\pi^- n$ $\pi^- p$ (NCE)	$\sigma_1(1-X)$
$\pi^- p$	$\pi^\circ n$ $\pi^- p$ $\pi^- n$ (NCE)	$\sigma_2 X$
$\pi^+ p$	$\pi^+ p$ $\pi^+ n$ (NCE)	$\sigma_1 X$
$\pi^+ n$	$\pi^\circ p$ $\pi^+ n$ $\pi^+ p$ (NCE)	σ_3 $\sigma_2(1-X)$

where

$$\left.\begin{aligned} \sigma_1 &= \pi^- + n \rightarrow \pi^- + n = 9 \\ \sigma_2 &= \pi^+ + n \rightarrow \pi^+ + n = 1 \\ \sigma_3 &= \pi^+ + n \rightarrow \pi + p = 2 \end{aligned}\right\} \quad \text{Relative Units}$$

and X = Probability of a nucleon charge exchange (NCE) i.e., $p \rightarrow n$ or $n \rightarrow p$.

Then for production of a $(\pi,\pi N)$ product

$$R_{\pi^-/\pi^+} = \frac{\sigma_1 - X(\sigma_1-\sigma_2)}{\sigma_2+\sigma_3+X(\sigma_1-\sigma_2)} = \frac{9-8X}{3+8X} . \qquad (4-7)$$

Thus, one may see how an NCE process may enhance the π^+ cross section and deplete the π^- cross section. The model of Sternheim and Silbar has also included in the above possible reaction channels the $(\pi^+,\pi^\circ N)$ depletion reaction (charge-exchange of the pion followed by charge-exchange of the struck nucleon). Then, following the Sternheim and Silbar notation, the ratio of cross sections becomes

$$R_{\pi^-/\pi^+} = \frac{N\sigma(\pi^- n)(1-P) + Z\sigma(\pi^- p \to \pi^- p)P}{N\sigma(\pi^+ n)(1-P) + Z\sigma(\pi^+ p)P} \approx \frac{9-8P}{3+6P} \qquad (4\text{-}8)$$

where P = the probability of a nucleon charge exchange (analogous to the X of Hewson). The approximate form applies only at about 180 MeV for N=Z nuclei. Interesting limits of Eq.(4-8) at 180 MeV are for P=0, which yields the impulse approximation ratio of $R_{\pi^-/\pi^+} = 3$ and for P = ½, expected for large nuclei were an outgoing nucleon has no memory of its initial charge state, which gives $R_{\pi^-/\pi^+} = 5/6$.

The equation for P, as derived from the appropriate transport equations, is

$$P(T_\pi) = \tfrac{1}{2}\left(1 - \exp\left(-A\rho_0\,\sigma_{NCE}(T_\pi)\,D\,(T_\pi)\right)\right) \qquad (4\text{-}9)$$

where A = the target mass number, $\rho_0 = 3/(4\pi r_0^3)$, with r_0 the nuclear radius parameter (taken in the calculation from electron scattering data) $\sigma_{NCE}(T_\pi)$ = the nucleon charge exchange cross section as a function of pion energy and $D(T_\pi)$ = the average distance traveled by the initially struck nucleon as a function of pion energy.

As indicated above, both σ_{NCE} and D are indirect functions of the incident pion energy. As given by Sternheim and Silbar, these variables are

$$\sigma_{NCE} = \beta\, T_N^{-1.9} \qquad (4\text{-}10)$$

$$D = \frac{4}{3} R\text{-}\lambda \qquad (4\text{-}11)$$

where R is the nuclear radius, λ is the mean free path of the recoil nucleon, T_N is the kinetic energy of recoil nucleon, and β is a parameter fit to one experimental point, usually at or near 180 MeV, to circumvent problems in calculating the magnitude of the Pauli reduction factor.

4.2.3 B Results

The results for the ratios R_{π^-/π^+} on the light nuclei ^{14}N, ^{16}O, and ^{19}F from the above NCE model are shown in Fig. 4-8 in comparison to the ratio of free-particle πN cross sections (π^-/π^+) and to the HEVI-DFF ratios, derived from the previously calculated Monte Carlo ($\pi,\pi N$) cross sections. The Monte Carlo cascade-evaporation calculations of Bertini(52) are also shown. All of the NCE solid curves have been normalized to an experimental point near 180 MeV.(105)

The agreement of the NCE model with the present data, as it was for the ^{12}C data of Dropesky et al., is excellent, and lends credence to the NCE mechanism for the ($\pi,\pi N$) reaction in the vicinity of the (3,3) resonance. In reality, this excellent agreement is somewhat surprising in view of the fact that the NCE model encompasses an approach that is very similar to the Monte Carlo intranuclear cascade method, which as demonstrated previously and seen in Fig. 4-8, gives poor agreement with the experimental R_{π^-/π^+} ratios in the area of the (3,3) resonance.

In summary, the NCE model of Sternheim and Silbar has been successful in correlating the observed R_{π^-/π^+} ratios, which were at variance with the impulse approximation predictions. It would be interesting to obtain cross section data for ($\pi^\pm,\pi N$) reactions on heavier nuclei and for ($\pi^\pm,\pi p$) reactions in order to test this model more rigorously.

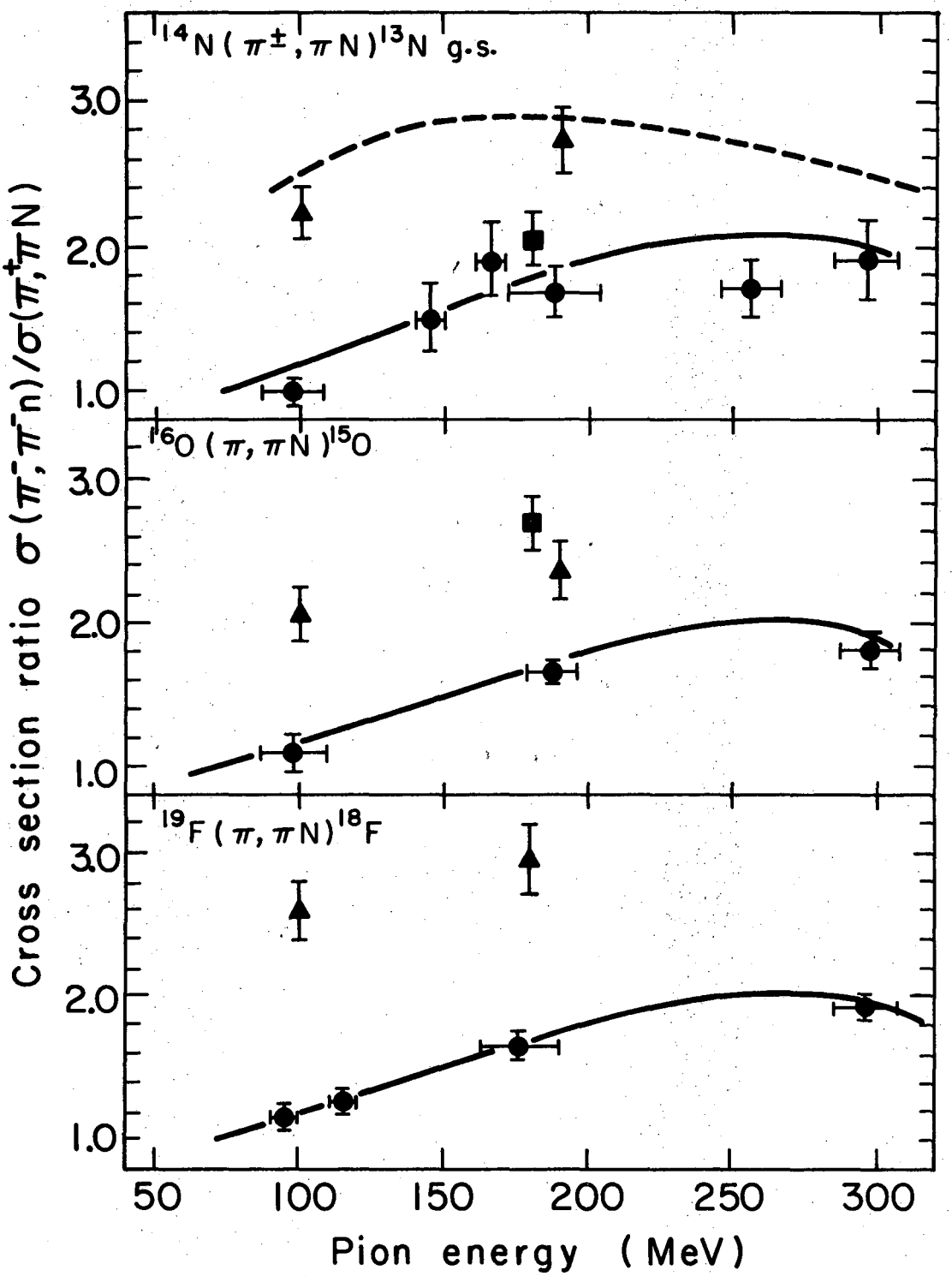

XBL756-3136

Fig. 4-8. Comparison of the NCE model to the measured ratios. The solid lines represent the theoretical NCE model, while the solid circles are experimental ratios for this work. Other representations are: dotted line - free-particle πN ratios; solid triangles - the HEVI-DFF calculated ratios; solid squares - calculations by Bertini.(52).

4.2.4 The NCE Model at High Energies

The NCE model of Sternheim and Silbar(89) reaches an interesting limit beyond the region of the (3,3) resonance, i.e., above about 350 MeV. An increasing pion energy T_π implies an increasing average nucleon recoil energy T_N, which is about equal to $T_\pi/3$, and thus, a dramatically decreasing charge exchange cross section σ_{EX}, which varies as $T_N^{-1.9}$. Thus, from Eq. 4-9, one would have that

$$\text{Limit } P = 0 \qquad (4\text{-}12)$$
$$T_\pi \rightarrow \text{large}$$

and that from Eq. 4-8 for N = Z nuclei,

$$\text{Limit } R_{\pi^-/\pi^+} = \sigma(\pi^- n)/\,\sigma(\pi^+ n) \qquad (4\text{-}13)$$
$$P \rightarrow 0$$

which is simply the ratio of free-particle cross sections or the impulse approximation prediction! Qualitatively stated, as the energy of the incident pion increases, the probability of the nucleon charge exchange process approaches 0, and one has that the ratio of $(\pi,\pi N)$ cross sections is very nearly equal to that of the corresponding free-particle pion-nucleon cross sections. This conclusion is consistent with the observed excellent agreement among measured, Monte Carlo, and simple impulse approximation ratios at energies above about 350 MeV (see Table 4-6). In reality, a small contribution would probably be expected from the NCE process even at these high incident pion energies, but it may be concluded that the mechanism of the $(\pi,\pi N)$ reaction above about 350 MeV would be almost entire CKO, with an additional small contribution on the order of 10% or less from the ISE and/or CESE mechanisms.

4.3 Mechanism of the $(\pi^{\pm},X)$ Reactions

4.3.1 Qualitative Discussion

Complex pion-induced reactions of the form $(\pi^{\pm},X)$, where X represents a number of nucleons removed from the nucleus, are be thought to occur by several mechanisms at high incident energies (i) An inelastic or charge-exchange scattering of the incident pion, followed by a cascade-evaporation sequence (ii) Capture of the incident pion by the nucleus (where its rest and kinetic energy are shared between two nucleons) and the subsequent de-excitation of the nucleus of the nucleus by the evaporation of particles (iii) Some complex combination of (i) and (ii), which would include capture of the initial pion after several collisions with nucleons.

Although $(\pi^{\pm},X)$ reaction mechanisms were not a major thrust of this project, it would still be interesting as well as relevent to speculate about these mechanisms at high energy from the limited results obtained in this work.

(1) Initial Pion-Nucleon Collisions are Important in Complex Pion-Reactions - The evidence for this conclusion is seen by the dominance of the (3,3) resonance in the excitation functions on the light nuclei in this work. Initially, it was thought that the peaks, which are clearly observed in $(\pi^{\pm},\pi N)$ excitation functions, would be washed out in the (π,X) excitation functions due to an "amnesia" effect in the final residual nucleus. Noting, however, that the inelastic (reaction) cross section for $\pi^- + {}^{12}C$ exhibits a broad peak near about 150 MeV,(97) one should anticipate that a (π,X) reaction, which constitutes a fraction of the total pion reaction cross section, will also display a broad peak in its

excitation function ascribable to the (3,3) resonance for light nuclei, such as ^{14}N, ^{16}O, and ^{19}F.

(2) Complex Pion-Reactions have Mechanisms Similar to those for Complex Proton Reactions - Qualitatively, this may be anticipated because of the similar overall energy deposition schemes for both protons and pions, i.e. both may undergo energy transfers from 0 MeV to the maximum energy possible, thereby leading to a broad distribution of final products. The observed similarities in the yields of nuclei from high energy protons and pions seen in the present work and others(57,103) indicate that the cascade-evaporation model, which has successfully correlated a large body of proton cross section data, is also applicable to the pion data. The one difference in the mechanism for energy transfer is that a pion may be captured by the nucleus and absorbed between two nucleons, which share its total energy. This absorption process has been shown to be the mechanism for pion interactions with nuclei between 0 to 60 MeV.(106) Pion absorption, however, may be a small contribution in comparison to a scattering-cascade-evaporation mechanism at the high energies considered in this work. At the same time, its contribution to the reaction mechanism should not be neglected. As a function of energy, the $\pi^+ + d \rightarrow p + p$ reaction rises to a maximum of about 10 mb at 180 MeV and falls rapidly, where at 300 MeV it has a cross section of about 2 mb.(107) Pion absorption has also been shown to be an important process in the LEVI-DFF calculations of Harp et al.,(54) particularly for the production of nuclei far removed from the initial target.

In view of the above considerations, one may anticipate that complex pion reactions proceed according to the cascade evaporation scheme model

applied often for protons, with some small but significant contribution from pion absorption on two nucleons.

4.3.2 Monte Carlo Calculations

A comparison of the measured ($\pi^{\pm}$,X) excitation functions to cross sections calculated at three pion energies by the HEVI-DFF code, described in Section 4.2.2 of Part II, is displayed in Fig. 4-9. The observations may be noted (1) Agreement between experimental and calculated cross section magnitudes in all cases is poor. The cross sections for production of ^{11}C from ^{19}F and ^{14}N are much lower than the experimental values. The calculation is seen, however, to overestimate the ^{13}N cross sections. (2) The influence of the (3,3) resonance is correctly predicted in the excitation functions (3) Cross sections for π^+ for a given target and product appear to be higher than the corresponding π^- cross sections at energies less than 180 MeV. At higher energies, the cross sections for the π^+ and π^- reactions become more equal. These calculated trends are consistent in general with the experimental excitation functions.

Thus, the Monte Carlo code appears to have reasonable success at predicting the general energy dependence of pion reactions but gives poor agreement with cross section magnitude comparison in this work. The latter is particularly disturbing in view of the previous successful correlation of Cu spallation data with this same code.(103) Potential reasons for discrepancies between the Monte Carlo calculations and experiment are considered subsequently.

4.4 Discrepancy between Monte Carlo and Experimental Results

The agreement of the NCE model and the severe disagreement of the Monte Carlo results with the data in the vicinity of the (3,3) resonance

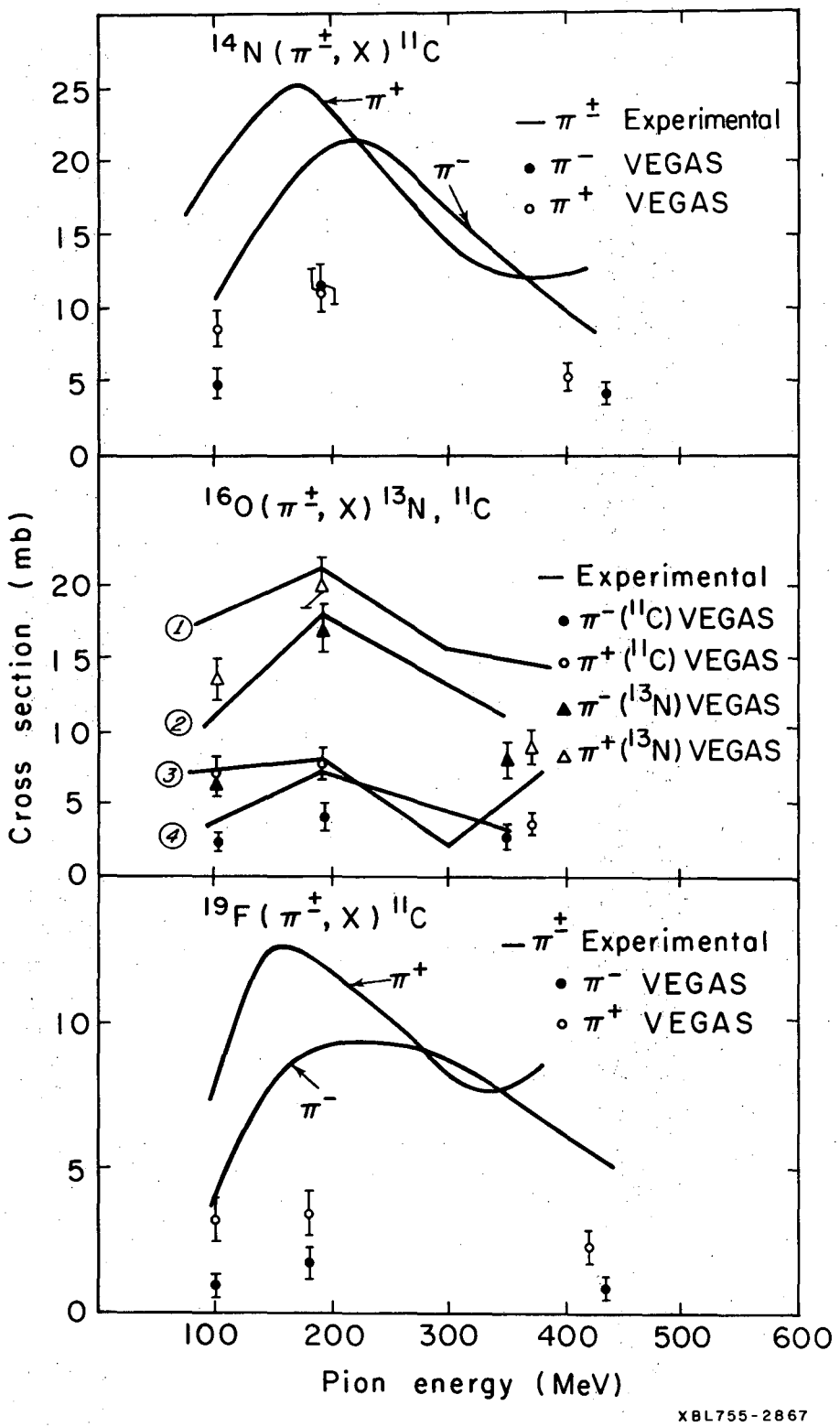

Fig. 4-9. Calculated and experimental complex pion cross sections. Solid curves represent the experimental data, while individual points are results of the calculation. For the middle diagram, the numbered curves are: (1) $^{16}O(\pi^+,X)\ ^{11}C$ (2) $^{16}O(\pi^-,X)\ ^{11}C$ (3) $^{16}O(\pi^+,X)\ ^{13}N$ (4) $^{16}O(\pi^-,X)\ ^{13}N$.

is somewhat a surprise, because both theoretical approaches employ similar underlying assumptions. Although the NCE process is accounted for in the HEVI code,(57) it appears that this particular mechanism is seriously underestimated in the calculation. Such discrepancies may be natural consequences of the nuclear model used in the code.

In the original VEGAS program,(53) it was assumed that the momentum distribution of nucleons in the nucleus was that of a degenerate Fermi gas. Since this model is statistical in nature, it applicability to the light nuclei in this work is crude at best, and conceivably, could affect the cross section magnitudes. The nuclei ^{14}N, ^{16}O, and ^{19}F would more accurately be represented in the calculation by the jj coupling or shell model of the nucleus.(108)

Another consequence of the Fermi gas model is that the residual excited cascade nucleus will have a continuum of excited levels, as given by the level density expression $\rho(E) = C \exp 2(aE)^{\frac{1}{2}}$, where C and a are constants and E is the residual excitation energy. This treatment is again not particularly accurate for light nuclei, especially in the case of ^{13}N, which has no excited bound levels. Figure 4-6 demonstrates the large cross section reduction when the instability of excited ^{13}N levels is taken into account, although even then, the agreement between experimental and theoretical cross sections in the area of the (3,3) resonance is still poor.

An additional facet of the calculation may be seen as affecting the more complex reaction cross sections. A single average value for the binding energies of protons and neutrons is used throughout the cascade calculation (independent of how many nucleons have escaped) to estimate

cutoff energies, below which the cascade nucleon is captured. In reality, these binding energies of neutrons and protons in the nucleus should change with the emission of every cascade nucleon. For light nuclei, which could become very quickly neutron excess or deficient with the emission of just a few nucleons, the variation of binding energies would be particuarly important. Thus, the initially fixed cutoff energies could be in reality either too high or too low as the cascade progressed and would possibly result in suppression or overproduction of certain cascade nucleons. A solution to this problem may be to use the correct binding energies throughout the cascade, or to apply a correction for the changing nucleon binding energies at each step along the cascade.

4.5 Suggested Experiments

As is the nature of scientific investigation, more questions seem to be uncovered than answered, and certainly this thesis project was no exception. Therefore, the following are suggested as future experiments that could contribute additional insights to the present understanding of pion-induced reactions:

(1) $(\pi^{\pm},\pi N)$ reactions on nuclei heavier than the ones studied here, and the application of the NCE model of Sternheim and Silbar to the measured R_{π^-/π^+} ratios.

(2) Extending $(\pi^{\pm},\pi N)$ cross sections to higher energies (> 550 MeV) than experienced in this work. This could accomplish two goals:

(a) Confirm the CKO mechanism at these energies, if $R_{\pi^-/\pi^+} = \sigma(\pi^-n)/\sigma(\pi^+n)$

(b) Measure the mean lifetime of the πN isobar inside the nucleus from the width of the $A(\pi^{\pm},\pi N)B$ excitation function near 600 and/or 900 MeV. (Momentum broadening effects make this a problem at 180 MeV)

(3) Further $(\pi^{\pm},\pi N)$ cross section measurements for reactions populating excited levels of the residual nucleus, by using counter techniques

(4) An angular distribution recoil study of $(\pi^{\pm},\pi N)$ reactions, which would become possible only with pion fluxes exceeding about 10^{10}/sec. This experiment could provide further information on the $(\pi,\pi N)$ reaction mechanism.

(5) Ratio measurements for pion-induced proton knockout reactions around the (3,3) resonance on various nuclei, and the application of the NCE model.

(6) Studies of complex spallation reactions on various elements by pions and subsequent comparisons to proton work

(7) Total cross section measurements through the (3,3) resonance for π^- on ^{14}N and ^{19}F.

5. SUMMARY AND CONCLUSIONS - Part II

Cross sections through the (3,3) resonance for $(\pi^{\pm},\pi N)$ and other more complex spallation reactions on the light nuclei ^{14}N, ^{16}O, and ^{19}F were measured by activation. The results were compared to analogous proton reactions, to a Monte Carlo intranuclear cascade-evaporation model (HEVI-DFF) and to a new semi-classical nucleon charge exchange (NCE). The combined results lead to the following conclusions:

(1) The broad peaks at about 180 MeV that appear in the excitation functions for all $(\pi^{\pm},\pi N)$ and $(\pi^{\pm},X)$ reactions illustrate the preservation of the (3,3) resonance and consequently, the concept of free-particle πN collisions in these nuclei.

(2) All $(\pi^{\pm},\pi N)$ excitation functions in this work have similar shapes and widths (FWHM) of about 250 ± 20 MeV. This peak broadening indicates that the average momentum of the "allowed" struck neutron is about $p_N \sim 180$ MeV/c, a figure consistent with those average momenta observed for protons in 1p nuclei.

(3) Striking differences in $(\pi^{\pm}\pi N)$ excitation function magnitudes are consistent with shell structure effects and the stabilities of the individual residual $(\pi,\pi N)$ nuclei.

(4) Cross sections and cross section ratios R_{π^-/π^+} are in from poor to excellent agreement with prior works. The measured ratio $R_{\pi^-/\pi^+} = 1.7\pm0.2$ at 180 MeV for all the nuclei in this work and is in excellent agreement with the value of 1.6 ± 0.1 determined for the $^{12}C(\pi^{\pm},\pi N)\ ^{11}C$ system.

(5) Monte Carlo cascade-evaporation calculations (HEVI-DFF), while predicting the general energy dependence of simple pion reactions, are at variance with the experimental cross section magnitudes and cross sections

ratios at the lower energies. These discrepancies are due, perhaps, to the Fermi gas model assumption, which for light nuclei, is admittedly crude.

(6) The mechanism of the $(\pi,\pi N)$ reaction, a puzzle for some time, is deduced from this work to consist of the following plausible mechanisms: CKO and NCE, with a small contribution from ISE and/or CESE (about 10%) and isobar formation (2-10%) in the energy region from 100-350 MeV; and almost entirely CKO, with small mixtures of NCE, and ISE and/or CESE mechanisms above 350 MeV.

(7) Mechanisms of complex pion spallation reactions are seen to be similar to those for complex proton reactions at energies exceeding about 100 MeV. Above this energy, pion absorption may be a small but still significant contributor to the overall reaction mechanism.

6. FINAL SUMMARY AND CONCLUSIONS - Parts I and II

The general objective of this thesis was to study the effect of free-particle collisions in the nucleus. This was achieved by the measurement of cross sections for simple proton and pion-induced reactions over energy regions where the free-particle cross sections displayed interesting structure(s). In the study of (p,2p) reactions, this was performed over the region above 0.3 GeV incident proton energy, where a rise in $\sigma(pp)$, ascribed to the onset of inelastic meson producing collisions, occurs. In the study of $(\pi^{\pm},\pi N)$ and other more complex pion spallation reactions, incident pion energies through the (3,3) pion-nucleon resonance were used. A set of final summary and conclusions may be made from these two studies:

(1) Both simple reactions of the form (a,aN) and more complex reactions of the form (a,X) may exhibit structure in their excitation functions that is directly attributed to initial free-particle aN collisions.

(2) Cross section magnitudes for (a,aN) reactions may be influenced, aside from attenuation factors, by nuclear shell structure and the stability of the residual (a,aN) nucleus to particle emission.

(3) Monte Carlo calculations of cross sections generally give poor agreement with the magnitudes of the experimental (a,aN) and more complex (a,X) cross sections. It is concluded, that the Fermi gas model is not an accurate representation of light nuclei for cascade-evaporation calculations.

(4) The mechanisms of high energy nuclear reactions induced by protons and pions are very similar.

(5) Isobars, formed in inelastic nucleon-nucleon and elastic pion-nucleon collisions within the nucleus, appear to contribute, a small but signifi-

cant (< 10%) fraction of the yield for simple (a,aN) reactions in this work.

(6) The pion data coupled with the nucleon charge-exchange model (NCE) gives evidence for the unclean knockout mechanism(UCKO). The UCKO process, judging from previous work, has not received strong consideration as a mechanism for reactions of the form (a,aN) at high energies, where CKO was thought to dominate.

ACKNOWLEDGEMENTS

I would like to thank my research director, Dr. Samuel S. Markowitz, for his patient guidance, scientific insights, and support during my career at Berkeley.

In addition, I would like to thank the following staff at the Lawrence Berkeley Laboratory:

Dr. Darrell Fee and Ms. Diana Lee for assistance and advice during the initial stages of this research project;

Dr. A. Poskanzer for extremely helpful coaching in the presentation of the LAMPF proposal;

Dr. H. Baer of the Crowe Group for allowing parasitic experiments in the Meson Cave;

Drs. K. C. Leung, P. Glodis, and D. Sober of the UCLA-Haddock Group for allowing frequent interruptions in their experiments for independent exposures;

James Vale, Leal Kanstein, and the rest of the crew for irradiations at the 184-inch synchrocyclotron.

Walt Hartsough, Ken Crebbin, and their crew for time on the Bevatron.

It is with distinct and special pleasure that I thank the following people, all of whom were responsible for some facets of my scientific education during my stay at the Los Alamos Scientific Laboratory:

Dr. Bruce J. Dropesky for his aid in implementing and scheduling of the pion work at an early date.

Dr. R. R. Silbar for many enthusiastic and informative discussions of the theoretical aspects of the pion work and for providing the nuclear charge exchange calculations.

Dr. Gerhart Friedlander my scientific Grandfather for teaching me to multiscale by eye.

Dr. R. A. "Bob" Williams and Ms. Maryanne (MAY) Yates for excellent assistance in the execution of the pion study at LAMPF and for outstanding hospitality and friendship during my visit with the Iguana.

Dr. W. "King" Hensley and his wife Carol for their excellent hospitality and moral support while I stayed in Los Alamos. Special thanks go to Walt for his help in the setup of the scintillation detectors and to Carol for the production of outstanding enchiladas.

Dr. G. D. Harp for discussions of the Monte Carlo results relevant to this study.

Drs. C. J. Orth and G. Butler of the Pion Monitoring Group.

The Tel-Aviv University Group for parasitic runs in their LEP beam.

Finally I would like to thank James B. Lansing (JBL) for the reproduction of crystal clear and crisp sounding music- the way it was always meant to be heard- by which much of thesis was written.

This work was supported by the Energy Research and Development Administration.

APPENDIX A

Measurement of Gamma Ray Counting Efficiencies for Ge(Li) Detectors

The calibration of the 20 cm^3 planar and 30 cm^3 coaxial Ge(Li) detectors for efficiency as a function of gamma ray energy was achieved by counting a set of gamma ray standard sources obtained from the International Atomic Energy Commission (IAEA) in Vienna, Austria. These gamma ray energies varied from 60-1333 keV. The sources, initially having about 10 μCi of activity, are summarized along with their respective decay characteristics recommended by the IAEA in Table A-1.

The counting efficiency was defined as the ratio of observed counts in a photopeak to the absolute counting rate. All photopeaks were analyzed by the code SAMPO (27) and absolute counting rates were calculated from the source strength, given by the IAEA to within 1%, with corrections for gamma branching ratios and decay factors. The result for the 30 cm^3 coaxial detector at a distance of 10 cm is represented in Fig. A-1. The efficiency for any given gamma ray energy is simply interpolated from this curve.

During the course of this work, the efficiencies of the two detectors was checked periodically. It was found that the efficiency of each detector never varied by more than about 2%.

Table A-1. Nuclear data for the γ-ray standards

Radionuclide	Half-life	Photon energy (keV)	% per disintegration
^{241}Am	432.9 years	59.54	35.9
^{57}Co	271.6 days	122.0	85.0
^{203}Hg	46.8 days	279.2	81.6
^{22}Na	2.6 years	511. (from β^+)	181.1
		1274.6	100.0
^{137}Cs	30.5 years	661.6	85.1
^{54}Mn	312.6 days	834.8	100.0
^{60}Co	5.28 years	1173.2	100.0
		1332.5	100.0
^{113}Sn	115 days	393.0	Ref.a

[a]Source calibrated in counts/sec of the 393 keV gamma

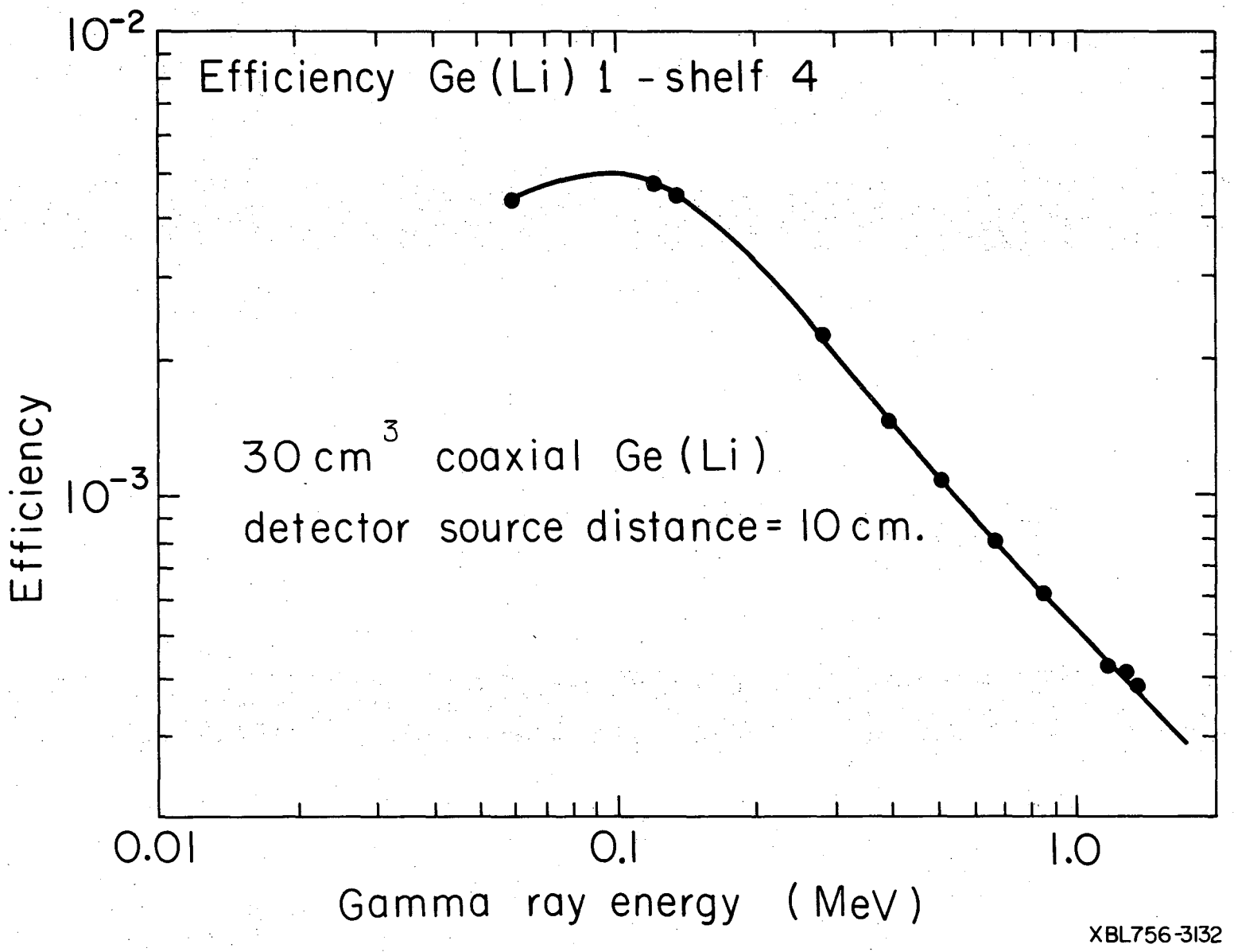

Fig. A-1. The efficiency of the 30 cm^3 Ge(Li) detector as a function of gamma energy. All measurements were taken at a distance of 10 cm from the aluminum cannister housing the crystal.

APPENDIX B

Isospin Wavefunctions and Cross Section Ratios for the Pion-Nucleon System

The interaction between a pion and a nucleon of definite total angular momentum J depends only on the total isospin T, which can have values T = 3/2 or T = 1/2. The possible values of T_3, the isospin projection, are then ± 3/2, ± 1/2 for the case of T = 3/2 and ± 1/2 for the T = 1/2 case. Thus, for a given value of T and T_3, it is possible to write various eigenfunctions for the different pion-nucleon combinations.

For example, the $\pi^+ p$ system can only have quantum numbers T = 3/2, T_3 = 3/2. However, the combinations $\pi^- p$ and $\pi^\circ n$ have T_3 = - 1/2, but are mixtures of the T = 3/2 and the T = 1/2 states. Therefore, the different pion-nucleon combinations would be added using the appropriate Clebsch-Gordan coefficients to obtain the following eigenfunctions of $|T\ T_3\rangle$:

$$|3/2,3/2\rangle = |\ p\ \pi^+\rangle$$

$$|3/2,1/2\rangle = \sqrt{\frac{1}{3}}\ |n\ \pi^+\rangle + \sqrt{\frac{2}{3}}\ p\pi^\circ\rangle$$

$$|3/2,-1/2\rangle = \sqrt{\frac{1}{3}}\ |p\ \pi^-\rangle + \sqrt{\frac{2}{3}}\ p\pi^\circ\rangle$$

$$|3/2,-3/2\rangle = |\ n\ \pi^-\rangle$$

$$|1/2,1/2\rangle = \sqrt{\frac{2}{3}}\ |\ n\pi^+\rangle - \sqrt{\frac{1}{3}}\ |p\pi^\circ\rangle$$

$$|1/2,-1/2\rangle = \sqrt{\frac{1}{3}}\ |\ n\pi^\circ\rangle - \sqrt{\frac{2}{3}}\ |p\ \pi^-\rangle$$

Conversely, any given pion-nucleon system can be expressed in terms of the isospin states as follows

$$|\, p\,\pi^+ \rangle = |\, 3/2,3/2 \rangle$$

$$|\, p\,\pi^\circ \rangle = \sqrt{\frac{2}{3}}\,|\, 3/2,1/2 \rangle - \sqrt{\frac{1}{3}}\,|1/2,1/2 \rangle$$

$$|\, p\,\pi^- \rangle = \sqrt{\frac{1}{3}}\,|3/2,-1/2 \rangle - \sqrt{\frac{2}{3}}\,|1/2,-1/2 \rangle$$

$$|\, n\,\pi^+ \rangle = \sqrt{\frac{1}{3}}\,|3/2,1/2 \rangle + \sqrt{\frac{2}{3}}\,|1/2,1/2\ \rangle$$

$$|\, n\,\pi^\circ \rangle = \sqrt{\frac{2}{3}}\,|3/2,-1/2 \rangle + \sqrt{\frac{1}{3}}\,|1/2,-1/2 \rangle$$

$$|\, n\,\pi^- \rangle = |\, 3/2,-3/2 \rangle$$

Now, the following reactions

(1) $\pi^+ + p \rightarrow \pi^+ + p = \pi^- + n \rightarrow \pi^- + n$ elastic scattering - σ_1

(2) $\pi^- + p \rightarrow \pi^- + p = \pi^+ + n \rightarrow \pi^+ + n$ elastic scattering - σ_2

(3) $\pi^- + p \rightarrow \pi^\circ + n = \pi^+ + n \rightarrow \pi^\circ + p$ charge-exchange-scattering - σ_3

(B-1)

can be described in terms of a scattering matrix in isospin space, i.e. a $T = 1/2$ scattering amplitude associated with matrix $M(1/2)$ and a $T = 3/2$ scattering amplitude associated with matrix $M(3/2)$. Since the scattering matrix is independent of T_3, the cross sections for the processes described in (B-1) can be expressed as

$$\sigma_1 \alpha\, |\langle \pi^+ p|\ M\ |\pi^+ p\rangle|^2 \alpha |\langle\, 3/2\ 3/2|M(3/2)|\ 3/2,3/2\ \rangle|$$

$$\alpha |A(3/2)|^2$$

$$\sigma_2\ \ \alpha |\langle \pi^- p\ |M|\ \pi^- p\rangle|^2 \alpha\, |\langle 1/3 \langle 3/2,-1/2|M(\tfrac{3}{2})|3/2,-1/2\rangle$$

$$+ \frac{2}{3}\langle 1/2,-1/2|M(1/2)|1/2,-1/2\rangle|^2 \alpha \frac{1}{9}\,|A(3/2) + 2A(1/2)|^2$$

$$\sigma_3 \alpha | \pi n|M|\pi^- p\rangle|^2 \alpha \left|\sqrt{\tfrac{2}{3}} \langle \tfrac{3}{3},1/2|M(\tfrac{3}{2})|\tfrac{3}{2},1/2\rangle - \sqrt{\tfrac{2}{3}} \langle \tfrac{1}{2},-\tfrac{1}{2}|M(\tfrac{1}{2})|\tfrac{1}{2},-\tfrac{1}{2}\rangle\right|^2 \alpha \left|\sqrt{\tfrac{2}{3}} A(\tfrac{3}{2}) - \sqrt{\tfrac{2}{3}} A(\tfrac{1}{2})\right|^2$$

$$\alpha \frac{2}{9} \left|A(\tfrac{3}{2}) - A(\tfrac{1}{2})\right|^2$$

For the one case where A(1/2) = 0 and A(3/2) $\neq$ 0, the ratio of cross sections for the 3 reactions of (B-1) is $1:\frac{1}{9}:\frac{2}{9}$ or 9:1:2. Thus one has that

$$R_{\pi^-/\pi^+} = \frac{\sigma_T(\pi^+ p)}{\sigma_T(\pi^- p)} = \frac{\sigma_1}{\sigma_2+\sigma_3} = \frac{9}{1+2} = 3$$

which is about the value one would expect near the (3,3) resonance. The assumption that A(1/2) contributes negligibly to the cross sections compared to A(3/2) near 180 MeV is verified by the fact that experimentally, R_{π^-/π^+} for free-particle scattering is 2.9±0.2 (58) at 180 MeV incident pion energy.

REFERENCES

1. J. M. Miller and J. Hudis, Ann. Rev. Nucl. Sci. 9, 159 (1959).

2. J. R. Grover and A. A. Caretto, Jr., Ann. Rev. Nucl. Sci. 14, 51 (1964).

3. J. Hudis in "Nuclear Chemistry" Vol. I, Academic Press, New York, L. Yaffe, ed. (1968).

4. R. Serber, Phys. Rev. 72, 1114 (1947).

5. B. B. Cunningham, H. H. Hopkins, M. Linder, D. R. Miller, P. R. O'Connor, I. Perlman, G. T. Seaborg, and R. C. Thompson, Phys. Rev. 72, 739 (1947).

6. G. F. Chew, Phys. Rev. 80, 196 (1950).

7. G. F. Chew and G. C. Wick, Phys. Rev. 85, 641 (1952).

8. G. F. Chew and M. L. Goldberger, Phys. Rev. 87, 778 (1952).

9. J. A. Panontin, L. L. Schwartz, A. F. Stehney, E. P. Steinberg, and L. Winsberg, Phys. Rev. 145, 754 (1966).

10. L. P. Remsberg, Phys. Rev. 174, 1338 (1968).

11. L. P. Remsberg, Phys. Rev. 188, 1703, (1969).

12. E. L. Grigor'ev, O. V. Lozhkin, Z. Marich, V. K. Suslenko, and V. I. Kochkin, Sov. J. Nucl. Phys. 12, 491 (1971).

13. Y. W. Yu, A. A. Caretto, Jr., and L. B. Church, Nucl. Phys. A152, 295 (1970).

14. Particle Data Group (O. Benary, L. R. Price, and G. Alexander), NN and ND Interactions (Above 0.5 GeV/c)- A Compilation, UCRL-20000NN (1970).

15. P. L. Reeder, University of California, Lawrence Radiation Laboratory Report, UCRL-10531, unpublished (1962).

16. S. Meloni and J. B. Cumming, Phys. Rev. 136, B1359 (1964).

17. P. L. Reeder, Phys. Rev. 178, 1795 (1969).

18. E. F. Norton, National Academy of Sciences, Report NAS-NS-3111 (1967).

19. J. Vale, private communication.

20. K. Crebbin, private communication.

21. J. B. Cumming, Ann. Rev. Nucl. Sci. 13, 261 (1963).

22. C. M. Lederer, J. Hollander, and I. Perlman, Table of the Isotopes, (Wiley, New York, 1976), 6th ed.

23. M. K. Wakat, Nucl. Data A8, 445 (1971). At this point it is noted that a more recent tabulation of half-lives and gamma ray energies has been published by W. W. Bowman and K. W. MacMurdo, Atomic and Nucl. Data 13, 90 (1974) which lists a half-life for ^{47}Sc of 3.41 days, as compared to the 3.43 day half-life given in Wakat and used in this work.

24. Both detectors were fabricated by the Semiconductor Group at Lawrence Berkeley Laboratory, Berkeley, California.

25. Obtained from the International Atomic Energy Association, Vienna, Austria.

26. D. L. Smith, Nucl. Instr. Methods 94, 157 (1971).

27. J. Routti and S. Prussin, Nucl. Instr. Methods, 72, 125 (1969).

28. J. B. Cumming, U. S. Atomic Energy Commission Report No. NAS-NS3107, unpublished (1962), p. 25.

29. J. P. Cohen, G. Albuoy, and N. Poffe, J. Phys. (Paris) 26, 427 (1965).

30. A. A. Caretto, Jr. Nucl. Phys. A92, 133 (1967).

31. I. Dostrovsky, R. Davis, Jr., A. M. Poskanzer, and P. L. Reeder, Phys. Rev. 139, B1513 (1965).

32. I. Dostrovsky, H. Gauvin, and M. Lefort, Phys. Rev. 169, 836 (1968).

33. A. A. Caretto, Jr., U. S. Atomic Energy Commission Report NYO-10693, unpublished (1964).

34. A. H. Wapstra and N. B. Gove, Nucl. Data A9, 303 (1971).

35. F. Ajzenberg-Selove, Nucl. Phys. A152, 1 (1970).

36. Nuclear Data Sheets, "Nuclear Level Schemes A=45 through A=257," edited by the Nuclear Data Group, ORNL, Academic Press, New York and London (1973).

37. B. R. Erdal, L. Westgaard, J. Zylics, and E. Roeckl, Nucl. Phys. A194, 449, (1972).

38. W. J. Nieckarz, Jr., and A. A. Caretto, Jr., Phys. Rev. C2, 1917 (1970).

39. R. F. Schall, Jr., and A. A. Caretto, Jr., Phys. Rev. C2, 1924 (1970).

40. P. J. Karol and J. M. Miller, Phys. Rev. 166, 1089 (1968).

41. W. D. Myers, Phys. Lett. 30B, 401 (1969).

42. P. A. Benioff, Phys. Rev. 119, 324 (1960).

43. N. T. Porile and S. Tanaka, Phys. Rev. 130, 1541 (1963).

44. M. Riou, Rev. Mod. Phys. 37, 375 (1965).

45. G. Jacob and Th. A. J. Maris, Rev. Mod. Phys. 38, 121 (1966).

46. D. J. Millener and P. E. Hodgson, Nucl. Phys. A209, 59 (1973).

47. A. A. Ross, H. Mark, and R. D. Lawson, Phys. Rev. 102, 1613, (1956).

48. N. Metropolis, R. Bivens, M. Storm, A. Turkevich, J. M. Miller, G. Friedlander, Phys. Rev. 110, 185 (1958).

49. N. Metroplis, R. Bivens, M. Storm, J. M. Miller, G. Friedlander, and A. Turkevich, Phys. Rev. 110, 204 (1958).

50. N. Metroplis, R. Bivens, M. Storm, J. M. Miller, G. Friedlander,

51. H. W. Bertini, Phys. Rev. 188, 1711 (1969).

52. H. W. Bertini, Phys. Rev. C6, 631 (1972).

53. K. Chen, Z. Fraenkel, G. Friedlander, J. R. Grover, J. M. Miller, and Y. Shimamoto, Phys. Rev. 166, 949 (1968). This is the code designated as VEGAS.

54. G. D. Harp, K. Chen, G. Friedlander, Z. Fraenkel, and J. M. Miller, Phys. Rev. C8, 581 (1973). This program is the low energy VEGAS Isobar code, designated as LEVI.

55. G. D. Harp, Phys. Rev. C10, 2387 (1974).

56. I. Dostrovsky, Z. Fraenkel, and G. Friedlander, Phys. Rev. 116, 1683 (1959).

57. G. D. Harp (private communication).

58. E. Bracci, J. P. Droulez, E. Flamino, J. D. Hansen, and D.R.O. Morrison, "Compilation of Cross Sections- π^- and π^+ Induced Reactions" CERN/HERA Report 72-1 (1972).

59. The equality or approximate equality of the number of neutrons and protons in the target nucleus is a necessary condition for Eq.(1-1) to hold, as this in turn means that the reaction cross sections for π^- and π^+ on a target nucleus are equal (or nearly equal) by charge symmetry.

60. W. O. Lock and D. F. Measday, Intermediate Energy Nuclear Physics, Methuen and Co., LTD, London (1970).

61. P. L. Reeder and S. S. Markowitz, Phys. Rev. 133, B639 (1964).

62. A. M. Poskanzer and L. P. Remsberg, Phys. Rev. 134, B779 (1964).

63. S. Kaufman and C. O. Hower, Phys. Rev. 154, 924 (1967).

64. S. O. Thompson, L. Husain, and S. Katcoff, Phys. Rev. C3, 1538 (1971).

65. C. O. Hower and S. Kaufman, Phys. Rev. 144, 917 (1966).

66. H. S. Plendl, D. Burch, K. A. Eberhard, M. Hamm, A. Richter, C. J. Umbarger and W. P. Trower, Nucl. Phys. B44, 413 (1972).

67. K. R. Hogstrom, B. W. Mayes, L. Y. Lee, J. C. Allred, C. Goodman, G. S. Mutchler, C. R. Fletcher, and G. C. Phillips, Nucl. Phys. A215, 598 (1973).

68. V. M. Kolybasov, Sov. J. Nucl. Phys. 2, 101 (1966).

69. O. D. Dalkarov, Phys. Lett. 26B, 610 (1969).

70. F. Selleri, Phys. Rev. 164, 1475 (1967).

71. D. T. Chivers, E.M. Rimmer, B. W. Allardyce, R. C. Witcomb, J. J. Domingo, and N. W. Tanner, Nucl. Phys. A126, 129 (1969).

72. Y. A. Budagov, P. F. Ermolov, E. A. Kushinenko, and V. I. Muskalev, Sov. Phys.-JETP, 15, 824 (1962).

73. M. A. Moinester, M. Zaider, J. Alster, D. Ashery, S. Cochavi, and A. I. Yavin, Phys. Rev. C8, 2039 (1973).

74. B. J. Leib, H. O. Finsten, and W. K. Lankford, Bull. Am. Phys. Soc. 15, 596 (1970).

75. M. V. Yester, A. A. Caretto, Jr., M. Kaplan, P. J. Karol, and R. L. Klobouchar, Phys. Lett. 45B, 327 (1973).

76. M. Zaider, J. Alster, D. Ashery, S. Cochavi, M. A. Moinester, and A. I. Yavin, Phys. Rev. C10, 938 (1974).

77. B. J. Leib, Ph.D. dissertation, College of William and Mary, 1971 (unpublished).

78. B. J. Leib, H. S. Plendl, H.O. Funsten, W. J. Kossler, and C. E. Stronach, Phys. Rev. Lett. 34, 965 (1975).

79. P. J. Karol, A. A. Caretto, Jr., R. L. Klobouchar, D. M. Montgomery, R. A. Williams, and M. V. Yester, Phys. Lett. 44B, 459 (1973).

80. H. S. Plendl, D. Robson, C. J. Umbarger, D. F. Burch, and A. Richter, Bull. Am. Phys. Soc. 16, 1174 (1971).

81. D. Ashery, M. Zaider, Y. Shamai, S. Cochavi, M. A. Moinester, A. I. Yavin, and J. Alster, Phys. Rev. Lett. 32, 943 (1974).

82. D. H. Wilkinson, J. Phys. Soc. Jap. Suppl. 24, 469 (1968).

83. R. Seki, Nuovo Cimento, 9A, 235 (1972).

84. V. M. Kolybasov, Phys. Lett. 27B, 3 (1968).

85. V. M. Kolybasov and N. Ya Smorodinskaya, Phys. Lett. 30B, 11 (1969).

86. D. Robson, Ann. Phys. (New York) 71, 277 (1972).

87. P. W. Hewson, Nucl. Phys. A133, 659 (1969).

88. B. J. Dropesky, G. W. Butler, C. J. Orth, R. A. Williams, G. Friedlander, M. A. Yates, and S. B. Kaufman, Phys. Rev. Lett. 34, 821 (1975).

89. M. M. Sternheim and R. R. Silbar, Phys. Rev. Lett. 34, 824 (1975).

90. The cross sections for the $^{12}C(\pi^{\pm},\pi N)\ ^{11}C$ reaction were taken from Ref. 88. These cross sections in the letter are subject to minor adjustment prior to final publication; R. A. Williams (private communication).

91. H. Baer (private communication).

92. K. C. Leung, D. Sober, P. Glodis (private communication).

93. LAMPF Users Handbook, Report MP-DO-1-UHB (1974).

94. L. P. Remsberg, Annu. Rev. Nucl. Sci. 17, 347 (1967).

95. G. Friedlander, J. Kennedy, and J. M. Miller, Nuclear and Radiochemistry, John Wiley and Sons, Inc., New York (1964).

96. W. Peter Trower, University of California Lawrence Radiation Laboratory Report, Vol. II, UCRL-2426, 1966 (unpublished).

97. F. Binon, P. Duteil, J. P. Garron, J. Gorres, L. Hugon, J. P. Peigneux, C. Schmit, M. Spighel, and J. P. Stroot, Nucl. Phys. B17, 168 (1970).

98. F. Ajzenberg-Selove and T. Lauritsen, Nucl. Phys. A114, 1 (1968).

99. F. Ajzenberg-Selove, Nucl. Phys. A190, 1 (1972).

100. R. Herman and K. Hofstadter, High-Energy Electron Scattering Tables, Stanford University Press, Stanford, CA (1960).

101. The preliminary $^{27}Al(\pi^{\pm},X)\ ^{18}F$ results were communicated by Dr. B. J. Dropesky.

102. C. K. Garrett and A. L. Turkevich, Phys. Rev. C8, 594 (1973).

103. Samuel S. Markowitz, Ph.D. thesis, Princeton University, 1957 (unpublished).

104. J. L. Symonds, J. Warren, and J. D. Young, Proc. Phys. Soc. (London) A70, 824 (1957).

105. I am grateful to Dr. R.R.Silbar, Los Alamos Scientific Laboratory for providing the NCE calculations of R_{π^-/π^+}.

106. H. Ullrich, E. T. Boschitz, H. D. Engelhardt, and C. W. Lewis, Phys. Rev. Lett, 33, 433 (1974).

107. Z. Fraenkel, Phys. Rev. 130, 2407 (1963).

108. Z. Fraenkel (private communication).

TECHNICAL INFORMATION DIVISION
LAWRENCE BERKELEY LABORATORY
UNIVERSITY OF CALIFORNIA
BERKELEY, CALIFORNIA 94720